A COMPUTATIONAL STUDY OF THE ELECTRICAL RESPONSE OF BIOLOGICAL

CELLS WITH REALISTIC THREE-DIMENSIONAL MORPHOLOGIES

A DISSERTATION IN
Electrical Engineering
and
Physics

Presented to the Faculty of the University of
Missouri-Kansas City in partial fulfillment of
the requirements for the degree

DOCTOR OF PHILOSOPHY

by
SOMEN BAIDYA

M.S., Electrical Engineering,
Georgia Southern University, 2016

Kansas City, Missouri
2021

A COMPUTATIONAL STUDY OF THE ELECTRICAL RESPONSE OF BIOLOGICAL

CELLS WITH REALISTIC THREE-DIMENSIONAL MORPHOLOGIES

Somen Baidya, Candidate for the Doctor of Philosophy Degree

University of Missouri-Kansas City, 2021

ABSTRACT

One of the unique features of a biological cell is the cell membrane that protects the cell interior by establishing a physical barrier between the cytoplasm and the extracellular matrix and governs the distribution of the cytoskeleton to control the three-dimensional (3D) morphology of a cell. From an electrical standpoint, the cell membrane represents an insulating layer with selective ion permeability, thereby administering an ionic imbalance between the conductive extracellular and intracellular fluids. Consequently, the electrical characterization of a biological cell mostly focuses on the specific electrical properties of the cell membrane and the means to modulate its semipermeable nature. Previously reported research studies had revealed many characteristics of the cell membrane. However, they did not explore the morphological feature to its fullest, especially in three dimensions. Motivated by this knowledge gap, this work explores the effect of the 3D variations in cell morphology on the electrical response of biological cells.

The most diverse and accurate 3D cell database developed to date by the National Institute of Standards and Technology was incorporated in this study, and an extensive investigation of these cells' electrical characteristics was manifested by computational means. The cell database has hundreds of morphologies that were reconstructed from stem cells grown

in different environments. To quantify how cell morphology affects the electrostatic properties of these complex cells, a validation study was conducted to study the polarizability tensors of stem cell morphologies, using three independent computational techniques. To draw accurate conclusions, the polarizability tensors of more than 1000 stem cells were calculated and statistical analysis was conducted to identify which growth environment generates cells with similar electric properties. Next, we studied the induced transmembrane voltage (ITV) across the cell membrane when it is subjected to a static and dynamic external electrical stimulus. The ITV generated across a cell's membrane plays a significant role in the process of electroporation since the membrane permeability increases when the ITV exceeds a certain threshold. By setting an arbitrary ITV electroporation threshold, the electroporated area for each stem cell morphology at different orientations was calculated and significant differences were shown in comparison to spherical cells of similar size. The significance of morphological variation is more prominent for dynamic frequency-dependent excitation. Using computational experiments, it has been observed that as the frequency of the excitation increases, the ITV decreases beyond a certain cutoff frequency that varies with cell morphology.

While the ITV study is vital in low-frequency applications, the nonlinear membrane dynamics must be taken into consideration in case of high intensity ultra-short electrical stimulus, commonly used in supra-electroporation techniques to penetrate the internal organelles' (i.e. nucleus, mitochondria etc.) membrane. As a consecutive step of this research, a computational testbed was developed upon the stem cell geometries to investigate the supra-electroporation phenomenon in realistic cell shapes. The results obtained from this study suggest that supra-electroporation is highly dependent on the cell membrane irregularity, especially the location of the internal organelle with respect to any protrusion on the cell

surface. The results from this observation can be utilized to engineer selective targeting of the desired cell with specific morphology.

APPROVAL PAGE

The faculty listed below, appointed by the Dean of the School of Graduate Studies have examined a dissertation titled "A Computational Study of The Electrical Response of Biological Cells with Realistic Three-Dimensional Morphologies" presented by Somen Baidya, candidate for the Doctor of Philosophy degree, and certify that in their opinion it is worthy of acceptance.

<u>Supervisory Committee</u>

Ahmed M. Hassan, Ph.D., Committee Chair
Department of Computer Science and Electrical Engineering

Paul Rulis, Co-discipline Advisor
Department of Physics and Astronomy

Masud Chowdhury, Ph.D.
Department of Computer Science and Electrical Engineering

Deb Chatterjee, Ph.D.
Department of Computer Science and Electrical Engineering

Da-Ming Zhu, Ph.D.
Department of Physics and Astronomy

CONTENTS

ILLUSTRATIONS

TABLES

ACKNOWLEDGEMENTS

Firstly, I would like to convey my heartful gratitude to my honorable supervisor, Dr. Ahmed Hassan for his continuous support and motivation since the very first day I joined Multidisciplinary Multiscale Electromagnetics Lab (MMEL). I am extremely grateful to him for providing me the opportunity to participate in this great research area, and without his inspiration, guidance, constructive criticism, and great suggestions, this feat would have been an impossible task. His expertise and insightful feedbacks were invaluable in formulating the research questions and methodology of this work. I am thankful to him for guiding me throughout the whole journey, for pushing me beyond boundaries to improve my analytic power, interpretation skills, problem-solving and decision-making skills, and for encouraging me by celebrating every small research success. I am privileged to learn so many things from him, not only his exceptional scientific knowledge but also his extraordinary human qualities of kindness, hearty, humor, and understanding. For all this and more, I am greatly indebted to him for believing in me at times when even me myself was doubtful about my capabilities. He is undoubtedly the greatest research mind that I came into contact with during my graduate study tenure and I am honored to have him as my mentor. I lookup to him as my role model and wish him every success in his professional and personal life.

DEDICATION

To my mother, who sacrificed all her comforts to make her children's dreams come true

CHAPTER 1

1   INTRODUCTION

Where the conventional electricity depends on the conduction of electrons and holes through a medium, bioelectricity is generated due to the flow of ionic charges inside our body. From signal propagation among neurons to regulating the blood flow through our heart, bioelectricity governs several core functionalities of human physiology. Beside neurons and cardiac tissues that can generate an independent electric potential, other cells and tissues also exhibit endogenous electric field which is vital for their operation. For instance, epithelial and endothelial tissues that are present in the skin, cornea, and linings of other internal organs of human body, exhibits a potential difference between the top and bottom layer of the tissue. This potential difference is a result of net ion flow between different compartments of the tissue layer. In case of a wound in the epithelial tissue, this endogenous electric field modulate the cell motility towards the wound center, thereby initiating the natural wound healing process, which implies different cell types also exhibit significant electrical characteristics under external electrical stimulus.

The core component of a biological cell is the cell membrane and the genetic material. Biological cell membranes are involved in several cellular functionalities by maintaining the ionic balance between the extracellular and intracellular medium. The phospholipid bilayer of the cell membrane maintains the cellular integrity of a cell by allowing passage to selective ions and organelles. Consequently, there exists a potential difference across the cell membrane due to the ionic imbalance between the intracellular and extracellular matrices. Beside regulating the cellular functionality, this transmembrane voltage plays a vital role in cell signaling and motility. As an effort to modulate the inherent transmembrane voltage present

across a cell membrane, scientists have been trying to engineer the cellular functionality by inducing voltage across the membrane with means of external electrical stimulus. Some of these efforts have been adopted as successful clinical modalities to assess health conditions and to cure diseases. A brief overview of some of these modalities are presented here

1.1 Wound healing

Natural wound healing is a highly complicated process that consists of several timed stages of cell signaling, migration, and proliferation. As discussed above, the endogenous electric field originated during a wound has a considerable effect on almost all stages of wound healing process. Several *in vitro* studies were performed on the different cell types involved in wound healing to investigate their response to endogenous electric field. A comprehensive summary of the steps involved in wound healing process and the outcomes of the electrical stimulus studies on different cell types is presented in [1]. These *in vitro* studies provide substantial evidence of the effect of endogenous electric field on the natural wound healing process which has encouraged researchers to test the use of external electrical stimulation as another potential modality to improve chronic wound cases in vivo. A brief summary of some of the external electrical stimulus studies conducted in human chronic wound cases and its effectivity is enlisted in Table 1.1 [2], [3].

Table 1.1 A summary of the reported effects of different ES modalities on wound healing

| Type of Wound | Type of ES | No. of Patients | | Parameters | Duration | No. of cases with improved wound healing |
		Treatment	Control			
Chronic Dermal Ulcer	Monophasic pulsed vs. sham	26	24	29.2V, 29.2mA, $132\mu s$ pulse	30 min twice for 4 weeks	66% WAR vs. sham 33%

	High voltage pulsed vs. sham	45	15	100-175V, 50μs pulse, 120 Hz	45-120 min daily for 5 weeks	Significant WAR compared to control
Pressure Ulcer	Monophasic pulsed	61	NA	128 pps, 35 mA	30 min twice daily	4 cases of complete healing
	High-voltage pulsed v sham	50	51	50-200V, 50-100 μs pulse, 100 Hz	05.-1 hour daily for 20-90 days	3 cases of accelerated wound healing and WAR
Leg/ Foot ulcer	High-voltage pulsed v sham	96	47	50-150V, 100μs, 100 Hz	50 min stimulation for 6 time or 8 hour daily	2 increased wound healing case and WAR
Diabetic Ischemic wound	High-voltage pulsed	38	NA	140-360V, 90-100μs	45-60 min session for 14-16 weeks	6 improved healing
Pressure Ulcer	LIDC	78	59	300-600 μA	8 weeks	6 cases of complete wound closure and WAR
Foot/ Leg Ulcer	LIDC	62	15	300-500 μA	45-120 min, 3-5 days a week for 5-8 weeks	5 cases of improved helaing
Ischemic Ulcer	LIDC v sham	6	6	Not stated	Until healed	1 LIDC group healed twice as fast as control
Acute Biopsy Wound	Biofeedback	79	79	0.004 mA, 20–80 V, 60 Hz	2 weeks to until full recovery	6 cases of improved scar symptom with increased

					angiogenic response
Foot/ Leg Ulcer	FREMS vs. Control	66	59	0–300 V, 1–1000 Hz, 10–40 µs, 100–170 µA	40 min daily, 5 days a week for 3 weeks to full recovery	Significant WAR reported
Venous ulcers	FREMS v control	10	10	Not stated	5 days a week for 3 weeks	1 Reduced pain and area of ulcers
Diabetic Leg Venous Ulcer	TENS vs Placebo	24	27	80 Hz, 1 ms pulse width	2 times a day for 84 Days	10 full recovery as compared to 4 in case of placebo, WAR
Healthy Volunteers	TENS	31	NA	High frequency: 110 Hz, 200 µs Low frequency: 4 Hz, 200 µs	15 minutes	1 Local increase in blood flow
Blister wound	TENS	9	NA	High frequency: 100 Hz. Low frequency: 2 Hz	45 Minutes	2 Stimulated perfusion
Skin graft donor sites	Bioelectric dressing	13	NA	2–10 mV, 0.6–0.7 V, 10 µA	1 month	4 cases

In the entries above, PPS stands for pulses per seconds; WAR refers to Wound Area Reduction; LIDC refers to Low-Intensity Direct Current, and Sham or Placebo represent the control group where patients did the same procedure as the active treatment without actually having the electrical stimulus.

The conclusion drawn from these studies is that, irrespective of the stimulation routine, ES has a general tendency to increase the wound healing rate and reduce the associated pain. However, to the best of our knowledge, no technique is capable of predicting the optimum

electrical stimulation routine that can effectively improve chronic wound healing for all cases. Therefore, there is a strong need for an optimized standard ES therapy that will irrevocably reduce wound area, accelerate the healing of the wound, reduce pain, and minimize scarring [3]. Before such an optimized stimulation can be developed, a quantitative understanding of the effect of endogenous current on wound healing is needed. Experimental measurements can only access a limited number of spatial and temporal positions without disturbing the wound itself. Therefore, there is a strong need for an accurate computational model that can generate a detailed spatial and temporal map of these electric signals in the vicinity of different kinds of wounds. This computational model should be accurately calibrated from experimental measurements and it needs to be validated by being capable of generating new outcomes that can be validated using alternative experiments

1.2 Dielectrophoresis

When a polarizable particle suspended in a dielectric media is subject to an inhomogeneous electric field, the induced dipole moment will exert a resultant force on the particle towards the anode or the cathode depending on the dielectric property of the particle and the surrounding medium. This phenomenon is known as dielectrophoresis (DEP) and extensively used to manipulate, transport, separate and sort different types of particles. In recent days, DEP has also found its fair share of interest in biomedical fields with major focus on categorizing healthy and pathological cells. A comprehensive review of research methods employing DEP forces in separating eukaryote and procaryote cells, diagnosing virus, bacteria, microorganisms, protein, and enzymes is available in [4]. The research conducted on various type of biological samples utilizing the DEP technique are mostly focused on understanding the fundamental response of biological particles to DEP forces. However, the actual link

between the DEP behavior of biological particles with their electrophysiological properties remains unexplored and require a thorough computational investigation to correlate the variation in DEP characteristics to the dielectric properties of the biological particles.

1.3   Electroporation

Electroporation is the technique of creating pores or opening on the cell membrane surface by applying high-magnitude electrical pulses to allow access of macromolecules inside the cell that are otherwise impermeable though the cell membrane layer. This technique has found its application in several biomedical applications like delivery of drug (electrochemotherapy), proteins (electroinsertion) and genetic materials (electrogenetransfection) into the cell, induce cell or tissue electrofusion, non-thermal tissue ablation, and initiating cell death [5]. However, the mechanisms of electroporation are still not fully understood and there are aspects of the process which are suboptimal in their possible performance yet. This calls for an extensive research on the pore formation dynamics on cell membrane and its correlation to different excitation protocols. Proper understanding of the physiological transformation of electroporation dynamics on the cell membrane hence requires an accurate computational model that can replicate the physics of the phenomena.

Besides, there are numerous disciplines of biological science (neurostimulation, optogenetics, disease diagnostics, biosensor etc.) that requires an accurate representation of cell electrical characteristics. Electrically, the membrane represents an insulator of low electric conductivity, and because of the charge separation between the intracellular and extracellular matrix, each cell membrane constitutes a voltage gradient across it. Hence, a linear circuit representation of the cell membrane will comprise of a capacitor connected in series with a voltage source or battery. However, the nonlinear distribution of membrane proteins and

6

metastable pore formations on the membrane surface asks for a more sophisticated electrical component model that incorporates the nonlinear membrane dynamics.

Over the last century, several research methods have been developed to outline the most accurate electrical representation of the cell membrane. Even though, significant insights regarding the electrical characterization of a biological cell membrane have been revealed through these extensive studies, one most overlooked aspect of this problem definition has been the cell morphology. This study drives the core motivation in this regard and aims to bridge the existing gap in literature by considering the morphological variation in characterizing the electrical properties of biological cells. To achieve this goal, this study incorporates the most accurate three-dimensional cell database developed to date. The database was established by a group of researchers at National Institute of Standards and Technology and presents the minuscule details of the morphological variations of a large number of cells, cultured in ten different microenvironments. By engineering the cell environment, the researchers were able to mimic the natural cell growth inside human body and introduced a wide range of morphological variation. Hence, by incorporating this cell database, the preliminary focus of investigating the morphological variation of cells has been achieved. The course of this thesis has been organized in following fashion:

In chapter 2, the cellular dimensionality of these wide variation of cell shape has been investigated by numerical means. The electrophysiological concern in this case was confined to electrostatic study and concentrates on how variation in cell morphology alone can dictate the electrical characteristics of a cell. For this, we incorporated the physics of perfect electric conductor and perfect magnetic conductor to calculate the electric and magnetic polarizabilities of cells. These two quantities represent two extreme cases and from these measurements, we

demonstrated the application of an close-form equation to determine the electrical characteristics of a realistic cell at actual environment. In chapter 3, the focus shifts towards uniform external electrical stimulus (both static and frequency-dependent excitation) on the cells in suspension. The cell membrane was modeled by a resistive layer of nanometer thickness, while the electrical properties were represented by a linear membrane model. Later in chapter 4, the pore formation dynamics of the cell membrane is taken into account and a nonlinear representation of the cell membrane is incorporated in the numerical methods. The primary problem is utilized in cell 2D cross-section and the validity of the results are confirmed. Finally, in chapter 5, we extend the nonlinear membrane model to 3D morphologies and explore different the effect of different excitation protocol (uniform and nonuniform) on the electroporation characteristics of irregular cell shapes. Overall, this thesis takes a journey of analyzing the electrical characteristics of a cell from a morphological standpoint at the beginning and then progresses along by incorporating the most accurate cell membrane model developed to date to provide the reader with the detailed overview of how variation in cell geometry can influence the study of cell electrophysiology.

CHAPTER 2

2   ANALYSIS OF DIFFERENT COMPUTATIONAL TECHNIQUES FOR

CALCULATING THE POLARIZABILITY TENSORS OF STEM CELLS

WITH REALISTIC THREE-DIMENSIONAL MORPHOLOGIES

2.1   Abstract

Recently, the National Institute of Standards and Technology has developed a database of three-dimensional (3D) stem cell morphologies grown in ten different scaffolds to study the effect of the cells' environments on their morphologies. The goal of this work is to study the polarizability tensors of these stem cell morphologies, using three independent computational techniques, to quantify the effect of the environment on the electric properties of these cells. We show excellent agreement between the three techniques, validating the accuracy of our calculations. These computational methods allowed us to investigate different meshing resolutions for each stem cell morphology. After validating our results, we use a fast and accurate Padé approximation formulation to calculate the polarizability tensors of stem cells for any contrast value between their dielectric permittivity and the dielectric permittivity of

their environment. We also performed statistical analysis of our computational results to identify which environment generates cells with similar electric properties. The computational analysis and the results reported herein can be used for shedding light on the response of stem cells to electric fields in applications such as dielectrophoresis and electroporation and for calculating the electric properties of similar biological structures with complex 3D shapes.

2.2   Introduction

Accurate characterization of a cell's morphology is crucial in many applications such as quantifying cellular responses under the influence of extracellular signals [6]. This is why morphological cell analysis has proved to play a significant role in many applications of biomedical engineering. Cytopathology or the science of diagnosis based on a single cell or a cell cluster is established on the subjective interpretation of cell morphological features by cytopathologists [7]. These morphological characteristics have numerous applications [8]–[16]. For example, cancerous cells exhibit micro-morphological changes through the different stages of tumorigenesis [8], apoptosis [9], cell division, and proliferation [10]. These changes can be detected by comparing the morphological features of normal cells with that of the cancerous cells at different stages, and hence open up a broad field of early cancer detection. Physiological fluctuations in reproductive function or cell classification based on their functionality can also be achieved by quantifying the morphological characteristics of a cell [11]–[13]. Dynamic feature extraction, to dissect cellular heterogeneity or the development of new drugs are other examples of applications that utilize the cell's morphological characteristics [14], [15]. As a result, cell imaging is an essential analysis tool in the field of cell cytology, neurobiology, pharmacology and biomedical research disciplines [16].

The physical interactions between the cell and the extracellular environment, in which the cells are embedded, have a significant effect on the shape of the cell [17]. Recent advancement in three-dimensional microenvironment engineering have enabled researchers to mimic the real in vivo conditions [18]–[20]. By engineering the biomaterial scaffold culture, researchers have been able to achieve desired cell shapes and hence control the cell's functionality [21]–[24]. Culturing the same cell in different biomaterial scaffolds leads to variation in the cell morphology. Florczyk et al. referred to this as cellular morphotyping, where they incorporated a cell line of human bone marrow stromal cells (hBMSCs) cultured in different microenvironments [25]. The present study draws upon on a database, recently developed by the National Institute of Standard and Technology (NIST), consisting of the 3D surface and volumetric map of stem cells grown in different environments. The motivation behind developing that database was to shed light upon the effect of the cell's microenvironment on its 3D morphological features [26]. The database is accessible via an open source interactive user interface [27] and available in *.obj* (wavefront) format and volumetric mesh format (*voxels*) for future studies [28]. The cells were divided into ten groups based on the microenvironments in which they were grown. Microenvironments with different geometrical and/or chemical properties were constructed to guide the cell's morphology to have characteristic shapes such as elongated, columnar, or equi-axial shapes [29]. The cells were imaged using confocal laser scanning microscopy, which generated a stack of 2D slices or cross sections for each cell [30]. The substantial number of 2D images (z-stacks) were then categorized as foreground or background by applying an automated segmentation algorithm. The wide variability in cell morphologies was introduced by carefully engineering the scaffolds, where the stem cells were grown, to mimic different natural environments for the

stem cells. Fig. 2.1 shows one cell from each of the ten families studied in the database. As shown in the figure, the cells exhibit a wide range of variation in morphology. For example, one cell morphology has an equi-axial sphere-like distribution (MG) whereas another cell is distributed along only one axis and is more similar to a 1D rod like structure (NF).

Florczyk *et al.* incorporated 82 different shape measures to assess the effect of the environment on the morphological features of the cell [25]. For determining cellular dimensionality, they organized the cells in a cellular dimensionality plot where each cell is assigned a coordinate based on ratios of elements in its radius of gyration tensor. The relative
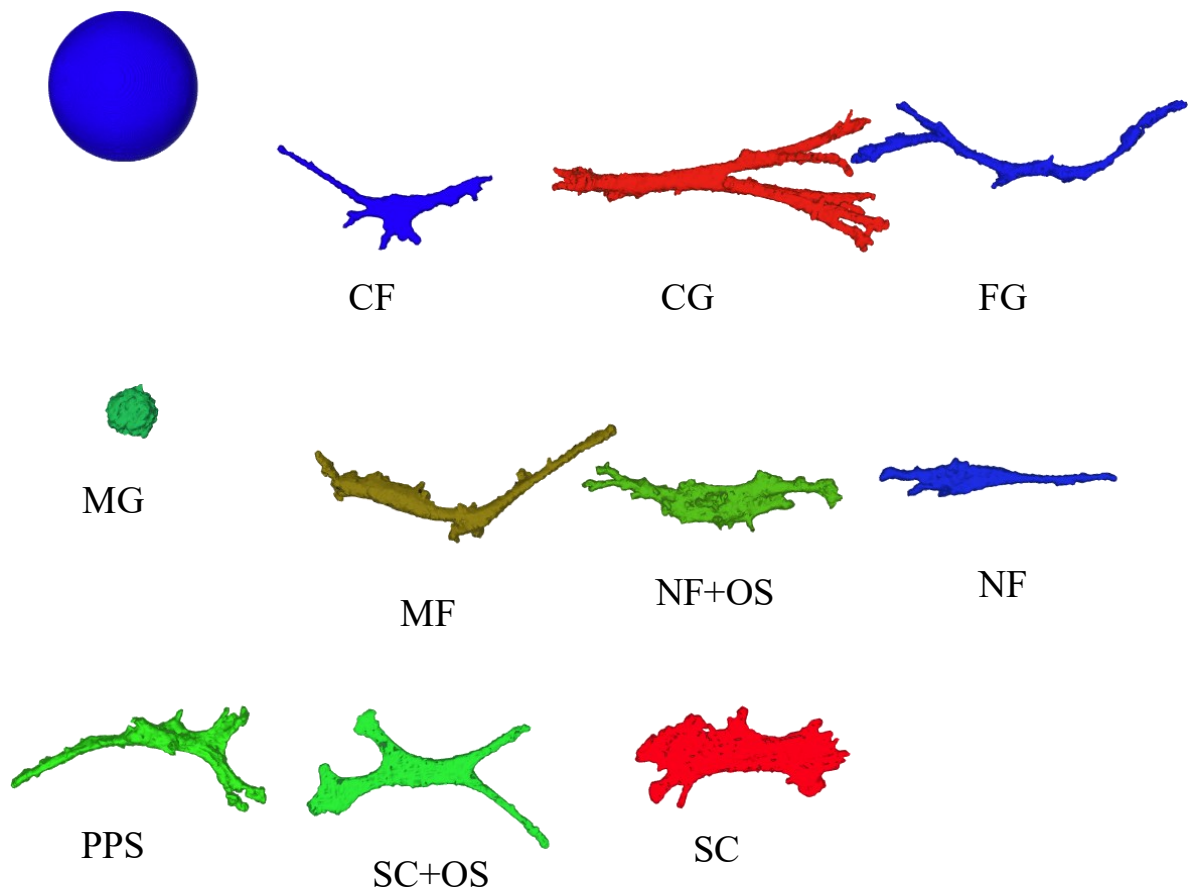
Figure 2.1 Morphological depiction of ten different cells from each family with blue sphere in serves as a size scale of 100 μm diameter sphere

location of each cell in this dimensionality plot defines the cell's properties and allows us to predict the scaffold's characteristics. For example, the question of whether the culturing medium is flat (2D) or whether it possesses 3D features or pores can be assessed from the smallest element of the gyration tensor. For a cell cultured on a 3D substrate, the smallest gyration tensor element was much larger than that of cells cultured on a 2D substrate, which would cause one diagonal element to be close to zero. Hierarchical Cluster Analysis (HCA) and Principle Component Analysis (PCA) were also incorporated for the statistical analysis of the dimensionality data [25]. However, the PCA and HCA analysis were incapable of identifying the scaffold of single cells due to the large heterogeneity in the cell shapes and the resulting heterogeneity in the dimensionality data.

Betancourt *et al.* recently employed the numerical path integrator ZENO to calculate the DC electric polarizabilities of the stem cells from the same database [29]. ZENO uses random walks to calculate the electric polarizability, capacitance and intrinsic viscosity of arbitrary shaped particles [31], [32]. The mathematical foundation of ZENO's random walk calculations automatically assign infinite contrast to the studied particle. That is, the polarizability of objects with arbitrary contrast cannot be calculated using ZENO. Therefore, the study of Pazmiño et al. only considers the electric polarizability tensor, the limiting situation in which stem cells are assumed to be perfect conductors. The reported results provide insight into how the local microenvironment of cells can influence how they react to an electric field stimulus. However, in vitro studies and several numerical studies emphasizes that we should incorporate non-ideal cases in cell polarizability studies [33]–[37]. For example, Sebastián *et al.* employed an adaptive finite element numerical approach to calculate the complex polarizability of realistic red blood cells by calculating the electric field distribution

inside the membrane and using the effective dipole element method [38]. They concluded that the polarizability of the cell calculated using anisotropic properties can be significantly different from that of the cell calculated using isotropic properties. They also used the same approach to determine the complex polarizability of four types of hematic cells: T-lymphocytes, platelets, erythrocytes, and type-II stomatocytes [36]. Prodan *et al.* developed a theoretical framework to explain the accumulation of surface charge over the cell membrane boundary in suspension (i.e. known as α- relaxation process in <10 kHz range and β- relaxation process at higher frequencies) by calculating the complex polarizability of a single shelled spherical cell (shell representing the membrane) [37]. Di Biasio *et al.* extended the polarizability expression to account for shape variability (i.e. ellipsoidal, toroidal) [34], [35]. Experimental validation of their model was presented by studying the low-frequency dielectric dispersion (α- dispersion) of *E. coli* bacteria cell in suspension [33].

For a more accurate assessment of the stem cells' response to an electric stimulus, computational techniques need to be developed that can calculate the polarizability of these complex stem cells using their true electrical properties. Moreover, since no closed form expressions exist for the polarizability of these complex-shaped stem cells, multiple independent computational techniques need to be tested to validate the accuracy of the calculated polarizabilities. The stem cells database provided at least five different representations for each cell with different resolutions. The resolution varied from the highest value, obtained directly from the raw confocal microscope images, down to the lowest value, which was 16 times coarser than the original value (details below). The highest resolution provides the most accurate representation of the true shape of the stem cell. However, it contains an extremely large number of discretization elements that can lead to prohibitively

14

large computational time in some numerical techniques. In most of the reported numerical experiments, the representations with moderate resolution were used to describe the stem cells [29].

The goal of this work is to extend these recent studies by addressing these challenges. Due to the complexity of the morphologies of these cells, we have incorporated three independent computational methods to calculate the polarizability tensors and validated our result through the excellent agreement in the numerical results achieved by the three techniques. We also adapted these computational techniques to calculate the polarizability tensors of the stem cells at an arbitrary contrast between their electric properties and the electric properties of the environment. This allows us to predict more accurately the response of stem cells, with realistic electric properties, to an arbitrary electric stimulus. After validating our calculations, we quantified the relationship between the polarizability tensors and the cell shapes. We also clarified the variations in the polarizability values with the variations in the meshing resolution used to describe each stem cell. Finally, we used a simple Páde approximation technique that employs the numerical results in two cases of extreme electrical contrast between a cell and its environment to calculate, with high accuracy, the polarizability tensors of stem cells with uniform but arbitrary electrical properties.

This section is arranged as follows: In subsection 2.3, we briefly describe the NIST stem cells database and the various microenvironments used to generate this database, we briefly introduce the theory behind the static polarizability calculation, and we describe the three numerical techniques employed in this work. In subsection 2.4, we present the polarizability results obtained from the different solvers. These results are discussed and conclusions drawn in subsections 2.5 and 2.6 respectively.

15

2.3   Methodology

2.3.1   NIST 3D Stem Cell Database

In the NIST stem cell database, ten different scaffold families were employed [25], [26]. The scaffold families can be divided into five major categories based on their geometry and material composition (all names taken from the NIST database):

(a) Spun-Coat (SC), Nanofiber (NF), and Microfibers (MF)

Spun-Coat (SC), Nanofiber (NF), and Microfibers (MF) scaffolds were made from the poly(ε-caprolactone) (PCL) polymer. The Spun-Coat scaffold was composed of flat films of PCL that provided a 2D environment. The Nanofiber and Microfiber scaffolds consisted of electrospun fibers with different sizes creating a complex porous 3D environment. The fibers in the Nanofiber category had a diameter of 589 nm and the fibers employed in the Microfiber category were 4.4 μm in diameter [25], [26].

(b) Matrigel (MG), Collagen Gel (CG), and Fibrin Gel (FG)

Matriigel (MG), Collagen Gel (CG), and Fibrin Gel (FG) scaffolds were composed of hydrogels obtained from three different natural sources. Fibrin Gel was composed of fibrinogen obtained from human plasma and Collagen gel was obtained from bovine Type I collagen [25], [26]. Matrigel scaffolds were obtained from the secretions of mice sarcoma cells. These three families formed porous 3D environments for the stem cells

(c) Collagen Fibrils (CF)

Collagen Fibrils (CF) scaffolds were obtained from bovine collagen similar to Collagen Gel. However, Collagen Gel was allowed to form a 3D porous gel structure whereas collagen fibrils were confined to a 2D film forming 200 nm diameter collagen fibers [25], [26].

(d) Spun-Coat + Osteogenic Supplements (SC+OS) and Nanofiber + Osteogenic Supplements (NF+OS)

Spun-Coat + Osteogenic Supplements (SC+OS) and Nanofiber + Osteogenic Supplements (NF+OS) scaffolds were geometrically identical to the SC and NF scaffolds, respectively. However, Osteogenic Supplements were added to the SC and NF scaffolds to form the SC+OS and NF+OS scaffolds. Therefore, by comparing the stem cells grown in the SC+OS scaffolds with the stem cells grown in the SC scaffolds, we can assess whether the chemical composition of the environment has an effect on cell shape or whether the geometry of the environment is the sole regulator of cell shape [25], [26].

(e) Porous polystyrene scaffold (PPS)

Porous polystyrene scaffold (PPS) scaffolds were composed of polystyrene and they represent one of the most commonly used 3D cell cultures [25], [26]. Unlike the NF and MF scaffolds, PPS is not composed of cylindrical fibers but is typically composed of more flattened ribbons. In PPS scaffolds, the pores range from 36 μm to 40 μm [25].

Approximately 100 different stems cells were imaged from each environment. Each cell was provided with a unique identifier. We started our numerical experiments by studying ten different cell shapes, one cell shape from each of the ten environments. The identifiers of the selected stem cells are summarized in Table 2.1 and taken from [25].

Table 2.1 Identifiers of the ten cell shapes used in this study

Scaffold Environment	Cell Identifier
SC	080613_SJF_SC1_d1_63x_12
NF	080713_SJF_NF1_d1_63x_18
MF	012014_SJF_BigNF_1d_63x_25

MG	022614_SJF_Matrigel_1d_63x_05
CG	050214_SJF_Collagen Gel_1d_63x_02
FG	040114_SJF_Fibrin Gel_1d_63x_07
CF	010914_SJF_Coll_Fibrils_1d_63x_2_05
SC+OS	091313_SJF_SC+OS_d1_63x_18
NF+OS	091613_SJF_NF+OS_d1_63x_08
PPS	012314_SJF_Alvetex_1d_63x_13

Each cell was stained for actin and nucleus for obtaining the morphology of cell cytoplasm and nucleus separately [25], [28]. Both the cell cytoplasm and the nucleus shape data are available in two different formats for user convenience: *(i)* the original voxel representation of the segmented cell image and *(ii)* triangular surface mesh representation obtained via the Marching Cubes algorithm from the original voxel representation and down-sampled representations. The triangular mesh representation is available in five different versions, each version down-sampled by a factor that ranges from 1 to 16 in powers of two [28]. For example, the "*down4*" mesh was generated by first representing each 4 pixels of the original cell morphology in each image in the stack of images defining the cell with one larger pixel, then operating with the Marching Cubes algorithm. Clearly, the "*down1*" mesh was generated from the original unchanged voxels. Fig. 2.2 depicts how down-sampling affects the actual morphology of a particular cell (in this case PPS). As can be observed from Fig. 2.2 and the associated data, down sampling the original mesh decreases the resolution of the original morphology and increases the stem cell's volume and surface area.

Format	Voxel	Down1	Down2	Down4	Down8	Down16

100 μm

	Voxel	Down1	Down2	Down4	Down8	Down16
No. of Vertices	—	36146	12972	4958	2126	1022
No. of Faces	—	72352	25968	9908	4248	2040
Surface Area (μm^2)	—	11395	10702	10627	11935	14684
Volume (μm^3)	14960	17857	19798	23895	32123	48348

Figure 2.2 Illustration of the raw voxels and the five different surface meshes of a PPS cell down sampled by factors from 1 to 16.

2.3.2 Theory of Electrostatic Polarizability

The inclusion of an isotropic or anisotropic particle in a homogenous environment, excited by a uniform electric field, will perturb this electric field in the vicinity of the inclusion [39]. The incident electric field will lead to the separation of charges on the surface of the particle, creating an overall dipole moment. The ratio between the induced dipole moment, p, and the incident electric field, E, is defined as the polarizability (α) of the particle. The polarizability α is a direct function of the shape, the electric properties of the particle, and the

19

electric properties of the environment where the particle is embedded. Closed form expressions for the polarizability of simple shapes, like spheres and ellipsoids, are relatively easy to obtain because of the uniform distribution of the internal field [40], [41]. However, for stem cells with complex 3D geometries, the polarizability calculation is only possible via a numerical solution of the Laplace equation [39] (depicted in (2.1)):

$$\nabla^2 \phi(r) = 0 \tag{2.1}$$

In (1), ϕ is a sum of the incident potential ϕ_e and the perturbed potential caused by the presence of the particle. For a randomly oriented inclusion with no planes of symmetry, the polarizability tensor will have in general nine non-zero elements, α_{ij}. However, the polarizability tensor is symmetric with a maximum of six independent components. By using matrix diagonalization, we can obtain the diagonalized form of the tensor (as shown in (2.2)), which can be achieved when the major axes of the particle are aligned with the principal axes of the coordinate system, x, y, and z [42]

$$\alpha = \begin{bmatrix} \alpha_{xx} & \alpha_{xy} & \alpha_{xz} \\ \alpha_{yx} & \alpha_{yy} & \alpha_{yz} \\ \alpha_{zx} & \alpha_{zy} & \alpha_{zz} \end{bmatrix} \xrightarrow{Diagonalization} \hat{\alpha} = \begin{bmatrix} \hat{\alpha}_{xx} & 0 & 0 \\ 0 & \hat{\alpha}_{yy} & 0 \\ 0 & 0 & \hat{\alpha}_{zz} \end{bmatrix} \tag{2.2}$$

Some symmetrical morphologies will have degenerate diagonal components, e.g. $\hat{\alpha}_{xx} = \hat{\alpha}_{yy}$. However, the following analysis will be the same. Theoretically, the polarizability of a particle for arbitrary values for ϵ_p and ϵ_m can be calculated using (2.3) [39]:

$$\alpha_{ij} = \left(\frac{\epsilon_p}{\epsilon_m} - 1\right) \int_V \hat{j}. E_i dV \tag{2.3}$$

where, j is selectively varied to x, y, and z based on the polarizability element of interest, i is determined by the direction of the incident field, and V is the volume of the inclusion. Different

components of the polarizability tensor can be calculated by varying the direction of the incident electric field and by selecting different components of the electric field inside the particle E_i. The electric polarizability tensor, $[\alpha_E]$, can be calculated by assigning infinity to the relative permittivity of the particle ($\epsilon_p = \infty$). For the case of a perfect conductor, the electric field is normal to the surface of the particle, see Fig. 2.3(a), and the electric field inside the particle diminishes to zero. This will make the integral in (2.3) undefined and, therefore, the surface integral form of (2.3) is preferred for calculating α_{ij} for the case of $\epsilon_p = \infty$ [42].

The magnetic polarizability tensor, $[\alpha_M]$, can also be calculated using (2.3) by assigning zero to the relative dielectric permittivity of the particle ($\epsilon_p = 0$). As shown in Fig. 2.3(b), this ϵ_p choice diminishes the normal component of the electric field at the surface of the particle but the tangential field component will be then nonzero. Since (2.3) does not have a closed form solution for particles with complex shapes, different numerical techniques need to be employed to validate each other. Practically, there is no particle with infinite or zero relative permittivity and moreover, biological cells will have some finite contrast depending on the type of cell and its surrounding medium. The theory of electric and magnetic polarizabilities is employed considering two extreme hypothetical cases to manipulate the normal and tangential field components on a particle surface. As we will discuss in detail in section 2.4.5, we can invoke close form approximation (Padé approximation) to calculate the electrical properties of a particle at any finite/practical contrast if we know the electric and magnetic polarizabilities at the two theoretical extremes.
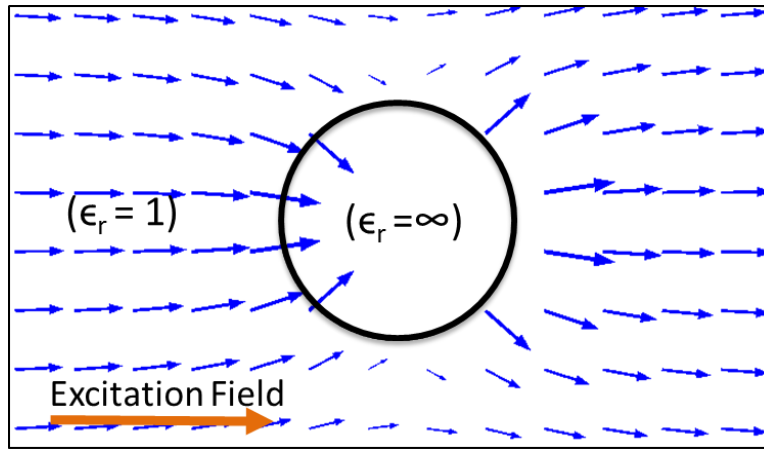
(a) Perfect Electric Conductor
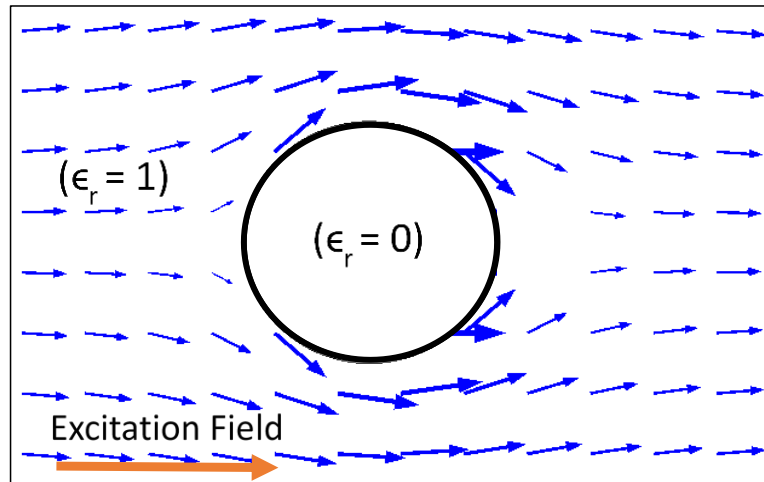
(b) Perfect Magnetic Conductor

Figure 2.3 Electric field distribution along the surface of a body with (a) perfect electric conductor (PEC), (b) perfect magnetic conductor (PMC) properties

2.3.2.1 *COMSOL Multiphyscis[1]*

COMSOL is a commercial multi-physics software package that uses the Finite Element Method (FEM) to calculate the desired physical properties [43]. FEM solvers like COMSOL

---

[1] Certain commercial equipment and/or materials are identified in this report in order to adequately specify the experimental procedure. In no case does such identification imply recommendation or endorsement by the National Institute of Standards and Technology, nor

require the geometry of interest to be subdivided into smaller volumetric elements (e.g. tetrahedrals, pyramids, or prisms) and solves the desired equations at every volumetric element under appropriate boundary conditions [43]. In this work, we used the Electrostatics physics interface under the AC/DC COMSOL module for our problem definition. This module uses FEM to solve Maxwell's equations under the static approximation [44]. The stem cell database contains the surface mesh of each cell morphology in the wavefront *.obj* format. We converted the cell mesh into STL (*STereoLithography*) format using MeshLab [45] to facilitate the import of the cells' geometries into COMSOL. COMSOL uses this STL mesh to define the surface or the outer boundary of the stem cell. COMSOL would then mesh the volume enclosed by this surface into volumetric tetrahedral elements [44]. To ensure the accuracy of the imported mesh, we validated that the number of faces in the outer surface of the stem cell did not change from the original values after it was imported to COMSOL. We also confirmed that the volume of the imported cell calculated by COMSOL matched the original volume of the cell as calculated by MeshLab. The cells were embedded in a large sphere whose radius was at least 25 times the size of the imported cell to replicate free space conditions. The medium enclosed by that bounding sphere was assigned a relative permittivity of unity, $\epsilon_m = 1$, and the material inside the cell was assigned a variable permittivity ϵ_p based on the polarizability tensor of interest.

2.3.2.2   *Scuff-EM*

Scuff-EM (Surface CUrrent/Field Formulation of ElectroMagnetism) is an open source Method of Moment (MoM) solver for static and dynamic electromagnetic scattering [46].

---

does it imply that the equipment and/or materials used are necessarily the best available for the purpose.

Scuff-EM requires the particles to be represented in *.msh* format which can be generated from the STL representation of the stem cells using the open source mesh generator Gmsh [47]. *Scuff-Static* is the static subroutine in the Scuff-EM package and the fundamental equation for this subroutine is depicted in (4) below:

$$\emptyset(\boldsymbol{r}) = \emptyset^{ext}(\boldsymbol{r}) + \frac{1}{4\pi\epsilon_0}\sum_s \oiint \frac{1}{|x-x'|}\sigma(\boldsymbol{r'})d\boldsymbol{r'} \qquad (2.4a)$$

$$E(\boldsymbol{r}) = E^{ext}(\boldsymbol{r}) + \frac{1}{4\pi\epsilon_0}\sum_s \oiint \frac{(r-r')}{|r-r'|^3}\sigma(\boldsymbol{r'})d\boldsymbol{r'} \qquad (2.4b)$$

In (2.4), $\boldsymbol{r}$ is the position vector of a point over the surface of s, $\emptyset^{ext}(\boldsymbol{r})$ and $E^{ext}(\boldsymbol{r})$ are the potential and field due to external stimulus and $\sigma(\boldsymbol{r'})$ is the surface charge density. The static physics equations are solved at every vertex of the *.msh* file and then combined through the integration in (2.4) to represent the actual morphological characteristics. The integral is taken over all particle surfaces in the problem and we do not need to apply a bounding sphere as in case of the COMSOL solver [46].

The stem cell surface mesh representations obtained from [28] were not centered around the origin (*0, 0, 0*) in 3D coordinate system. Therefore, we obtained the center of mass of the cell from MeshLab [45], assuming a uniform density for the stem cell, and applied translational operations to re-center the cell at the origin before forwarding the mesh to Scuff-EM for the calculation of the polarizability tensor.

2.3.2.3 *NIST Finite Element Method Using Voxel Representation*

An open source finite difference and finite element package was developed at NIST to calculate the linear and elastic properties of heterogeneous random materials [48]. The package was developed to be versatile enough for a wide range of applications such as the calculation

of the effective properties of random mixtures and composites such as concrete [48]. The package requires the discretization of the object into cubical voxels and therefore was able to operate directly on the voxel representation of the stem cells (see Fig. 2.2). The accuracy of the package has been validated in a wide variety of applications [49]–[51]. It was used as a third method to crosscheck the polarizability values calculated using the COMSOL and SCUFF-EM packages. This solver will be designated as NIST FEM for the remainder of this paper.

The three solvers discussed in this work employ different numerical recipes for the calculation of the polarizability. For example, Scuff-EM uses a surface mesh because it is based on the integral form of Maxwell's equations whereas COMSOL and the NIST FEM use a volumetric mesh since they employ the differential form of Maxwell's equations [52]. However, if a fine-enough mesh is employed, the three methods should yield the same polarizability values since they are solving identical Maxwell's equations for a stem cell with an identical shape and electric properties. The agreement between the three techniques is enforced by the Uniqueness theorem, which states that only one solution can satisfy Maxwell's equations and the boundary conditions of the problem regardless of the numerical technique that is used to achieve this solution [40]. This justifies our approach to compare different solvers to confirm validity of our results. With the variability in the computational domain, the different resolutions of the cell images compatible with corresponding platform is listed in Table 2.2. Besides, we were also concerned about the computational time and resources each simulation occupied which is listed in tabular form for a cell shape (PPS) in Table 2.3[2].

---

[2] All computational times were measured on an Intel Xeon Processor E5-2687W with 20 MB Cache and 3.10 GHz processor base frequency. The values in the table only shows the run time

Table 2.2 Solvers used for various stem cell representations

Solver	Voxel	Down1	Down2	Down4	Down8	Down16
NIST FEM	√					
COMSOL FEM				√	√	√
Scuff-EM		√	√	√	√	√

Table 2.3 Approximate computational time for PPS in hours

Solver	Voxel	Down1	Down2	Down4	Down8	Down16
NIST FEM	5.3	N/A	N/A	N/A	N/A	N/A
COMSOL FEM	N/A	N/A	N/A	21	5	0.65
Scuff-EM	N/A	36	2.6	0.08	0.01	2.6×10^{-3}

2.3.3 Polarizability Tensors of Simple Cell Shapes

To cross-validate the results of these three techniques, we started by calculating the polarizability tensor of a simple sphere whose polarizability tensor is analytically well-known. Due to its symmetry, a sphere has a diagonal polarizability tensor where the three components are identical and equal to *3* for a sphere with unit volume [39]. Note all the polarizability tensor elements reported in this paper are normalized by particle volume. This simple experiment will help us identify the meshing resolution needed for the accurate calculation of the polarizability tensor of a certain object. Fig. 2.4 shows the polarizability results versus the inverse of the number of meshing elements used in the calculation (*N*). As the number of meshing elements

of each solver. An additional ~ 1 hour was needed to adapt the format of each cell to formats that are compatible with each solver.

26

increases, the numerical values move towards, with complete agreement in the limit where N^{-1} converges to zero, which is equivalent to an infinite number of meshing elements leading to a continuous object.

For Scuff-EM, the number of elements is the number of triangular surface mesh elements and for COMSOL the number of elements is the number of volumetric tetrahedral mesh elements. Linear extrapolation to the $N \rightarrow \infty$ limit facilitates the accurate calculation of the polarizability values using a feasible number of meshing elements. Therefore, in both the COMSOL and Scuff-EM polarizability calculations, the simulations were performed at least two times, with different resolutions, before linear extrapolation was performed to improve the accuracy of the results. To explain the minor differences between COMSOL and Scuff-EM in Fig. 2.4, it is important to clarify that for both COMSOL and Scuff-EM, the geometry of the stem cell is described by its surface mesh representation. Scuff-EM uses this surface mesh directly to calculate the polarizability tensor. However, COMSOL converts this surface mesh into a volumetric mesh by dividing the medium inside and outside of the surface of the stem cell into volumetric tetrahedrals. Therefore, due to the differences in meshing, small geometrical differences can exist between the COMSOL and Scuff-EM, which can lead to small differences in the calculated polarizability values. However, these differences should diminish as the number of meshing elements is increased as shown in Fig. 2.4.
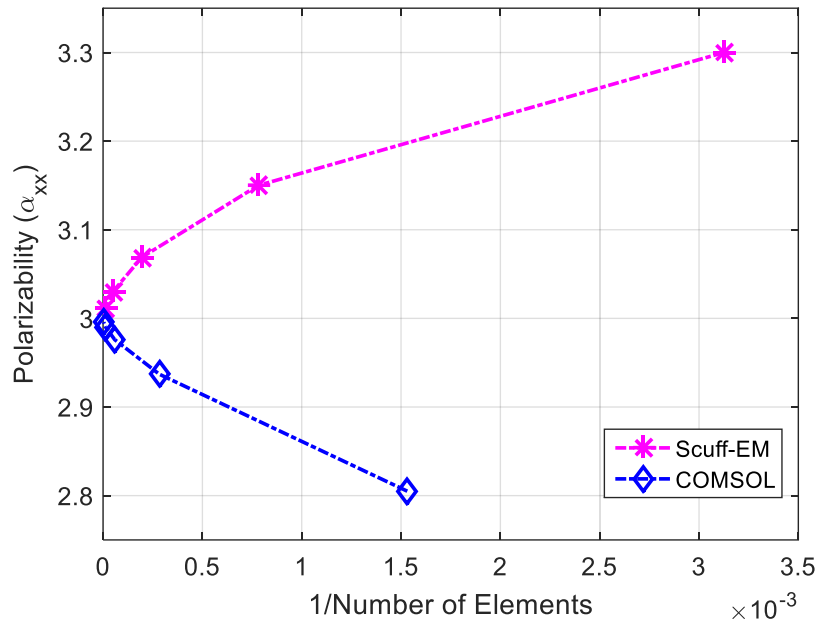
Figure 2.4 Depiction of the polarizability convergence between COMSOL and Scuff-EM for a unit sphere.

2.3.4 Electrostatic-Hydrodynamic Analogy

As depicted in Fig. 2.3(b), the electrical field line around a perfect magnetic conductor is tangential to the surface of the inclusion, which exactly resembles the fluid movement around an insoluble object in a dilute suspension. The fact that electrical field lines around such an inclusion in a dielectric medium is analogous to the fluid movement along a particle in hydrodynamics forms the basis of the Electrostatic-Hydrodynamic analogy [32], [53]. According to this analogy, the intrinsic diffusivity and the intrinsic viscosity of the stem cell can be estimated using the trace of the magnetic and electric polarizability tensors, respectively, as summarized in Table 2.4 [42], [54]. The improvement of the approximation in Table 2.4 can be achieved by using the whole polarizability tensor as discussed in [55].

Table 2.4 Hydrodynamic−Electrostatic analogy

Hydrodynamic properties	Electrostatic properties	Formulae
Intrinsic Viscosity $[\eta]$	Electric polarizability $[\alpha_E]$	$[\eta] \approx \dfrac{5}{6}[\sigma_\infty] = \dfrac{5}{6}\dfrac{tr[\alpha_E]}{3}$
Intrinsic Diffusivity $[D_s]$	Magnetic polarizability $[\alpha_M]$	$[D_s] = [\sigma_0] = \dfrac{tr[\alpha_M]}{3}$

2.4   Result

2.4.1   Validations of the Polarizability Calculations Using Different Solvers

Different solvers require different representations of the cell geometry. For example, NIST FEM requires the volumetric raw voxel representation whereas the Scuff-EM solver requires the STL surface mesh representation. The raw voxel representation of the cell's morphology was converted to a *stereolithography* (STL) surface mesh with varying levels of resolution. The "*down1*" representation has the highest resolution and is closest to the raw *voxel* representation of the cell. The "*down16*" representation has the lowest resolution and the fewest number of surface triangles. Therefore, for an accurate comparison between the NIST FEM results and the Scuff-EM results in Table 2.5, the raw voxel representation was used for the NIST FEM[3] Package whereas the "*down1*" representation was used for Scuff-EM[4]. Even though the "*down1*" surface mesh is close to the volumetric raw voxels, there are still some differences between the two representations. To illustrate these differences, Table 2.6 shows a comparison between the volume of the volumetric raw *voxel* representation and the "*down1*"

---

[3] NIST FEM was performed on the *voxel* representation of each cell morphology.

[4] Scuff-EM was performed on the "*down1*" representation of the surface mesh of each cell.

surface mesh representation of the cells. The percentage variation in the volume between the two representations exceeded 20 % for some cell representations. For these cells, the relative differences between the polarizability values calculated using the NIST FEM package and the Scuff-EM solver are comparable to the differences in the volume of the two representations. Table 2.5 shows the comparison between the diagonalized electric and magnetic polarizability tensors calculated using the NIST FEM and Scuff-EM solvers. Each family name corresponds to the cell morphology listed in Table 2.1. The polarizability values are dimensionless since they are normalized by the volume of each respective cell. Additional columns in Table 2.5 list the relative percent difference between these values as calculated using (2.5):

$$\% \, Difference = \frac{|\alpha_{Scuff-EM} - \alpha_{NIST-FEM}|}{\alpha_{Scuff-EM}} \times 100 \qquad (2.5)$$

We represent the diagonalized electric polarizability values in a descending order such that $P_1 \geq P_2 \geq P_3$. The maximum percentage uncertainty between the NIST FEM and the Scuff-EM results was 23.16 % as observed in the case of the electric, α_E, P_1 component of the FG stem cell.

Table 2.5 Diagonalized polarizability comparison between NIST FEM and Scuff-EM

Cell Family	α_E	NIST FEM	Scuff-EM	% diff-erence	α_M	NIST FEM	Scuff-EM	% diff-erence
PPS	P_1	124.16	109.51	13.39	M_1	-2.55	-2.39	6.83
	P_2	19.59	17.86	9.70	M_2	-1.94	-1.85	5.02
	P_3	4.43	4.61	3.86	M_3	-1.38	-1.32	4.75
Collagen Fibrils (CF)	P_1	106.62	105.09	1.46	M_1	-2.80	-2.52	10.90
	P_2	21.67	20.33	6.60	M_2	-1.65	-1.67	1.07
	P_3	1.99	2.44	18.34	M_3	-1.28	-1.31	2.50
Matrigel (MG)	P_1	4.31	4.50	4.14	M_1	-1.82	-1.76	3.28
	P_2	3.99	3.91	2.38	M_2	-1.58	-1.53	3.19

	P_3	3.05	2.94	3.49	M_3	-1.48	-1.43	3.53
Spun-Coat (SC)	P_1	59.09	52.88	11.74	M_1	-5.62	-4.68	20.19
	P_2	13.62	11.73	16.13	M_2	-1.35	-1.38	1.71
	P_3	1.54	1.80	14.38	M_3	-1.17	-1.15	2.09
Nanofiber (NF)	P_1	114.61	113.96	0.57	M_1	-2.81	-2.51	11.70
	P_2	4.17	3.85	8.39	M_2	-1.83	-1.84	0.58
	P_3	2.14	2.50	14.61	M_3	-1.13	-1.15	1.33
SC+OS	P_1	121.97	111.8	9.10	M_1	-3.62	-3.06	18.20
	P_2	31.96	27.43	16.51	M_2	-1.5	-1.55	3.36
	P_3	1.74	2.15	19.07	M_3	-1.24	-1.26	1.68
NF+OS	P_1	92.65	84.06	10.21	M_1	-3.25	-2.91	11.43
	P_2	7.44	6.88	8.14	M_2	-1.7	-1.65	2.71
	P_3	2.41	2.58	6.75	M_3	-1.22	-1.23	0.37
Collagen Gel (CG)	P_1	221.18	192.0	15.20	M_1	-2.8	-2.76	1.37
	P_2	25.38	22.56	12.51	M_2	-1.71	-1.62	5.89
	P_3	10.55	9.24	14.10	M_3	-1.26	-1.05	20.22
Fibrin Gel (FG)	P_1	369.33	299.88	23.16	M_1	-2.25	-2.15	4.51
	P_2	25.68	21.76	18.04	M_2	-1.99	-1.83	8.46
	P_3	8.92	7.93	12.58	M_3	-1.40	-1.19	17.63
Microfiber (MF)	P_1	136.94	129.9	5.42	M_1	-2.27	-2.22	2.47
	P_2	17.34	16.36	5.97	M_2	-1.75	-1.67	5.37
	P_3	5.03	5.09	1.12	M_3	-1.51	-1.44	4.88

This difference in the P_1 value is justifiable given that the difference in volume between the volumetric raw voxel representation and the surface mesh representation was 21 % as shown in Table 2.6. The diagonalized magnetic polarizability values M_1, M_2, and M_3 are also shown in Table 2.5 arranged such that $M_1 \geq M_2 \geq M_3$. The maximum difference for the magnetic polarizability values was 20.22 % as observed in the P_3 component of the CG cell, which is

comparable to the 17.88 % difference in the volume of the two different representations used in the NIST FEM and the Scuff-EM packages.

Table 2.6 Comparison of volume of each cell measured from their *voxel* representation and "*down1*" surface mesh representation

Cell Family	PPS	CF	MG	SC	NF	SC+OS	NF+OS	CG	FG	MF
Voxel Volume (μm³)	14960	7128	11965	21162	8315	13074	16247	20157	8036	17880
Mesh Volume ["*down1*"] (μm³)	17857	8701	13048	27129	9864	17007	19433	24547	10199	20634
% Variation	16.2 %	18.1 %	8.30 %	22.0 %	15.7 %	23.1 %	16.4 %	17.9 %	21.2 %	13.4 %

As an additional independent validation step, Table VII compares the polarizability values calculated using the FEM package COMSOL and the Scuff-EM package. In this comparison, the percentage uncertainty is defined as (2.6):

$$\% \ Difference = \frac{|\alpha_{Scuff-EM} - \alpha_{COMSOL}|}{\alpha_{Scuff-EM}} \ x \ 100 \qquad (2.6)$$

Both solvers used the "*down*4" representation and, therefore, the agreement was even better and the differences were less than 7 % for all of the cell shapes. Note that the difference between Table 2.7 and Table 2.5 is that Table 2.5 compares the polarizability values calculated by the NIST-FEM solver with the values calculated using the Scuff-EM solver. For Table 2.5, the "*down*1" mesh is used for Scuff-EM and the voxel representation is used for the NIST-FEM solver. Table 2.7, however, compares the polarizability values calculated using COMSOL with those calculated using Scuff-EM both using the "*down*4" mesh representation of the stem cells. The level of agreement between the three independent solvers summarized

32

in Table 2.5 and Table 2.7 adds further validity to the polarizability values reported in this work.

Table 2.7 Diagonalized polarizability comparison of "*down4*" mesh representation between Scuff-EM and COMSOL

Cell Family	α_E	NIST FEM	Scuff-EM	% diff-erence	α_M	NIST FEM	Scuff-EM	% diff-erence
PPS	P_1	86.426	84.461	2.27	M_1	-2.41	-2.44	0.95
	P_2	14.308	13.677	4.41	M_2	-1.73	-1.74	0.21
	P_3	3.344	3.212	3.93	M_3	-1.22	-1.25	2.16
Collagen Fibrils (CF)	P_1	85.726	80.264	6.37	M_1	-2.75	-2.78	1.2
	P_2	17.078	16.094	5.76	M_2	-1.49	-1.47	1.35
	P_3	1.776	1.703	4.14	M_3	-1.18	-1.17	0.8
Matrigel (MG)	P_1	3.743	3.638	2.81	M_1	-1.67	-1.67	0.14
	P_2	3.474	3.370	2.98	M_2	-1.48	-1.47	0.61
	P_3	2.766	2.680	3.11	M_3	-1.43	-1.42	0.32
Spun-Coat (SC)	P_1	47.097	46.065	2.19	M_1	-4.78	-4.86	1.73
	P_2	10.815	10.504	2.88	M_2	-1.27	-1.26	0.83
	P_3	1.459	1.426	2.26	M_3	-1.09	-1.10	0.69
Nanofiber (NF)	P_1	95.572	89.274	6.59	M_1	-2.63	-2.68	1.8
	P_2	3.679	3.538	3.85	M_2	-1.66	-1.64	1
	P_3	1.891	1.822	3.68	M_3	-1.10	-1.07	2.29
SC+OS	P_1	94.722	92.292	2.57	M_1	-3.26	-3.27	0.41
	P_2	23.793	23.635	0.66	M_2	-1.41	-1.36	3.33
	P_3	1.617	1.603	0.85	M_3	-1.18	-1.19	0.97
NF+OS	P_1	69.285	67.121	3.12	M_1	-3.00	-3.03	1.19
	P_2	5.718	5.515	3.56	M_2	-1.53	-1.49	2.21
	P_3	1.919	1.857	3.24	M_3	-1.15	-1.09	5.21
Collagen Gel (CG)	P_1	131.27	125.19	4.63	M_1	-2.31	-2.30	0.49
	P_2	15.595	15.164	2.76	M_2	-1.79	-1.77	0.99
	P_3	7.037	6.791	3.48	M_3	-1.14	-1.07	6.34

Fibrin Gel (FG)	P_1	212.89	206.42	3.04	M_1	-1.94	-2.02	3.94
	P_2	15.923	15.385	3.38	M_2	-1.75	-1.82	4.23
	P_3	5.846	5.618	3.9	M_3	-1.19	-1.24	4.68
Microfiber (MF)	P_1	99.210	92.633	6.63	M_1	-2.00	-1.99	0.26
	P_2	12.893	12.208	5.31	M_2	-1.74	-1.76	1.29
	P_3	3.898	3.739	4.08	M_3	-1.33	-1.38	3.44

One of the advantages of the NIST stem cell database, not a detriment, is that it provides varying resolution levels for each cell representation. Therefore, we were able to study the effect of the meshing resolution on the calculated values of the polarizability. Scuff-EM was used to calculate the polarizability tensors for all the meshing resolutions, "*down1*" to "*down16*", for the PPS stem cell. Fig. 2.5(a) – 2.5(c) depict the diagonalized electric polarizability values *P1*, *P2*, and *P3*, respectively, calculated for the PPS stem cell using surface meshes with varying resolutions. Since each mesh has a slightly different volume, the polarizability values were normalized with the volume of each respective mesh. For the case of the PPS stem cell, Fig. 2.5 shows that if the coarsest representation, "*down16*", is used, the value of P_1 drops by 49.4 % from the value calculated using the "*down1*" mesh. Similarly, P_2 and P_3 experienced a decrease of 38.85 % and 49.5 %, respectively, between "*down1*" and "*down16*". Other stem cells showed the same trend, where the diagonal polarizability components decreased as the mesh resolution became coarser. However, if we consider the ratios P_1/P_2 and P_1/P_3 as depicted in Fig. 2.5(d) and Fig. 2.5(e), respectively, a much smaller change in the ratios is exhibited as the meshing resolution becomes coarser. The results in Fig. 2.5 were achieved using the PPS stem cell but several other cell shapes showed a similar behavior but they were not included in Fig. 2.5 for conciseness. Therefore, we can conclude that the absolute polarizability values vary significantly with the resolution of the mesh, but

the polarizability ratios are less sensitive to the meshing resolution. Therefore, if accurate absolute values for the polarizabilities are required, the highest resolution should be used in the calculation. However, if only the ratios of the main polarizability components are required, a coarse meshing representation can provide a good estimate at significant savings in the computational time.

2.4.2 Elements of the Electric Polarizability Tensor

Another goal of this paper was to investigate different ways to visualize any correlations between the polarizability results and the shapes of the different stem cells. The diagonal elements of the electric polarizability tensor are always represented in descending order ($P_1 \geq P_2 \geq P_3$). A spherical cell would have $P_1 = P_2 = P_3$ due to its symmetry, with $\frac{P_1}{P_2} = \frac{P_1}{P_3} = 1$. The closer a stem cell is to being spherical, the closer its polarizability ratios P_1/P_2 and P_1/P_3 will be to unity. Similarly, a 2D circular disk would have $P_1 = P_2$ and both components will be significantly larger than the third component P_3 [48]. A 1D rod would have P_1 significantly larger than the other two components, P_2 and P_3, and if the rod has a circular cross section then $P_2 = P_3$. Therefore, a 2D plot having these two polarizability ratios as axes would effectively represent the shape and electrical behavior of any 3D object. Fig. 6 captures the effective dimensionality of the 10 different cell morphologies considered. The bottom left corner electrically represents a spherical cell having $\frac{P_1}{P_2} = \frac{P_1}{P_3} = 1$; likewise, the top left corner represents a 2D disk since $\frac{P_1}{P_2} = 1$ and $\frac{P_1}{P_3} \to \infty$ and top right corner represents a 1D rod having $\frac{P_1}{P_2} = \frac{P_1}{P_3} \to \infty$.
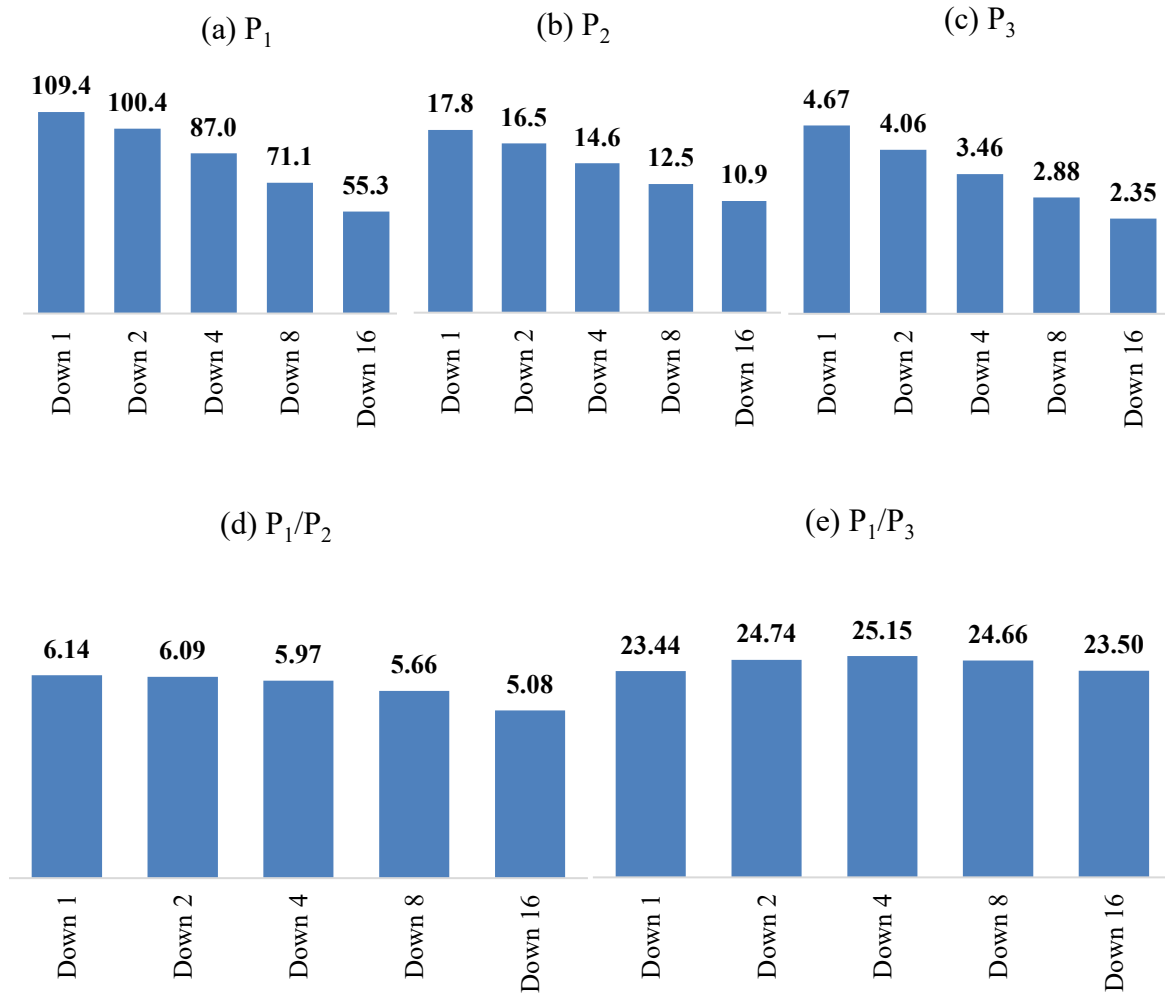
Figure 2.5 Histogram of diagonalized electric polarizability tensor of the PPS cell (for the specific cell identifier mentioned in Table 2.1

Cells cultured on planar substrates (SC+OS, CF, SC) were closest to the top left corner of the plot, electrically representing a 2D disk like behavior. Among the cells grown in 3D scaffolds (NF, NF+OS, MF, PPS, MG, FG, CG), MG-grown cells are closest to being spherical, indicating equi-axial morphology. The remaining substrate groups showed elongated morphologies with NF being closest to the 1D rod corner. Therefore, the polarizability ratios can be considered as alternative morphology specifiers, given that the diagonalized polarizability values are arranged in descending order ($P_1 \geq P_2 \geq P_3$), which is

equivalent to aligning the cell such that its major axis is parallel to the *x-axis*. The data in Fig. 2.6 were achieved using only 1 morphology per cell family as detailed in Table 2.1, and therefore the previous observations will be re-checked for a larger number of cells in the following sections.

Another visualization technique to present the data summarized in the three diagonalized components of the polarizability matrix can be performed by calculating the polarizability of the cell at different orientations. Rotating the cell along any of the axes will effectively alter the polarizability matrix since by rotating the cell we are altering the dimension and distribution of the original cell morphology. The resulting polarizability matrix after re-orienting the cell, *A′*, can be obtained by applying (2.7),

$$A' = RAR^T \tag{2.7}$$
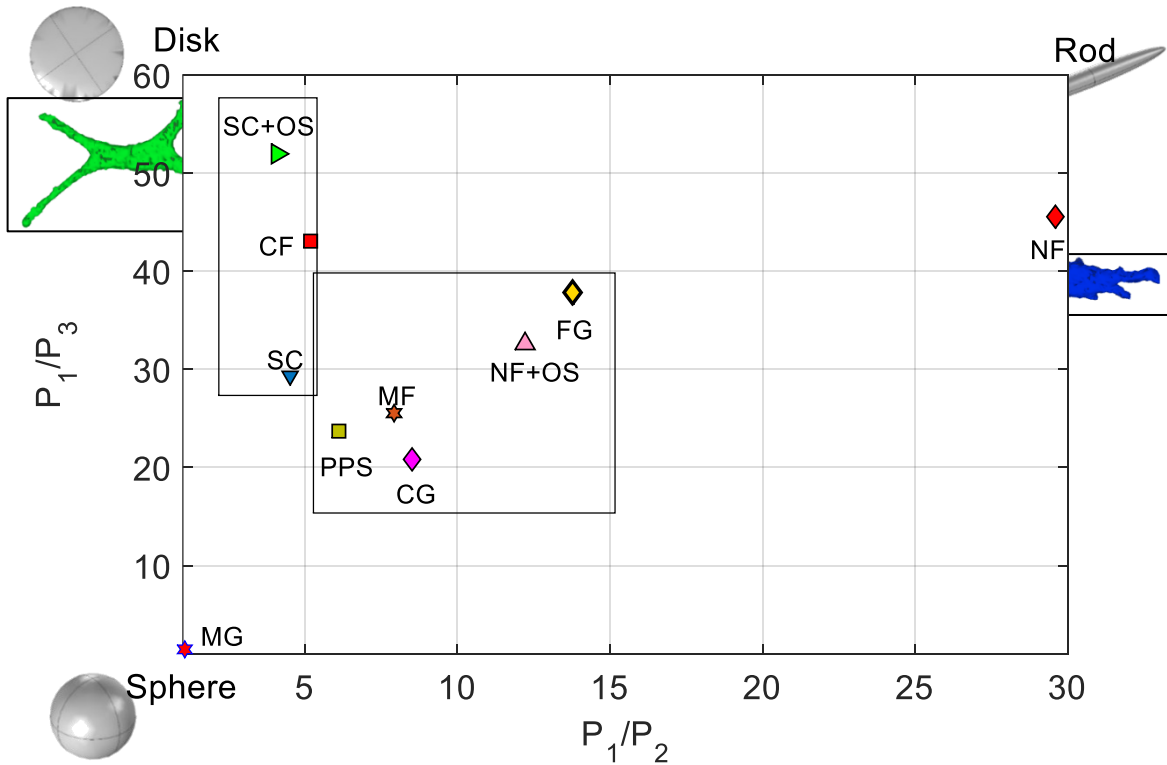
Figure 2.6 Encoding shape information from α_E

where A is the original polarizability matrix, R is the matrix for proper rotations and R^T is the transpose of R. For simplicity, let us assume P_1 is parallel to the *x-axis*, P_2 is parallel to the *y-axis,* and P_3 is parallel to the *z-axis* in the Cartesian coordinate system. If the cell is rotated around the *y-axis*, the rotation matrix can be designated as R_y and if the cell is rotated around the *z-axis* the rotation matrix can be designated as R_z. If the cell is rotated around both the *y-axis* and the *z-axis*, the effective rotation matrix can be expressed as (2.8):

$$R = R_y R_z = \begin{bmatrix} cos\beta & 0 & sin\beta \\ 0 & 1 & 0 \\ -sin\beta & 0 & cos\beta \end{bmatrix} \begin{bmatrix} cos\gamma & -sin\gamma & 0 \\ sin\gamma & cos\gamma & 0 \\ 0 & 0 & 1 \end{bmatrix}$$

$$= \begin{bmatrix} cos\beta cos\gamma & -cos\beta sin\gamma & sin\beta \\ sin\gamma & cos\gamma & 0 \\ -sin\beta cos\gamma & sin\beta sin\gamma & cos\beta \end{bmatrix} \tag{2.8}$$

where β = the angle of rotation around the *y-axis* and γ = the angle of rotation around the *z-axis.* The effective polarizability tensor A' can now be expressed as (2.9):

$$A' = \begin{bmatrix} cos\beta cos\gamma & -cos\beta sin\gamma & sin\beta \\ sin\gamma & cos\gamma & 0 \\ -sin\beta cos\gamma & sin\beta sin\gamma & cos\beta \end{bmatrix} X \begin{bmatrix} P_1 & 0 & 0 \\ 0 & P_2 & 0 \\ 0 & 0 & P_3 \end{bmatrix}$$

$$X \begin{bmatrix} cos\beta cos\gamma & sin\gamma & -sin\beta cos\gamma \\ -cos\beta sin\gamma & cos\gamma & sin\beta sin\gamma \\ sin\beta & 0 & cos\beta \end{bmatrix} \tag{2.9}$$

If we focus on only the *xx* component of the resultant polarizability matrix, it can be expressed as (2.10):

$$\alpha_{E_{xx}} = P_1 cos^2\beta cos^2\gamma + P_2 cos^2\beta sin^2\gamma + P_3 sin^2\beta \tag{2.10}$$

For a spherical cell, since $P_1 = P_2 = P_3 = 3$, $\alpha_{E_{xx}}$ will always have a constant value of three. For the case of an oblate ellipsoid or a 2D disk, $P_1 = P_2$, and therefore the resultant

$\alpha_{E_{xx}} = P_1 cos^2\beta + P_3 sin^2\beta$ will only vary with respect to β (rotation along *y-axis*). Equation (2.10) cannot be simplified further in case of a prolate ellipsoid or 1D rod like morphology since $P_1 >> P_2$ and $P_1 >> P_3$ implying that $\alpha_{E_{xx}}$ will vary for both β (rotation along *y-axis*) and γ (rotation along *z-axis*) for a 1D rod-like morphology. These observations can be used to interpret polarizability measurements from a single cell at multiple orientations to identify whether the cell is more spherical, more oblate-like, or more prolate-like in shape.

To clarify these observations, Fig. 2.7 shows a plot of $\alpha_{E_{xx}}$ from (2.10) for different cell types. In each subplot, the $\alpha_{E_{xx}}$ value is normalized by P_1 for different combination of β and γ values. Fig. 2.7(a) shows the case of a sphere and it is clear that the rotations around the *y-axis* or *z-axis* will have no impact on the value of $\alpha_{E_{xx}}$. Fig. 2.7(b) shows the "*stripes*" pattern typical of a 2D disk where the $\alpha_{E_{xx}}$ values will change with respect to rotation angles around the *y-axis* but will stay constant with rotations around the *z-axis*. This is why Fig. 2.7(b) is constant for different values of γ and varies with β. For a 1D prolate shape, the values of $\alpha_{E_{xx}}$ will vary with β and γ creating the rounded-square pattern shown in Fig. 2.7(c). Fig. 2.7(d) shows the value of $\alpha_{E_{xx}}$ due to the variations in β and γ, according to (2.10), for the Matrigel cell shape. By comparing Fig. 2.7(d) with Fig. 2.7(a), the polarizability values of Matrigel at multiple cell orientations can be used to infer its approximately spherical shape. In the case of the SC+OS cell, it has a flattened morphology with multiple rod-like protrusions and, therefore, we expect the polarizability behavior for multiple orientations to provide a pattern that is a hybrid of the oblate and prolate patterns. Fig. 2.7(e) shows the $\alpha_{E_{xx}}$ due to the variations in β and γ for the SC+OS cell and it is clear that the pattern is a hybrid of the pattern in Fig. 2.7(b) and that in Fig. 2.7(c). The NF cell shape is very close to that of a prolate ellipsoid and therefore

its $\alpha_{E_{xx}}$ pattern in Fig. 2.7(f) shows significant resemblance to that of a 1D prolate rod shown in Fig. 2.7(d).
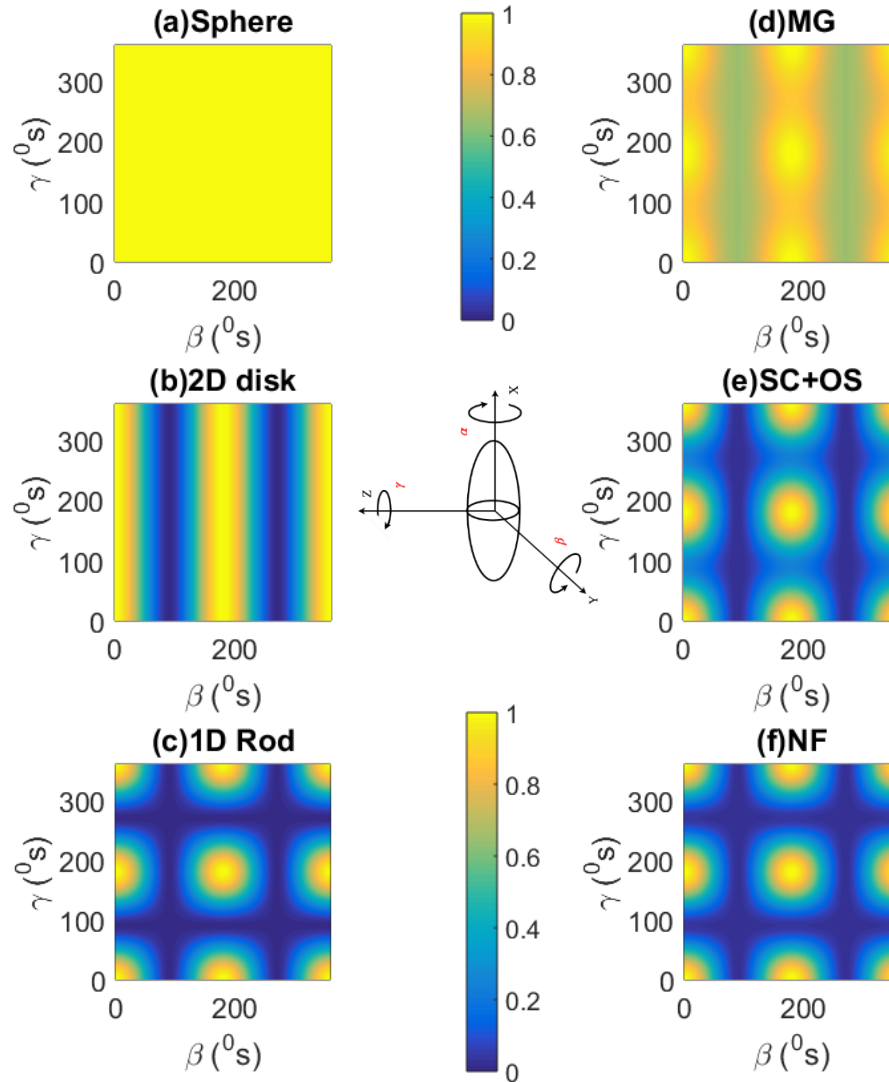
Figure 2.7 Pseudo-color (checkerboard) plot of $\alpha_{E_{xx}}$ normalized by P_1

It is important to emphasize that the previously described observations were achieved using only a single morphology from each cell family. Within each family, there is significant cell-to-cell variability and, therefore, a larger number of cells from each family needs to be examined before these observations can be converted into solid conclusions. However, the main contribution of this Section is to: (*i*) adapt multiple numerical techniques to accurately calculate the polarizabilities of highly complex stem cells, (*ii*) quantify how the polarizabilities depend on the resolution of the mesh used to represent the stem cell, and (*iii*) develop efficient techniques to visualize the variations in theses polarizabilities between different cells within the same family or in different families.

2.4.3   Elements of the Magnetic Polarizability Tensor

We also calculated the magnetic polarizability tensor (α_M) values, M_1, M_2, and M_3, and plotted the values for the 10 different cell shapes in Fig. 2.8. The diagonalized magnetic polarizability values were arranged in descending order $M_1 \geq M_2 \geq M_3$. Similar to Fig. 2.6, the *x-axis* of Fig. 2.8 shows the ratio M_1/M_2 and the *y-axis* shows the ratio M_1/M_3. Comparing Fig. 2.8 with Fig. 2.6, it is clear that the magnetic polarizability values are concentrated within a smaller range than the electric polarizability values. Hence, the α_M values are more challenging to use as a shape classifier than the α_E values. Even so, some observations can be derived from Fig. 2.8. Magnetic polarizability components show an opposite trend to that of the electric polarizability components discussed in the previous section. Hence, disk-like oblate ellipsoids will have an M_1 value that is significantly larger than the M_2 and M_3 components [53]. Therefore, any object having a flat morphology, similar to that of a thin oblate ellipsoid, will have an M_1 value that is significantly larger than the M_2 and M_3. Consequently, the upper right corner of Fig. 2.8 will represent a disk-like shape. That is why we observed the largest values

41

of M_1/M_2 and M_1/M_3 for the SC and SC+OS stem cells, implying the same observation we drew from Fig. 6 that cells cultured on a 2D substrate are more likely to behave as a 2D disk under an external electrical field. Similar to the previous subsection, the observations achieved from Fig. 2.8 were obtained using a single shape from each family and a larger number of cells from each family will be simulated in the future to draw more accurate conclusions.
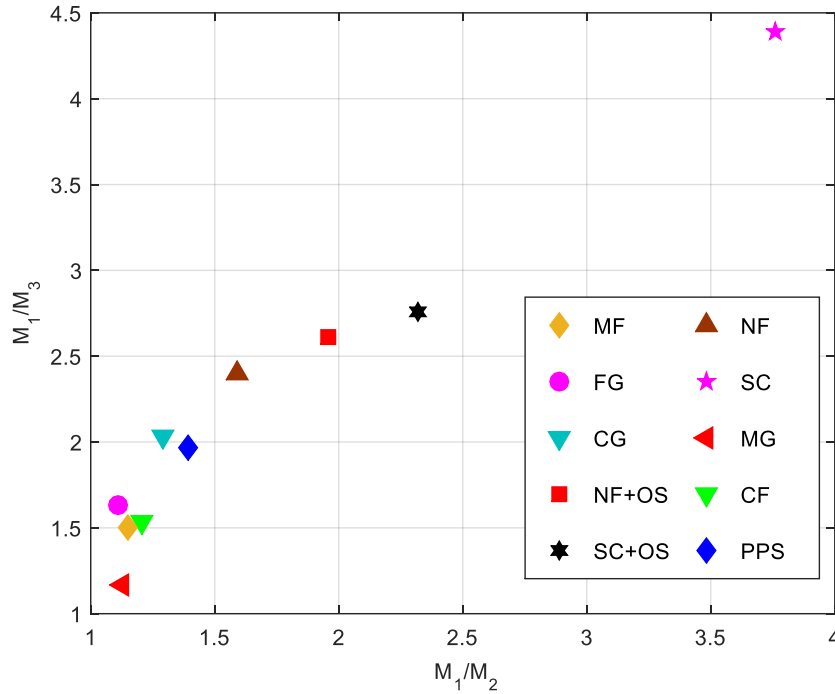
Figure 2.8 Encoding shape information from α_M

2.4.4 Intrinsic Viscosity

By using the hydrodynamic/electrostatic analogy, we can use the electric polarizability values to calculate the intrinsic viscosity of the stem cells. This will allow us also to quantify how the cell's morphology impacts the intrinsic viscosity η of the cell (see Table 2.4), a quantity that describes the presence of the cells at low concentration increases the viscosity of the fluid overall. Intrinsic viscosity is a measure of the contribution of the suspended particles

to the overall suspension viscosity. It is defined as $[\eta] = \lim\limits_{\phi \to 0} \frac{\eta - \eta_0}{\phi \eta_0}$, where $[\eta]$ is the intrinsic

viscosity of the suspended particles, ϕ is the volume fraction of the suspended particles, η_0 is

the viscosity of the solution in absence of the suspended particles, and η is the viscosity of the

suspension. We can calculate the intrinsic viscosity, using the analogy in Table 2.4, from the

polarizability results.

Fig. 2.9 shows the intrinsic viscosity of the 10 different stem cells. MG, FG and CG

are all obtained from hydrogel yet their $[\eta]$ values differ significantly. CG and FG have

significantly large $[\eta]$ compared to other cell morphologies because of their distributed

volume. The NF and the NF+OS cells were grown in a geometrically identical environment

but with different chemical composition since the soluble factor Osteogenic Supplements (OS)

was added only to the NF+OS cells. The comparison of the $[\eta]$ of the NF and the NF+OS cells,

and the $[\eta]$ of the SC and the SC+OS cells, indicates that modifying the chemical composition

of a cell's environment can affect its intrinsic viscosity $[\eta]$.

2.4.5   Intrinsic Conductivity [σ] for Variable Conductivity Contrast Δ

So far, we have only considered the calculation of the electric and magnetic

polarizability tensors α_E and α_M. The α_E values are calculated when the ratio between the

electrical conductivity of the cell and the electrical conductivity of its environment is equal to

infinity, whereas the α_M values are calculated when this ratio is equal to zero. Therefore, α_E

and α_M represent the two limiting cases for the electrostatic polarizability. In a practical
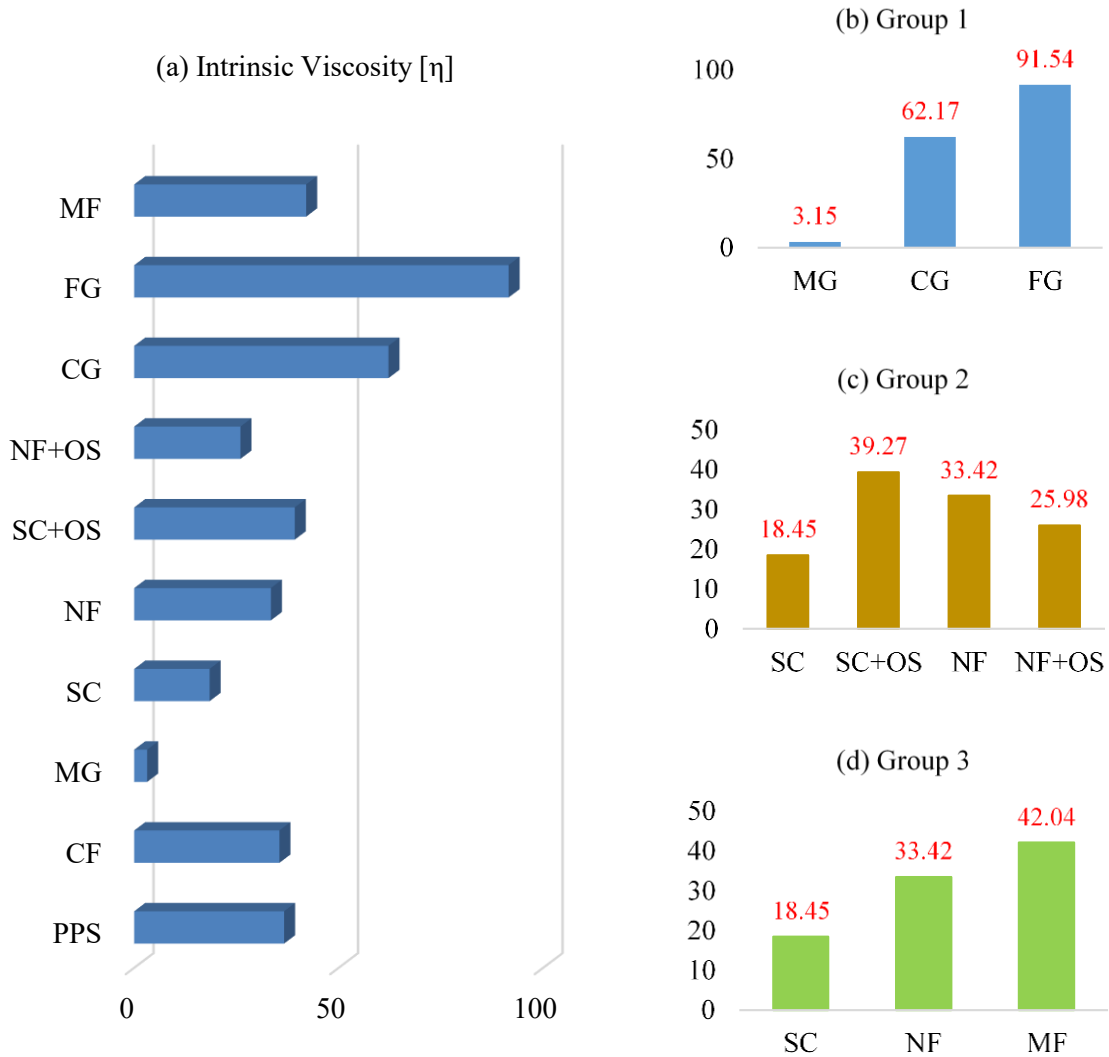
Figure 2.9 (a) Histogram plot of the intrinsic viscosity [η] of ten cell shapes. (b) Group 1 had the same building material (hydrogel) yet show a difference in [η], (c) Group 2 indicates addition of a soluble factor (OS) might increase the value of [η] in planar substrates (d) Group 3 is based on the 3 families made from same polymer [poly(ε-caprolactone), PCL]

scenario, the cell will have a finite contrast with respect to its environment. The ratio between the electrical conductivity of the cell and the electrical conductivity of its environment, Δ, will be finite and nonzero. Garboczi and Douglas introduced a Padé approximant formulation that we use to estimate the intrinsic conductivity of a particle, $[\sigma]_\Delta$, with an arbitrary shape at finite

contrast via the knowledge of only $[\sigma]_0$ and $[\sigma]_\infty$, where these quantities are defined as $[\sigma]_\infty = \frac{1}{3}tr(\alpha_E)$ and $[\sigma]_0 = \frac{1}{3}tr(\alpha_M)$ [49]. The intrinsic conductivity $[\sigma]_\Delta$ represents the average polarizability of the particle at multiple orientations when the particle has an arbitrary contrast Δ with respect to its environment. Similarly, $[\sigma]_0$ and $[\sigma]_\infty$ represent the average polarizability of the particle at multiple orientations for $\Delta = 0$ and $\Delta = \infty$, respectively. Equation (2.11) gives the Padé approximant as [49]:

$$[\sigma]_\Delta = \frac{[\sigma]_\infty(\Delta-1)^2 + a\ (\Delta-1)}{(\Delta-1)^2 + \left([\sigma]_\infty + \frac{a}{d}\right)(\Delta-1) + a} \qquad (2.11)$$

where d = spatial dimensionality of the particle. For our study, all particles are 3D (even the flattened cells). The parameter a is a shape dependent parameter defined as follows [49]:

$$a = \frac{[\sigma]_\infty - [\sigma]_0 + [\sigma]_\infty[\sigma]_0}{1 + (1 - \frac{1}{d})[\sigma]_0} \qquad (2.12)$$

The accuracy of the Padé approximant was demonstrated for a wide variety of shapes such as worm-like carbon nanotubes and crumpled graphene flakes [42]. In this work, our goal was to test the accuracy of the Padé approximant for shapes as complicated as the stem cell morphologies shown in Fig. 2.1. The Padé approximant can significantly reduce the computational time needed for numerical computation of $[\sigma]_\Delta$. Fig. 2.10(a) and Fig. 2.10(b) show the Padé approximant versus the intrinsic conductivity calculated using COMSOL for the PPS and FG stem cells, respectively, at "*down4*". As shown in Fig. 2.10, the good agreement between the Padé approximant and the COMSOL calculations for multiple contrast values, Δ, validate the approximation. Using COMSOL, the intrinsic conductivity at each Δ value required ~ 21 hours of run time whereas the Padé approximant required essentially no time at all, provided that $[\sigma]_0$ and $[\sigma]_\infty$ were calculated beforehand.

45
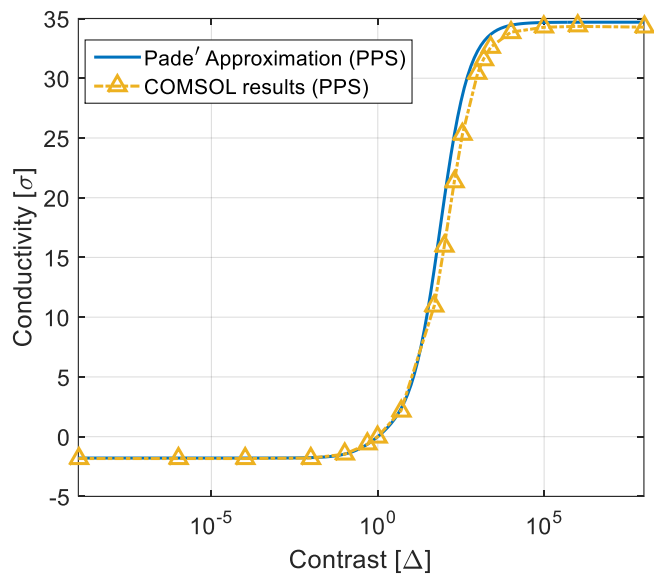
(a) PPS Cell
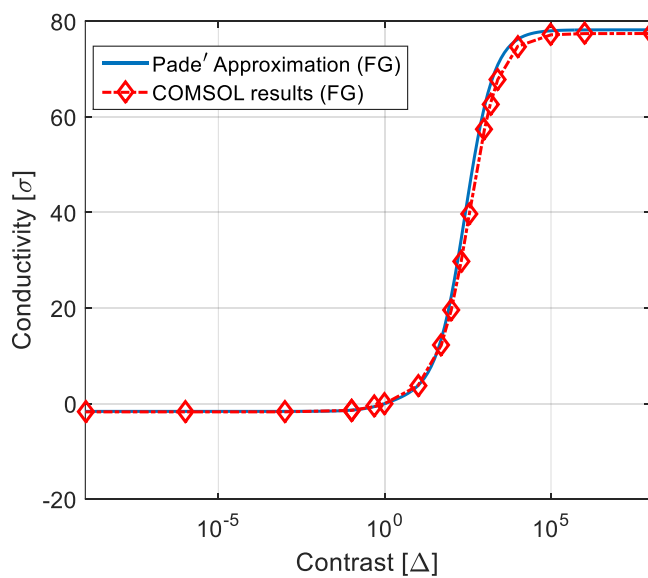
(b) Fibrin Gel (FG) Cell

Figure 2.10 Padé approximation for the intrinsic conductivity values for the case of two families (a) PPS and (b) FG

2.4.6 Minimum Enclosing Ellipse (MEE)

So far, all our previous results only considered 10 cell morphologies, one from each family. Our goal now is to explore the variations in the polarizability of cells with respect to different cells within each family. Therefore, we calculated the electric polarizability values, i.e. $\Delta = \infty$, of hundreds of shapes from each of the ten families to observe the variance in the calculated values. Since the Padé approximant only estimates the polarizability values at a finite contrast Δ and given that the three different solvers used in this work showed excellent agreement, only the Scuff-EM solver was used for all the cell shapes because of its' reduced computational time requirement. In each case, the "*down4*" representation of each cell was used. The "*down4*" representation is not the finest mesh but if we focus on the polarizability ratios, $\frac{P_1}{P_2}$ and $\frac{P_1}{P_3}$, similar values can be achieved as those achieved using the "*down1*" representation with the highest resolution as concluded from Fig. 2.5. This section summarizes the results of hundreds of stem cell polarizability ratios from the ten different families. One powerful tool to extract the useful observations from this large set of results is to enclose the polarizability ratios, $\frac{P_1}{P_2}$ and $\frac{P_1}{P_3}$, obtained from the hundreds of morphologies simulated from each family into a hyper-sphere (in this case a 2D ellipse) [56].

The dimension of the hyper-sphere will then contain the information about the variance of the data set. Khachiyan *et al.* first introduced the algorithm as an optimization problem to find the ellipsoid with the smallest volume that encloses all the given data points in an n-dimensional space in [56]. The general form of an ellipsoid in center form can be written as (2.13) [57]:

$$\mathcal{E} = \{x \in \mathbb{R}^n \mid (x-c)^T A(x-c) = 1\} \tag{2.13}$$

47

where x are the data points, c is center of the ellipsoid in n dimensional space and A is an $n \times$ n matrix containing the information about dimension and orientation of the ellipsoid. The volume of the ellipsoid in this form is given by (2.14) [57]:

$$Vol(\mathcal{E}) = \frac{v_o}{\sqrt{\det(A)}} = v_0 \det(A^{-1})^{\frac{1}{2}} \tag{2.14}$$

where v_0 is the volume of the unit hypersphere in dimension n. Now, to enclose a set of m data points in n dimensional space $S = \{f_1, f_2, f_3, \dots f_m\} \in \mathbb{R}^n$, we must impose the constraints that all the m points f_i are inside the boundary of the ellipsoid [57]i.e.

$$(f_i - c)^T A(f_i - c) \le 1 \qquad i = 1,2 \dots m \tag{2.15}$$

So, the optimization problem can be formulated as (2.16)

$$minimize \quad \det(A^{-1})$$

$$subject\ to \quad (f_i - c)^T A(f_i - c) \le 1 \qquad i = 1,2 \dots m \tag{2.16}$$

Calculating the *singular value decomposition (SVD)* of matrix A will provide us the information about the length of the semi-axes and orientation of the principal axes of the enclosing ellipse [57]. Adopting the numerical implementation of the above-mentioned algorithm, we simulated all cell morphologies in the NIST database. The electric polarizability ratios from each of the ten families are then clustered as a minimum area ellipse as shown in Fig. 2.11. The successful implementation of MEE is demonstrated for the case of one cell family (e.g. Microfibers (MF)) in Fig. 2.11. We opted for calculating the MEE that encloses all the polarizability values even the outliers as shown in Fig. 2.11. We could have focused on obtaining a smaller MEE by enclosing a smaller percentage of the cells (~ 80% for example)

that show similar polarizability values. But we opted for calculating the MEE as indication of the maximum variability in the polarizability values that can be obtained in each family.
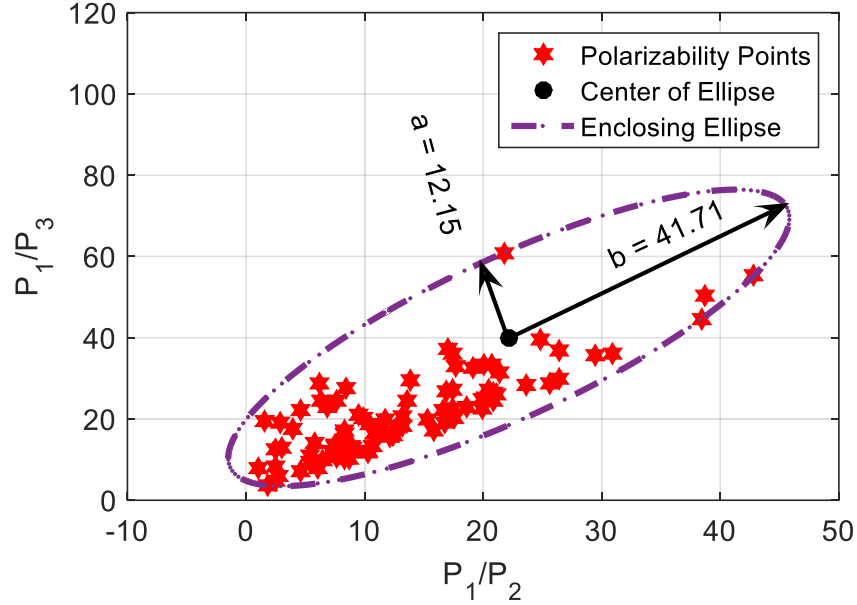
Figure 2.11 Implementation of Minimum Enclosing Ellipse (MEE) to represent MF family

We computed the enclosing ellipse for all the ten cell families in similar fashion. Table VIII summarizes the number of cells simulated from each family as well as the properties of the MEE such as the semi-minor axis (a), the semi-major axis (b), the area of the MEE, and the tilt angle the MEE makes with the *x-axis*. Since $P_1 \geq P_2 \geq P_3$, the minimum tilt angle is 45° which occurs when occurs when $P_2 = P_3$. Large tilt angles indicate that the ratio between P_1/P_3 and P_1/P_2 is large (i.e. $\frac{P_1}{P_3} \gg \frac{P_1}{P_2}$), indicating that P_2 is significantly larger than P_3. Therefore, large tilt angles indicate shapes which have two dimensions larger than the third, i.e., oblate in nature, whereas small tilt angles indicate shapes that have one dimension larger than the other two, i.e. prolate in nature.

To make the observation visually less complicated, we divided the MEE of the 10 cell families into three different subplots in Fig. 2.12. The subplots were categorized according to the scaffold material and characteristics of the cell families. MF, NF, and NF+OS are grouped in one subplot, Fig. 2.12(a), since they all were made from the same PCL polymer. Fig. 2.12(b) incorporates the three cell families that were grown on 2D planar scaffolds CF, SC, and SC+OS. The remaining scaffolds CG, FG, and MG are 3D scaffolds, and their MEE polarizability results are grouped together in Fig. 2.12(c).

From the cell clustering, we can deduce some significant understanding about the electrical behavior of the ten different cell families. The MEE for the MF family has the smallest area of the three cell families in Fig. 2.12(a), indicating less variations in the cell's polarizability values than the NF and the NF+OS families. For the MF family, the cells were grown on a scaffold composed of microfibers whereas for the NF family the cells were grown on a scaffold composed of nanofibers. Therefore, the main conclusion from Fig. 2.12(a) is that the larger features sizes of the MF scaffold reduce the possible shape variations similar to the case of a pixelated screen where coarser resolutions lead to fewer pixels per unit area and a smaller number of possible shape variations.

The results in Fig. 2.12(a) and Fig. 2.12(b) show that adding a soluble factor (i.e. Osteogenic Supplement) to create the SC+OS and NF+OS scaffolds, generate cells with polarizability values that cover the same range of values as the SC and NF cells. The same conclusion can be achieved from Table 2.8 which shows that the MEE area and tilt angle of the SC family and the SC+OS are very similar. Similar observations can be achieved by comparing the NF and the NF+OS values in Table 2.8.

50
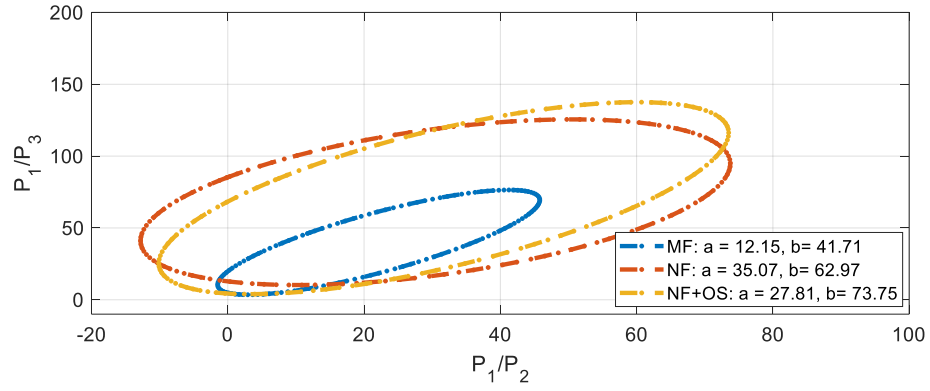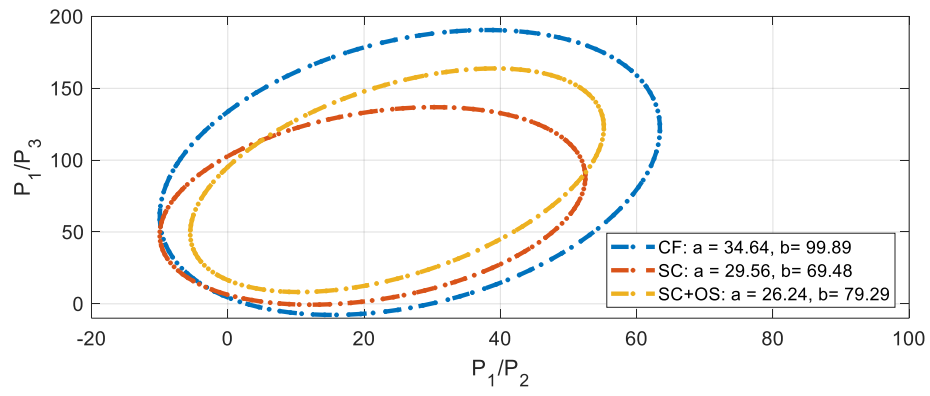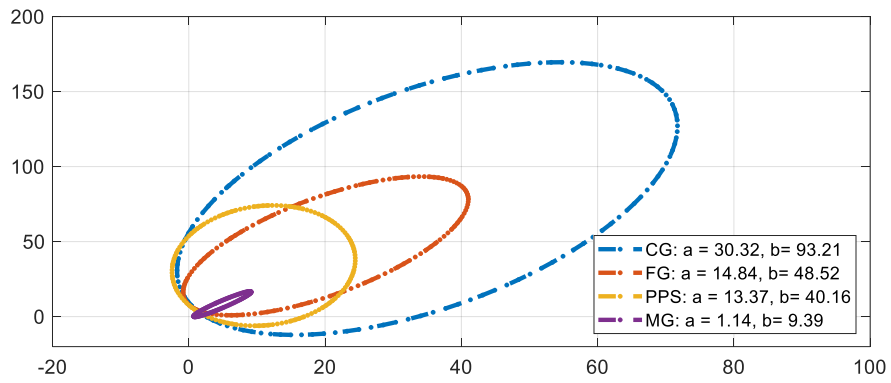
Figure 2.12 Cluster presentation of (a) NF, MF, NF+OS; (b) CF, SC, SC+OS and (c) CG, FG, PPS, MG using Minimum Enclosing Ellipse (MEE)

Table 2.8 The semi-axes of the Minimum Enclosing Ellipse (MEE) algorithm for all ten cell families

Family	Number of Cells	a	b	Area	Tilt Angle (°)
MF	87	12.2	41.7	1592.09	59.47
NF	101	35.1	63	6937.76	61.02
NF+OS	95	27.8	73.8	6443.37	62.79
CF	102	34.6	99.9	10870.5	82.56
SC	99	29.6	69.5	6452.29	80.78
SC+OS	96	26.2	79.3	6536.3	78.24
CG	101	30.3	93.2	8878.54	76.41
FG	92	14.8	48.5	2262.06	71.37
PPS	98	13.4	40.2	1686.84	87.84
MG	98	1.14	9.39	33.63	64.17

The cell family showing the most variations, that is the MEE with the largest area, is the CF family. The scaffold used for this family is 2D in nature and Fig. 2.12(b) shows that 2D scaffolds (SC, SC+OS, and CF) typically lead to more variations in the polarizability values of cells than most 3D scaffolds. The SC, SC+OS, and CF families also show higher tilt angles than most other families. This can be seen by comparing the orientations of the MEEs in Fig. 2.12(a) and Fig. 2.12(b) and also by looking at the tilt angle entries in Table 2.8. Therefore, the SC, SC+OS, and CF families lead to cells which are more oblate in shape than the other families.

The remaining 3D families in Fig. 2.12(c) show that the CG family has the largest variations followed by the FG, then the PPS family, and the MG gamily shows the least

variations. This can be observed by comparing the areas of the ellipses in Fig. 2.12(c) and the entries in Table VIII. The MG scaffold generate cells which are almost spherical in shape with minimal variations and therefore their polarizability values are clustered over the smallest areas.

A final comment on the Fig. 2.12 and Table 2.8 is that these results were obtained from a finite number of cells. Larger cell distributions are needed to draw firm conclusions about the cell populations grown under different conditions. However, the current paper focuses on the methodology of calculating the polarizability values for complex shaped cells and how to visualize their variations in a clear and informative manner.

2.5   Discussion

The numerical experiments performed in this work validate the calculated polarizability values and shed light on the advantages and disadvantages of different numerical techniques and meshing resolution. However, more importantly, calculating the polarizability tensors at any contrast between the cell and its environment paves the way to many applications such as predicting the hydrodynamic, dielectrophoresis, and electroporation response of stem cells. For example, by invoking the well-established theory of the hydrodynamic-electrostatic analogy [32], we can predict the variations in the hydrodynamic properties of stem cells grown in different environments. Dielectrophoresis (DEP), defined as the force exerted on a cell due to a specific electrical excitation, is directly proportional to the elements of the generalized polarizability tensor [53]. This force, $\overrightarrow{F_{DEP}}$, acting on a cell can be quantified as (2.17) [58]

$$\overrightarrow{F_{DEP}} = \frac{1}{2}\alpha V(\nabla E^2) \tag{2.17}$$

where, α is the volume normalized polarizability of the particle, V is the volume of the cell.

Therefore, the DEP force has a strong dependency on the polarizability of the cell or particle in general [59]. The DEP force has been frequently employed in the separation of particles with different shapes and properties. This is because, particles with different shapes will have different polarizability values, α, leading to different forces that can be leveraged in separating a heterogeneous mixture of particles. Frederick *et al.* successfully employed this phenomena to isolate cancer cell line MDA231 from *erythrocyte* and *T lymphocyte* blood cells in an *in vitro* condition [59]. They observed that, cancer cell lines experience a different DEP force than the normal cells when subjected to a rotating electric field due to their variation in morphology, microvilli inclusion and membrane folds. Regtmeier *et al.* experimentally evaluated the differences in polarizability between two DNA fragments of different shapes: *(i)* linear and (*ii*) supercoiled. Based on this differences in polarizability, the DNA fragments with different shapes experienced different $\overrightarrow{F_{DEP}}$ behavior which was successfully leveraged for their separation [60]. The main goal of this work is to explore different computational techniques to calculate the polarizabilities of realistic and complex cell shapes grown in different environments. Accurate calculation of these polarizability values can help in predicting the $\overrightarrow{F_{DEP}}$, experienced experimentally by cells, guiding cell separation experiments similar to those reported in [61]–[64].

The induced transmembrane voltage (ITV) on the cell membrane under the excitation of an external electric field is also a direct function of the polarizability of the cell and its electric properties [65]. The ITV plays a significant role in the formation of aqueous pores, termed electroporation, which emerge at the cell membrane locations where the ITV exceeds a certain threshold [66]. This enables the introduction of therapeutic drugs into the cell, which are not easily passed through the membrane in natural conditions [66]. Therefore, an accurate

calculation of the polarizability of a stem cell will shed light on the effectiveness of the electroporation process due to a specific electric stimulus.

On a different note, there is significant interest in the overall electrical properties of tissues made of a composite of cells and other structures. By invoking the Effective Medium Approximation, the effective electrical properties of these tissue can be expressed as a function of the polarizability of the constituting cell types [67]. Therefore, the calculation of the polarizability of cells of different shapes can be used to predict the effective electric properties of tissues [67].

2.6   Conclusion

In this paper, the electric properties of a large number of stem cells with realistic three-dimensional (3D) morphologies are calculated. The stem cell morphologies were obtained from a database recently introduced by the National Institute of Standards and Technology. The electric properties that we focused on were the electrostatic electric polarizability, the magnetic polarizability, and the polarizability at an arbitrary contrast. Multiple computational techniques and multiple resolutions were tested for each cell for cross-validation and to show the effect of shape resolution on the electrical polarizabilities. This work shows that the environment of the stem cells can have a significant effect on the shape leading to polarizability values that are significantly different from each other and from a simple sphere. Furthermore, we introduced different techniques to visualize the variations in the polarizability values with respect to the shape of different cells from within one family and with respect to cells from different families. Finally, a Padé approximant was shown to accurately estimate the polarizability of a stem cell at arbitrary electrical conductivity contrast using only the electric and magnetic polarizabilities. We believe that these results can be used as a benchmark for the

polarizability calculation of 3D biological and non-biological particles with complex 3D shapes. Moreover, in many previously reported studies, the shape of stem cells were assumed to be approximately spherical when designing experiments for their electric characterization and during the interpretation of the measured results. The polarizability values in this work will aid in designing more accurate experiments and a more accurate interpretation of the measurement results, which has the potential to advance the electrical characterization of biological cells.

CHAPTER 3

3 INDUCED TRANSMEMBRANE VOLTAGE IN REALISTIC THREE-DIMENSIONAL MORPHOLOGIES OF STEM CELLS

3.1 Abstract

The induced transmembrane voltage (ITV) generated across a cell's membrane plays a significant role in the process of electroporation since the membrane permeability increases when the ITV exceeds a certain threshold. The objective of this study is to use Finite Element simulations to investigate the ITV profile for cells with realistic three-dimensional (3D) morphologies. A wide range of realistic 3D morphologies is obtained from a database of stem cell morphologies developed by the National Institute of Standards and Technology. By setting arbitrary ITV electroporation thresholds, we calculated the electroporated area for each stem cell morphology at different orientations and showed significant difference in comparison to spherical cells of similar size. The significance of morphological variation is more prominent for dynamic frequency-dependent excitation. Using numerical experiments, we show that as the frequency of the excitation increases, the ITV decreases beyond a certain cutoff frequency that varies with cell morphology. An approximate relation exists between this cutoff frequency and the self-capacitance of the cells. Our findings solidify our hypothesis that morphology plays a substantial role in the electrical response of biological cells and therefore must be taken into consideration when interpreting measurements.

3.2 Introduction

Cell membrane preserves the cellular integrity by creating a barrier between the extracellular and intracellular media [68]. All biological cell membranes are composed of a lipid bilayer, with embedded ion pumps and transporters [68]. The ion pumps/ transporters

help to maintain the ionic imbalance between the cell's interior and exterior by allowing the passage of specific ions to and from the cellular compartments [69]. Due to the ionic imbalance, there exists a potential difference in steady state, ranging from 20 mV to 70 mV, negative inside the cell with respect to the extracellular matrix [70]–[72]. This built-in potential plays a major role in many molecular activities and facilitates signal transmission in excitable cells (i.e. neuron, muscle cells). Electrically, the cell membrane represents an insulating barrier to the ionic current flow through the cell [66]. An external electrical excitation generates a voltage across the cell membrane termed the induced transmembrane voltage (ITV) [5]. When the induced voltage superimposed on the exiting membrane potential exceeds a certain threshold, the energy required for stable pore formation on the membrane surface reduces and the lifetime of these pores increase by several orders, ranging from milliseconds to minutes [73], [74]. The creation of pores allows ions and proteins to enter the cell, that are otherwise impermeable through the membrane. This phenomenon is typically referred as electropermeabilization or electroporation [66], [75].

The electroporation process is reversible if the duration of the excitation pulse is small, commonly known as reversible electroporation and has gained huge interest in electro-chemotherapy and gene therapy during the last few decades [76]–[79]. If the cell is exposed to the high electric pulse for long enough period, the result is cell death. This phenomenon is known as IRreversible Electroporation (IRE) and it is currently investigated as a promising tool for cancer treatment [79]–[84]. Reversible electroporation provides control over targeting a specific region of a cell or tissue for chemotherapeutic drug or DNA delivery [85]. Irreversible electroporation is simpler but it impedes the efficiency by resulting in detrimental thermal effect [85].

Depending on the area of interest, the electroporation study can be subdivided into two major categories: bulk electroporation and single cell electroporation [75]. Single cell electroporation studies are more suitable for observing the effect of cell shape, size and orientation of the excitation field [5], [75]. Moreover, the technical understanding from a single cell electroporation study can be easily transferred to cell assemblies and tissues if the modification of local electric field distributions due to the presence of neighboring cells is taken into consideration [5], [86].

The goal of this study is to investigate the effect of variation in cell morphology on the ITV profile to guide electroporation studies. To isolate the effect of cell morphology, we are focusing on single cell ITV simulations. Several studies have already investigated the ITV using a wide variety of experimental and computational techniques [87]–[89]. However, most of these reported studies only considered simple cell morphologies such as spheroidal cell shapes (i.e. spheres and ellipsoids) [65], [87]. Few studies considered morphologies reconstructed from experimental measurements of the cell shape. A similar study done by Pucihar *et al.* 2006, presented numerical simulation of irregularly shaped cells [88], [89]. The study proposed a finite element solution of ITV on an irregularly shaped CHO cell cultured on a 2D substrate. As 2D culturing microenvironment was used, the cultured cell families failed to account for the effect of *in-vivo* environment on the cells' 3D morphology [88], [89]. The major conclusion drawn from that study is that each cross section of the CHO cell is analytically equivalent to the ITV calculation of a hemi-ellipse of the same shape [88]. Linear cell membrane dynamics were incorporated using numerical implication of surface conductivity and permittivity without going through the tedious process of physically implementing uniform membrane thickness for arbitrary shapes. Some recent studies also

incorporated the similar methodology to calculate the ITV distribution across *E. Coli* and Red Blood Cell (RBC) layers under different excitation protocol [90], [91]. Gowrishankar and Weaver performed the ITV calculation of multiple cells in a tissue using an equivalent impedance model (transport model) to characterize the cell interior, exterior and the cell membrane [92]. The major finding of these studies is the demonstration of a useful, accurate and convenient approach to get insight of the behavior of a cell under external electrical excitation which is rather difficult to obtain experimentally. However, the major drawback of these studies is their incapability to incorporate the exact 3D morphology of cells under investigation, due to the lack of appropriate imaging and segmentation algorithms [88], [89], [93].

Therefore, the goal of this work is to bridge this knowledge gap by incorporating the most advanced open source 3D cell database developed by National Institute of Standards and Technology (NIST) to date. This database was created by culturing the Human Bone Marrow Stromal Cells (hBMSCs) lineage in ten different microenvironments to show how the environment affects cell morphology [94]. The cells were categorized into ten cell families according to their culturing microenvironment, each cell family containing 3D map of approximately 100 cells, available in both volumetric mesh format (*voxels*) and surface mesh (*.obj*) via [94]. We studied the electroporation scenario for one cell from each of the ten families, therefore incorporating a wide variability of realistic and most accurate representation of 3D cell shapes.

This paper is arranged as follows: In Section 3.3, we briefly describe the NIST stem cell database and how the morphologies in the database can be adapted for ITV Finite Element Simulations. In Section 3.4, we present the electroporation results for both the steady state and

frequency dependent simulations. In Section 3.5, we present the Conclusions and discussion potential ideas for future expansion of our current study.

3.3   Methodology

In the NIST stem cell database, five different resolutions were provided for each cell morphology: "*down1*", "*down2*", "*down4*", "*down8*", and "*down16*". The "*down1*" resolution was the highest and, therefore, is the closest approximation to the original cell morphology whereas "*down16*" is the coarsest resolution. In our previous study, we showed that the ratios of the diagonalized electrostatic polarizability values are insensitive to the resolution of the cell morphology [95]. Therefore, we used the "*down4*" resolution for all ten cells to reduce the computational cost without losing significant morphological features. We incorporated the same cells from Table 2.1 for the preliminary study. The 3D morphologies of all the ten cell shapes categorized according to their culturing microenvironment along with their volume are presented in Fig. 3.1. As discussed previously in section 2.3, the 10 selected cells demonstrate a wide range of variations in regard of morphological feature. For recap, the MG cell demonstrates an equiaxial morphology, the NF cell shape resembles a 1D rod, and the SC cell exhibits a 2D disk like shape.

Polymer (PCL) substrate	Hydrogel Material	Collagen processed into either 3D gel or 2D	Additional soluble factor OS (Osteogenic Supplement)	Alvetex, pore size: 36 μm
Spuncoat (SC) 31755 μm^3	Matrigel (MG) 15906 μm^3			
Nanofiber (NF) 12421 μm^3	Fibrin Gel (FG) 15133 μm^3	Collagen Fibrils (CF); 15133 μm^3	(NF+OS) 24754 μm^3	
Microfiber (MF) 27892 μm^3		Collagen Gel(CG) 36359 μm^3	(SC+OS) 20959 μm^3	Porous Polystyrene Scaffold(PPS) 23885 μm^3

Figure 3.1 3D Volumetric Mesh of all ten cell shapes from ten different scaffolds

3.3.1 Numerical Simulation Setup

The ITV of a few canonical shapes can be expressed using a closed form formula. Fricke first developed the closed form expression of induced transmembrane voltage for a cell of general ellipsoidal morphology under steady state DC excitation in 1953 [96]. Over the past few decades, there has been several attempts to modify this close form solution of ITV to account for arbitrarily oriented regular cell shapes like ellipsoids, sphere and cylinders [97]–[101]. All these expressions were obtained based on the assumption of zero membrane conductance and uniform field excitation. For a spheroidal cell where $b = c$, the ITV on a simple spheroidal cell for uniform field excitation can be expressed as (3.1) [65]:

$$\Delta\phi = E \frac{1}{\sqrt{\frac{cos^2\theta}{a^2} + \frac{sin^2\theta}{b^2}}} \begin{pmatrix} sin\alpha \, cos\beta \\ sin\alpha \, sin\beta \\ cos\alpha \end{pmatrix} \begin{pmatrix} \frac{1}{1-L_x} sin\theta \, cos\varphi \\ \frac{1}{1-L_y} sin\theta \, sin\varphi \\ \frac{1}{1-L_z} cos\theta \end{pmatrix} \qquad (3.1)$$

Here, a and b are the length of major semi axes of the ellipsoidal cell, α and β denotes the orientation of the E field in spherical coordinate system; θ and φ are used to express the coordinate of the point of interest on the membrane; L_x, L_y and L_z are depolarization factor of the ellipsoid in x, y and z directions respectively and follows the relation $L_x = L_y = \frac{1}{2}(1 - L_z)$ (Fig. 3.2).
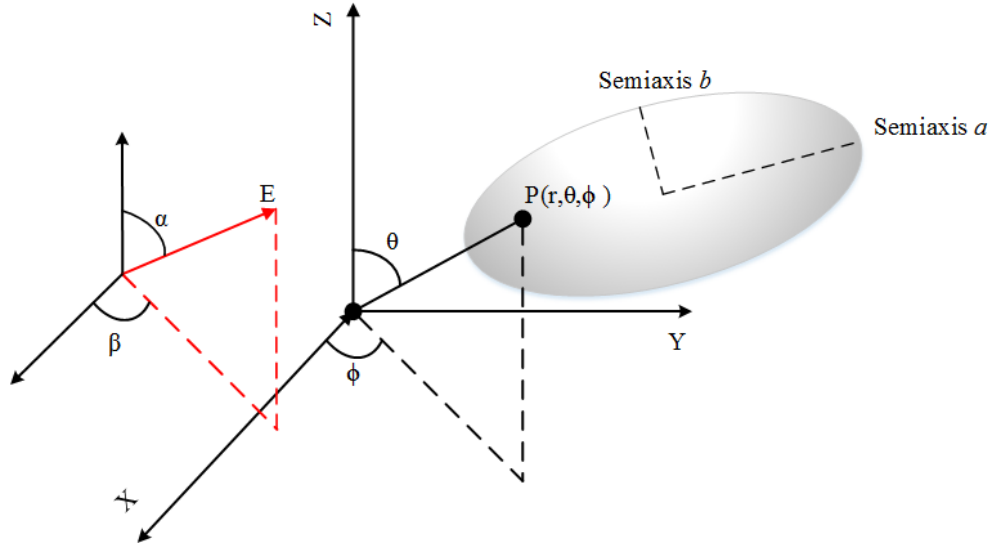
Figure 3.2 Depiction of an arbitrarily oriented ellipsoidal cell under a uniform electric field E

However, closed form expression of the ITV for realistic cell shapes with nonuniform geometry is not possible to obtain since the circumference of the object cannot be expressed as a mathematical entity. In such cases, the ITV can be obtained by solving the time dependent Laplace equation by using finite element or finite time difference method (3.2) [66]:

$$\nabla \left[\left(\sigma + \varepsilon \frac{\partial}{\partial t} \right) \nabla\phi(x, y, z, t) \right] = 0 \qquad (3.2)$$

In our study, we are going to incorporate the methodology developed by Pucihar, *et al.* 2006 for the ITV calculation of the cell shapes introduced above, to observe the effect of variation in realistic cell shapes on ITV [88]. The available mesh format that is appropriate for our study is *.obj* (wavefront) format [28]. We used Meshlab to recenter the geometry of the cell at origin and converted it to *.stl* (stereolithography) that is compatible to be imported in COMSOL® Multiphysics[5], the finite element solver that will be used in this study [43], [45]. For our single cell electroporation study, we performed ITV calculation using the Electrical Current Package of COMSOL® under both stationary and frequency dependent conditions. For our study design, a uniform incident electric field excitation of 100 V/cm is used for all analysis.

The cell membrane thickness is almost a thousand times thinner than the cells' average diameter which makes it computationally expensive to model the membrane explicitly without using an extremely large number of mesh elements [44]. Therefore, the cell membrane is modeled implicitly by defining a contact impedance at the outer boundary of the cell in COMSOL, which leads to close agreement to the case where the membrane is explicitly modeled [88]. The set of equations incorporated for the contact impedance case is as follows (3.3) [44]

$$n.J_1 = \frac{\sigma + j\omega\varepsilon_0\varepsilon_r}{d_s}\,(V_1 - V_2) \tag{3.3a}$$

---

[5] Certain commercial equipment and/or materials are identified in this report in order to adequately specify the experimental procedure. In no case does such identification imply recommendation or endorsement by the National Institute of Standards and Technology, nor does it imply that the equipment and/or materials used are necessarily the best available for the purpose

$$n.J_2 = \frac{\sigma + j\omega\varepsilon_0\varepsilon_r}{d_s}(V_2 - V_1) \qquad (3.3b)$$

Here, J_1 and J_2 are the surface current densities at the outer and inner surface of the membrane, d_s and σ are the thickness and surface conductivity representing the cell membrane, V_1 and V_2 corresponds to the voltage on both side of a point on the cell membrane. Computationally, the difference between V_1 and V_2 will correspond to the ITV at a specific point on the cell membrane.

The simulation setup for the steady-state (DC) and frequency dependent (AC) ITV calculation is depicted in Fig. 3. The parameters and material properties used for both DC and AC studies are enlisted in Table 3.1.

Table 3.1 Material properties for different domain incorporated in the FEM model

Medium	Electrical Conductivity (S/m)	Relative Permittivity
Extracellular Matrix	1.2	72.3
Intracellular Matrix	0.3	72.3
Cell Membrane	5×10^{-7}	5
Membrane Thickness		5 nm
Electrical Excitation		100 V/cm
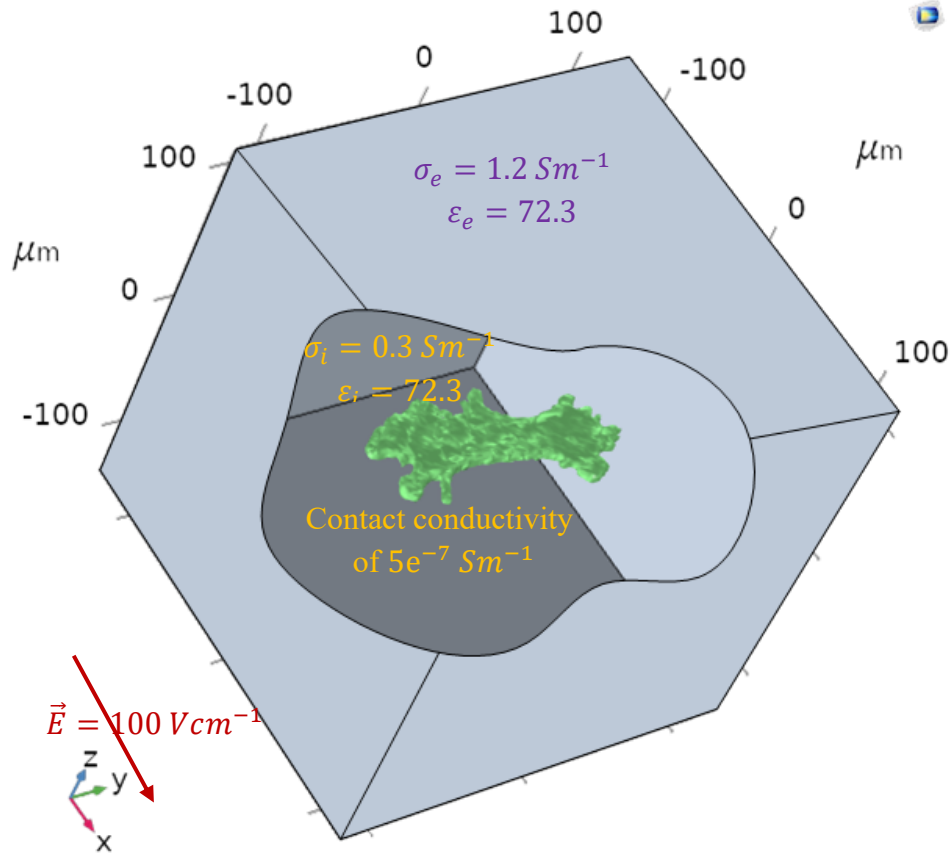
Figure 3.3 Depiction of the FEM solution setup for both steady state and frequency dependent study

The simulation steps involve importing the cell shape of interest into a bounding box of 100 V/cm electrical excitation and extracellular material properties. The intracellular matrix properties (i.e. electrical conductivity (σ_i)and relative permittivity (ε_i)) were assigned to the cell interior. Cell membrane properties were incorporated using the "*contact impedance*" feature as described previously. Then the desired study was performed under uniform excitation.

In frequency dependent study, to establish the relation between crossover frequency and shape parameter, we incorporate the concept of self-capacitance. Besides being an electrical

quantity, capacitance can also be used as a shape measure to quantify shape dependence of any object under electrical excitation [29]. For spherical cell shapes, the self-capacitance follows a closed form formula given by (3.4):

$$C_{self} = 4\pi\varepsilon r \qquad (3.4)$$

Where, ε is the permittivity of the medium and r is the radius of the sphere. The calculation of self capacitance for the complicated geometries as considered in this study requires numerical solution of the Laplace equation (3.2) in a similar fashion. For evaluate the shape dependent self-capacitance parameter, we have employed the static subroutine of Scuff-EM, an open source method of moment (MoM) package for solution of static and dynamic electromagnetic scattering problems [46].

3.4   Result and Discussion

3.4.1   Validation

The accuracy of the implementation of our model is depicted in Fig. 3.4. Fig. 3.4(a) illustrates the steady state excitation and the frequency dependent excitation case is represented in Fig. 3.4(b). In both cases, we have considered a 100 V/cm excitation electric field with radius $r = 15\ \mu m$ for spherical cell. In steady state excitation, the ITV profile along the cross-section at $z = 0\ \mu m$ was taken and plotted against the arc angle parameter. For frequency dependent excitation, ITV at pole, a point of the cell surface where the excitation field is longitudinal was considered. Our observation from the comparison depicted in Fig. 3.4 establishes the validity of our model implantation.
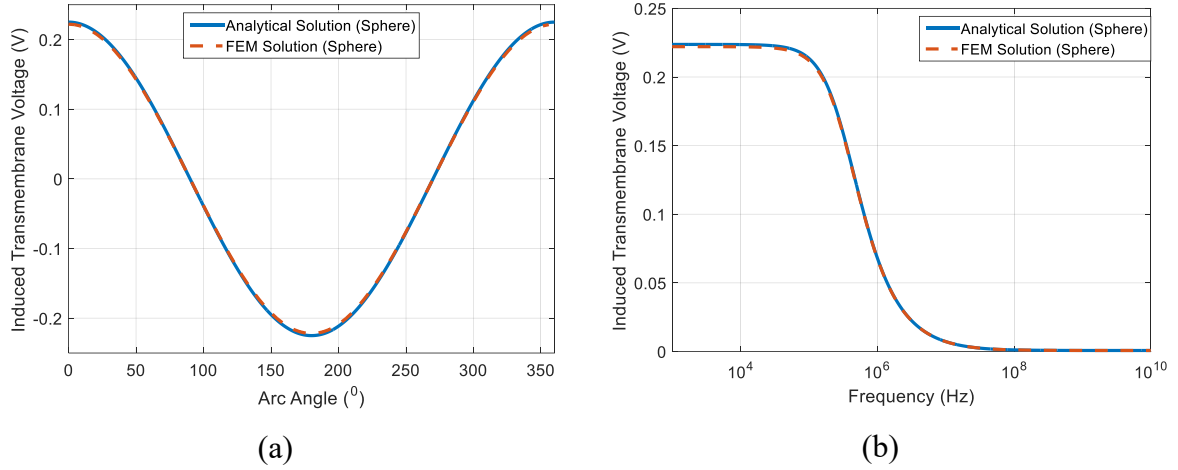
Figure 3.4 Proposed Finite Element Model (FEM) validation in case of (a) steady-state and (b) frequency varying excitation

3.4.2　　Steady State Excitation

To investigate the effect of cell orientation on cell electroporation area (i.e. area of the cell experiencing ITV$\geq \phi_c$), we applied the steady state excitation on two spheroids with same volume and aspect ratio. Valič et. al demonstrated the effect of cell orientation with experimental validation in their study [65]. They observed that, the maximum transmembrane voltage induced increases for an oblate ellipsoid whereas it decreases in case of a prolate ellipsoid as the principle axis of the cell is rotated such that it becomes horizontal to vertical with the direction of the excitation field [65]. However, as the aspect ratio of the spheroids tends to one, the transmembrane dependence on the rotation of the cell becomes negligible as the cells become more spherical in shape [65]. Similar behavior is demonstrated in Fig. 3.5 where we can observe the variation in electroporated area due to variation in the angle of rotation. Both the oblate and prolate ellipsoid with same volume and aspect ratio (7:1) were placed under a steady state 100 V/cm electrical excitation with their major axis aligned parallel to the direction of the excitation field (i.e. $\alpha = 0^0$). As the ellipsoids were rotated so that the excitation field becomes perpendicular to the major axis (i.e. $\alpha = 90^0$), the electroporated area

68

of the oblate ellipsoid (Fig. 3.5(b) & 3.5(c)) increases while the threshold for electroporation (ϕ_c) is low. However, as the electroporation threshold is increased, the percentage electroporated area starts decreasing similar to the case of prolate ellipsoid (Fig 3.5(a)). This behavior of oblate ellipsoid is independent of the excitation strength as can be seen by comparing Fig. 3.5(b) and Fig. 3.5(c). Fig. 3.5(b) depicts the scenario when $E = 100$ V/cm and Fig. 3.5(c) encloses the oblate ellipsoid behavior when $E = 200$ V/cm. The reason behind the difference in electrical behavior of these ellipsoids are evident from Fig. 3.5(d). As can be observed from the figure, the maximum ITV decays more rapidly with rotation angle in case of prolate ellipsoid in comparison to oblate ellipsoid, making the later having a slow response to the rotational axis change. That is why the electroporated area for oblate ellipsoid seems to increase with angle of rotation when the threshold is low.

(a)

(b)

(c)

70
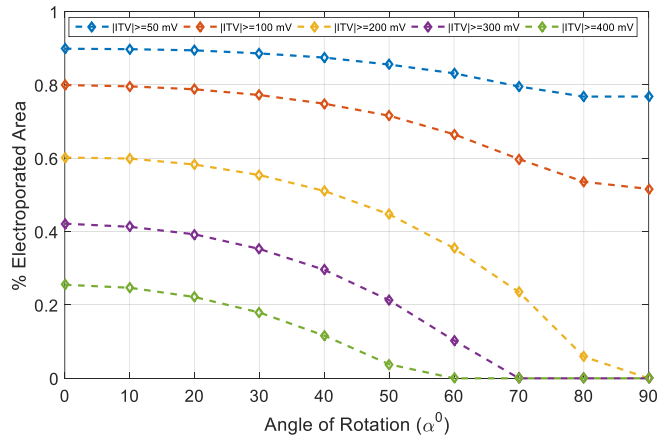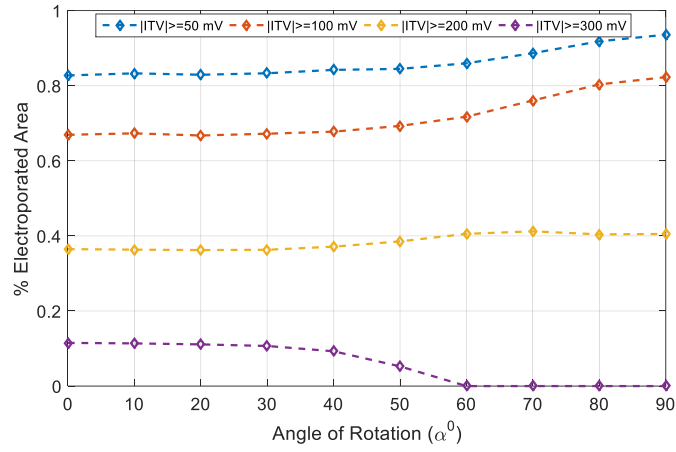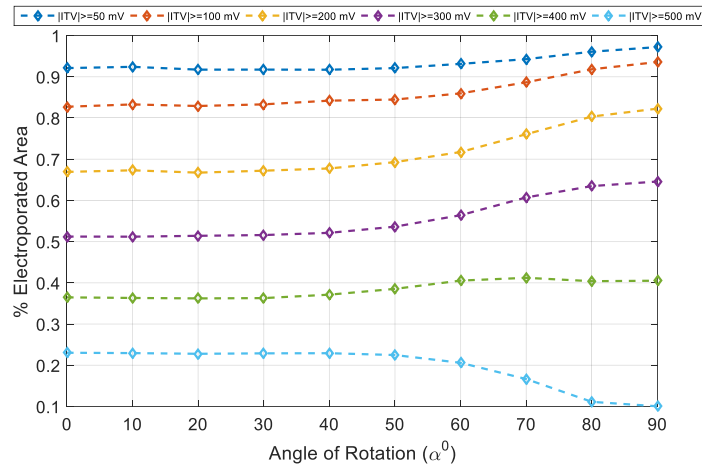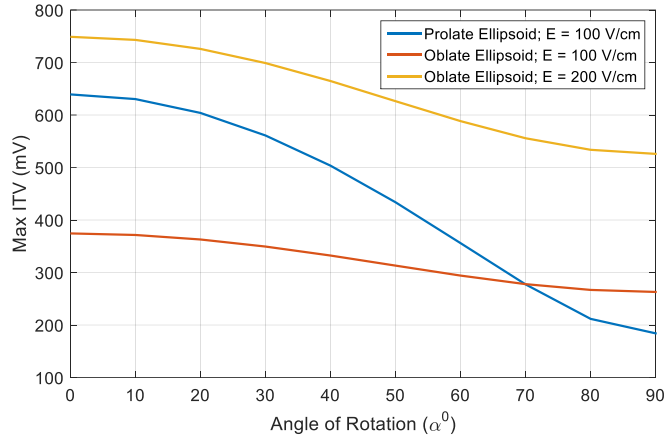
(d)

Figure 3.5 Comparison between percentage electroporated area variation with angle of rotation for (a) a prolate and (b) an oblate ellipsoid of same volume and aspect ratio under 100 V/cm electrical excitation; (c) oblate ellipsoid excitation 200 V/cm, and (d) The maximum ITV profile for the prolate ellipsoid

We tried to observe the behavior of the stem cell geometries mentioned in our study in a similar manner to conclude upon their shape classification. In order to align the cells with major axis parallel to the direction of excitation field, we diagonalized the cells according to their electric polarizability [95]. After diagonalization, we performed a parametric study on rotation along the minor axis (smallest dimension of the cells), which is depicted in Fig. 3.6. Although, the SC cells are electrically supposed to behave like a oblate ellipsoid or 2D disk as summarized from [95], the percentage electroporated area vs. angle of rotation plot shows that, the SC cell considered in this study is actually behaving like a prolate ellipsoid when the induced transmembrane voltage study is of concern. In fact, all the other cells which has huge variation in their electrical behavior according to their polarizability as concluded from [95], all of them demonstrates similar behavior as the prolate ellipsoid (i.e. the electroporated area always decreases with the variation of angle of rotation). Since, in our case, the cell geometries are not symmetric, we performed the parametric study from $\alpha = 0^0$ to $\alpha = 180^0$. However,

electroporated area of the NF cell as depicted in Fig. 3.6(c) drops more rapidly with rotation angle (α) as compared to the SC (Fig. 3.6(a)) or PPS (Fig. 3.6(b)). That is because, the NF cells were grown in a 3D substrate with very small pore radius, resulting the cells to be distributed only along one major axis in Cartesian plane, resembling a distribution like a prolate ellipsoid.
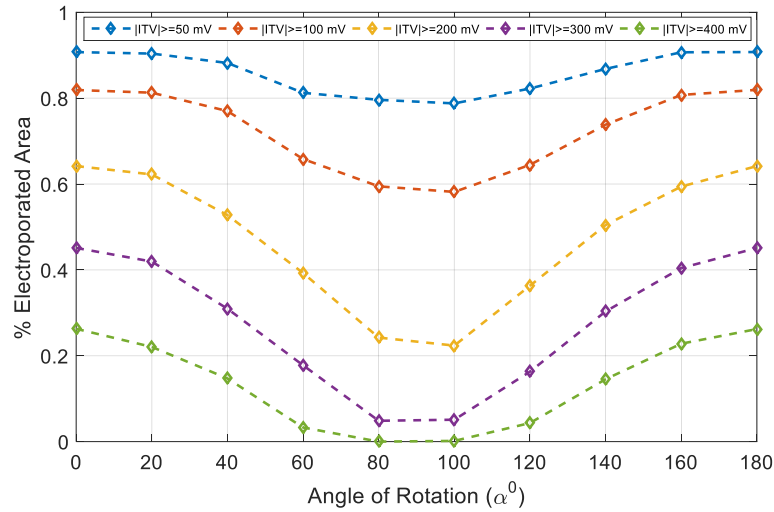
(a)
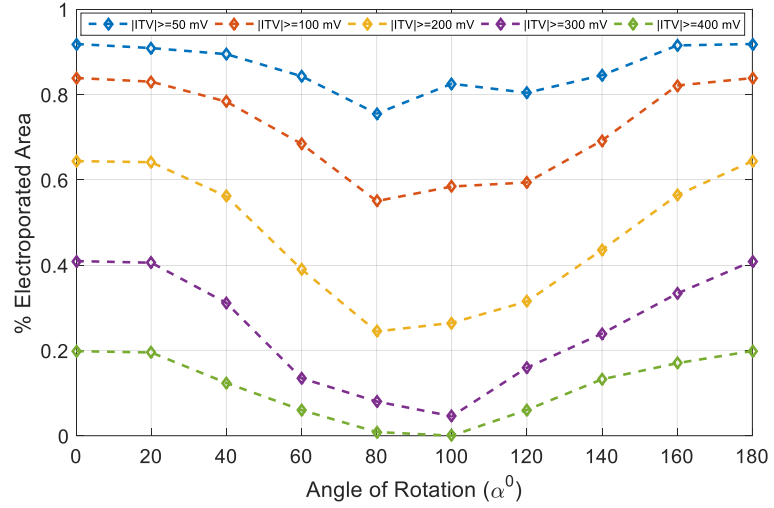
(b)
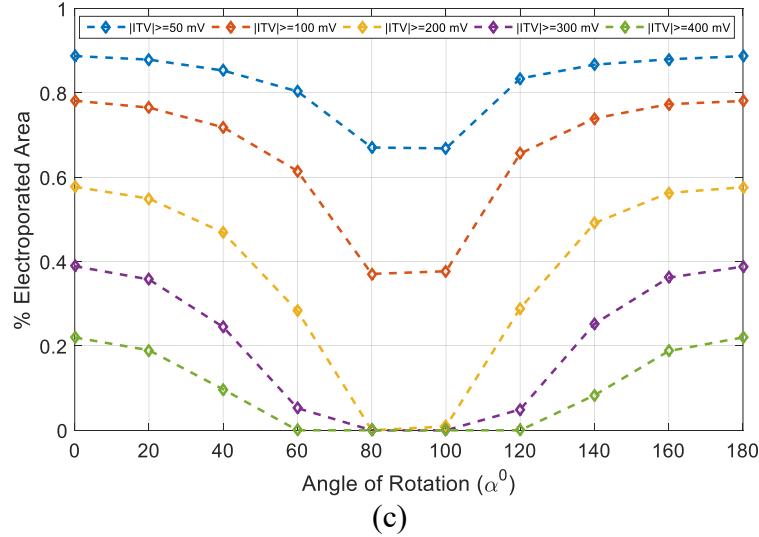
Figure 3.6 Percentage electroporated area variation with respect to angle of rotation for three cell families (a) SpunCoat (SC), (b) Porous Polysterene Scaffolds (PPS), and (c) Nanofibers (NF)

To demonstrate the difference in potentiometric distribution between a realistic cell shape and an equivalent spherical cell with same volume, we performed the steady-state ITV study on three different cell families. We compared the ITV profile over the surface of the membrane at $z = 0\,\mu$m plane for both the cell shape and their spherical replica (based on volume). As depicted in Fig. 3.7(a), the ITV profile for MG cell has satisfactory resemblance to the spherical replica because of its equiaxial distribution in 3D domain. On the other hand, NF (Fig. 3.7(b)) and SC (Fig. 3.7(c)) cells deviate significantly when compared to their spherical equivalent. The un-uniform distribution of the cell shapes results into complicated electric field distribution over the fractal geometry of the cell hence this deviation. The microenvironment of NF scaffold guides the cells to have rod like distribution hence the ITV is maximum when the principle axis of the cell is oriented along the excitation field direction. Cells grown on SC substrate form a 2D disk like distribution because of the nature of the 2D

scaffold, so ITV distribution of this specific cross-section is comparable to an ellipse rather than a sphere.

(a)

(b)

(c)
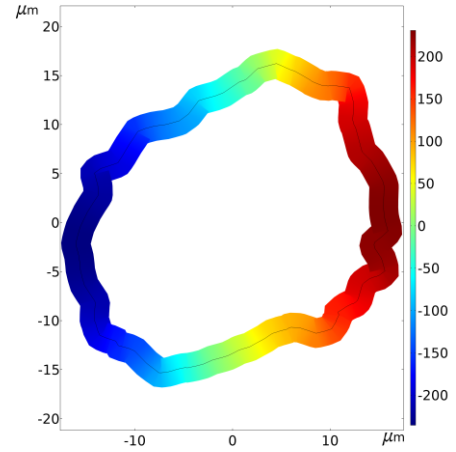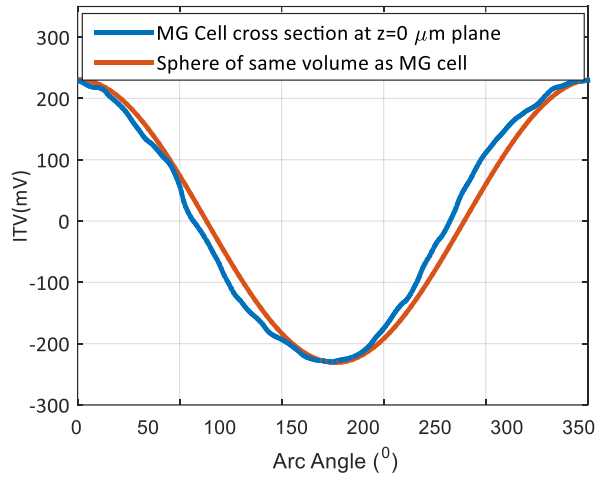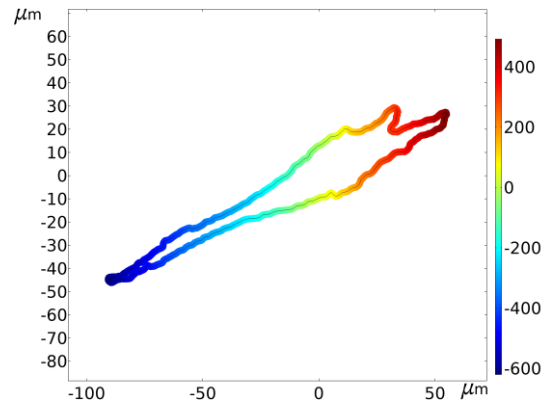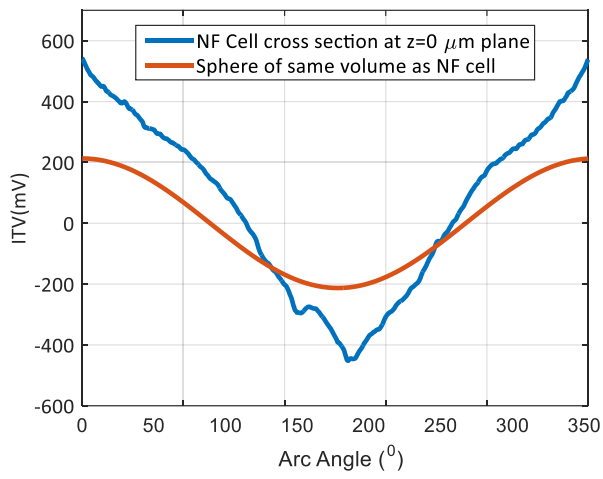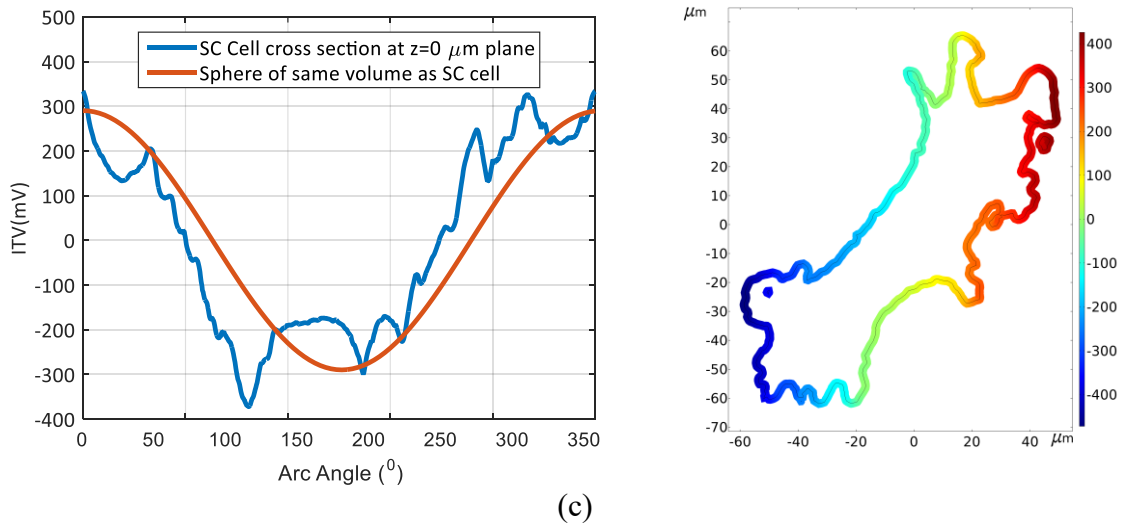
Figure 3.7 The Induced Transmembrane Voltage (ITV) profile for (a) Matrigel, (b) Nanofiber and (c) Spuncoat cell under steady-state excitation

As the theory of electroporation implies, the membrane starts forming metastable pores when the induced voltage exceeds a certain threshold. The induced transmembrane voltage is superimposed on the resting membrane potential (ranging from -20 mV to -70 mV) which is much smaller than the reported threshold voltage of electroporation (200 mV to 1 V) [70]. Therefore a first approximation to ignore the resting membrane potential is valid while considering the threshold for electroporation [65]. The electroporation threshold is obtainable from bulk electroporation through experimental setup which varies significantly in accordance to specific cell line. The specific cell line we are considering here (hBMSCs) is yet to be tested experimentally for electroporation. For simplicity, we continue our observation assuming 200 mV to be the threshold (ϕ_c) of this specific cell line. To have a measure of total electroporation due to a steady state excitation field, we implemented the method of calculating the area of the cells that experiences induced voltage more than 200 mV. The ITV for cells that are not equiaxially distributed in 3D coordinate system varies w.r.t. the size (volume), orientation and excitation field strength.

To account for the variation in orientation of these cell shapes, we have considered a parametric sweep of orientation along all x, y and z direction for each of the cells and took the average for each axis orientation. In all the cases, the excitation field was kept constant at 100 V/cm. Fig. 3.8 depicts the average electroporated area for the PPS cell. As can be observed from the trend, the average electroporated area remains almost identical irrespective of the angle of rotation. To account for the size of the shape, we have normalized the integrated area over ϕ_c by the total area of respective cell and referred it to effective electroporation rate (A^*) by definition [65]. To further validate the difference in electroporation study between a realistic cell and its spherical equivalent, we compared A* for all the 10 cell shapes with its spherical replica depicted in Fig. 3.9. We can easily describe the linear relation between the electroporation rate and size of the cell in case of spherical shape. However, the electroporation rate for the realistic cell shapes do not seem to maintain any linear relation with the cell geometrical feature. Even, the largest volume cell (CG) has the second lowest electroporation rate among all the ten cell shapes. Cells grown on 2D substrates (SC, SC+OS, CF) seems to be comparatively more permeabilized than 3D oriented cells.
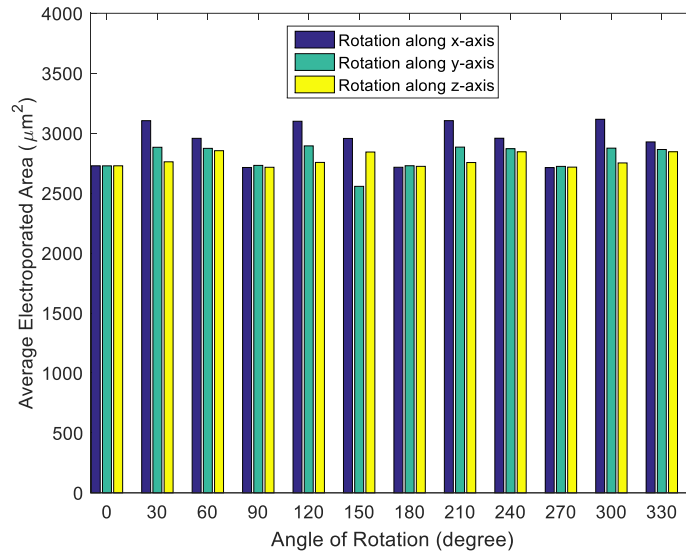
Figure 3.8 Average Electroporated area (μm^2) for a PPS cell for different rotation along x, y, and z-axis under the same steady state excitation

3.4.3 Frequency Dependent Study

Under frequency varying electrical excitation, the gain in induced transmembrane voltage observed across the cell membrane drops exponentially after a certain frequency, known as breakpoint frequency. For a spherical cell geometry, the breakpoint frequency decreases as the radius of the sphere is increased for constant membrane thickness (5 nm) as depicted in Fig. 3.10(a). To demonstrate the variation in breakpoint frequency with cell shape variation, we introduce the self-capacitance of respective cells. As can be observed from the Fig. 3.10(b), the breakpoint frequency is inversely proportional to the self-capacitance of the cell. The capacitance values are normalized by material permittivity to avoid ambiguity.
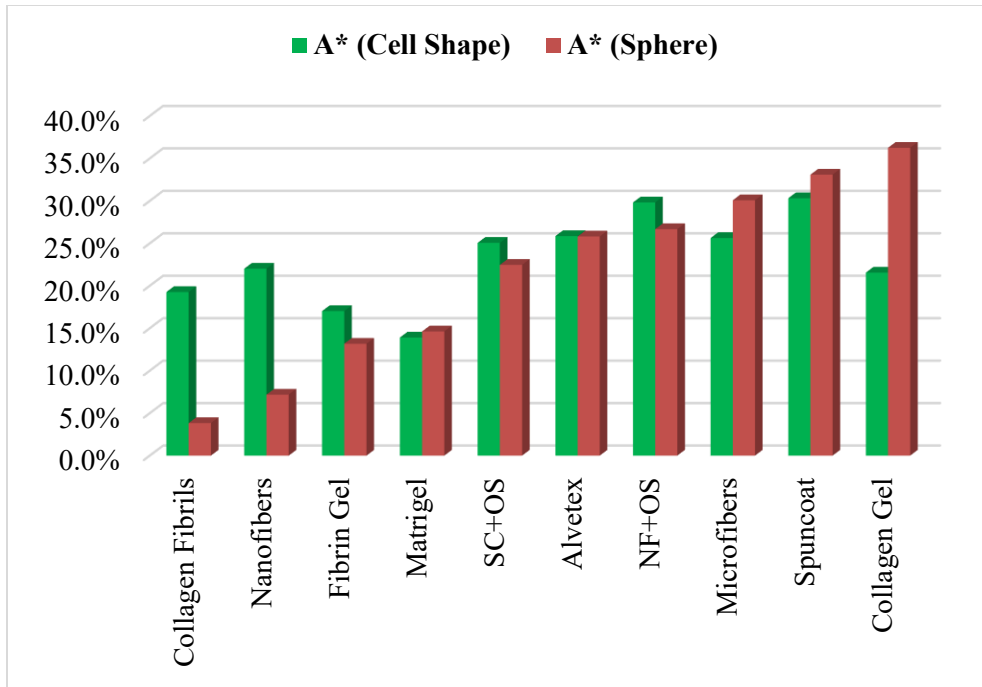
Figure 3.9 The effective electroporation rate (A^*) for the ten cell shapes considered under steady state excitation (Green) in comparison to the effective electroporation rate for a replica sphere with the same volume of respective cell (Orange)
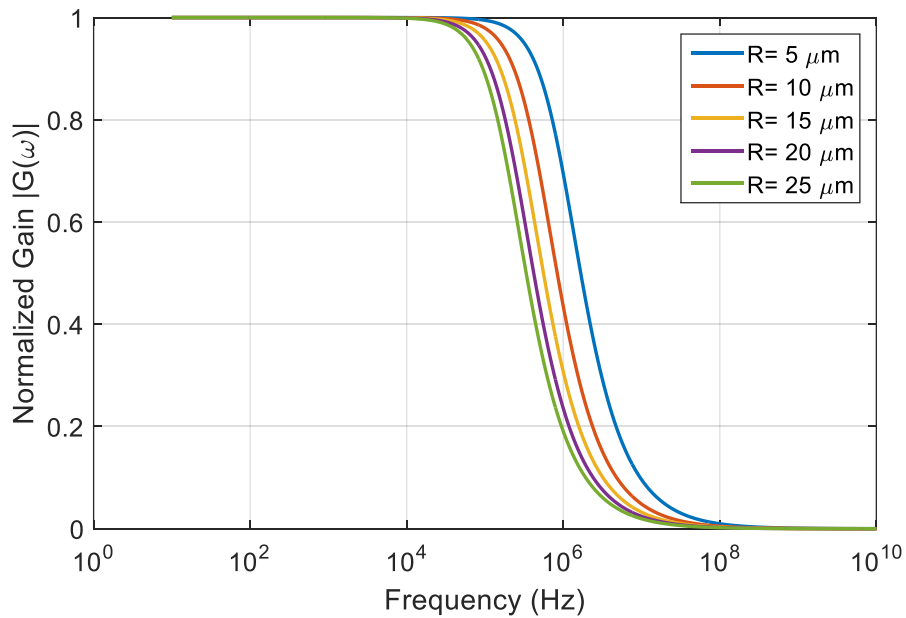
(a)
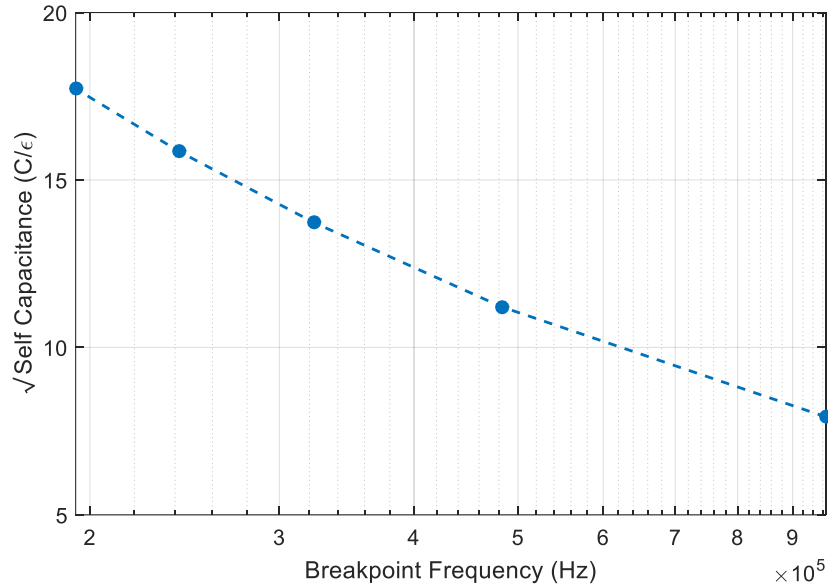
(b)

Figure 3.10 (a) Normalized gain vs frequency for a spherical cell with different radius; (b) The breakpoint frequency is inversely proportional to the self-capacitance of the sphere

Fig. 3.11(a) concludes the effect of variation in cell geometry based on a frequency dependent study. We performed a frequency dependent study over the frequency range of 10 Hz to 10 GHz to observe the variation in ITV when the excitation field comes from a variable source. To simply illustrate the complex geometrical deviation in the cell ITV we calculated the surface integral of the ITV profile of the entire cell. To nullify the effect of size variation, we normalized the surface integral by the total area of respective cells and the maximum voltage induced at low frequency and also performed average over three different excitation (i.e. the source excitation was employed in all x, y and z- directions). At low frequency, the normalized curve corresponds to a variable voltage irrespective of the size of the shape illustrating a highly insulating barrier for the excitation field to penetrate. The cell membranes resistivity starts to drop at a frequency range of 1 kHz to 10 kHZ while at very high frequency all the cells become purely conductive (i.e. presenting increased permeability). As a measure

79

of shape dependence corresponding to the breakpoint frequency, we investigated the similar

trend of self-capacitance vs. frequency plot as depicted in Fig. 3.11(b). Although the frequency

does not convey a direct relation with the capacitance, still we can observe an inverse relation

between the breakpoint frequency with respect to the self-capacitance. The Matrigel cell which

has the highest breakpoint frequency as well as lowest self-capacitance solidifies its spherical

behavior. Collagen Gel has the largest capacitance due to its 3D distribution and largest volume

among the ten cell shapes, hence has a much lower breakpoint frequency compared to other

cells
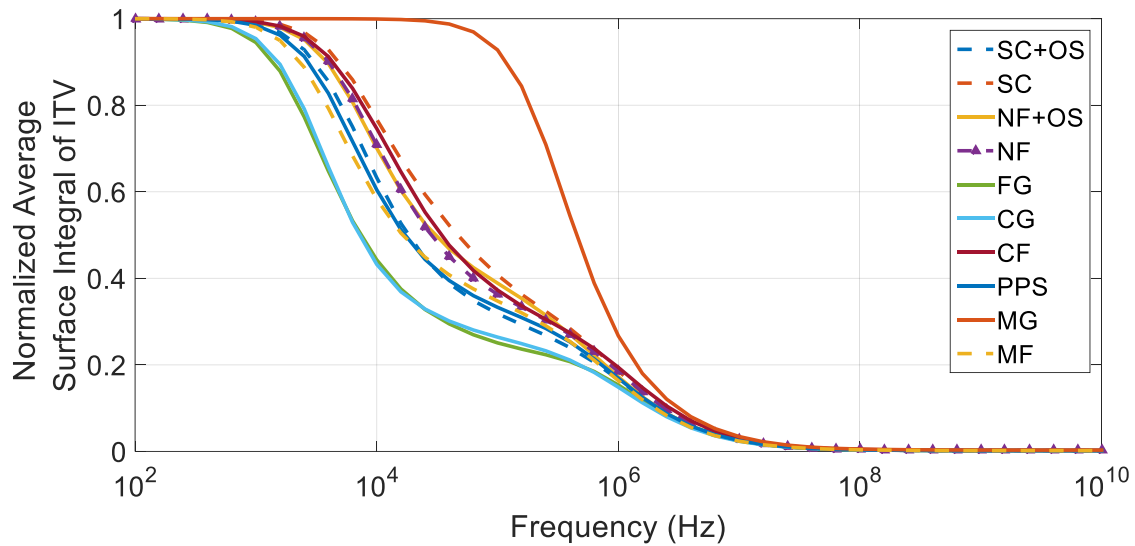
(a)
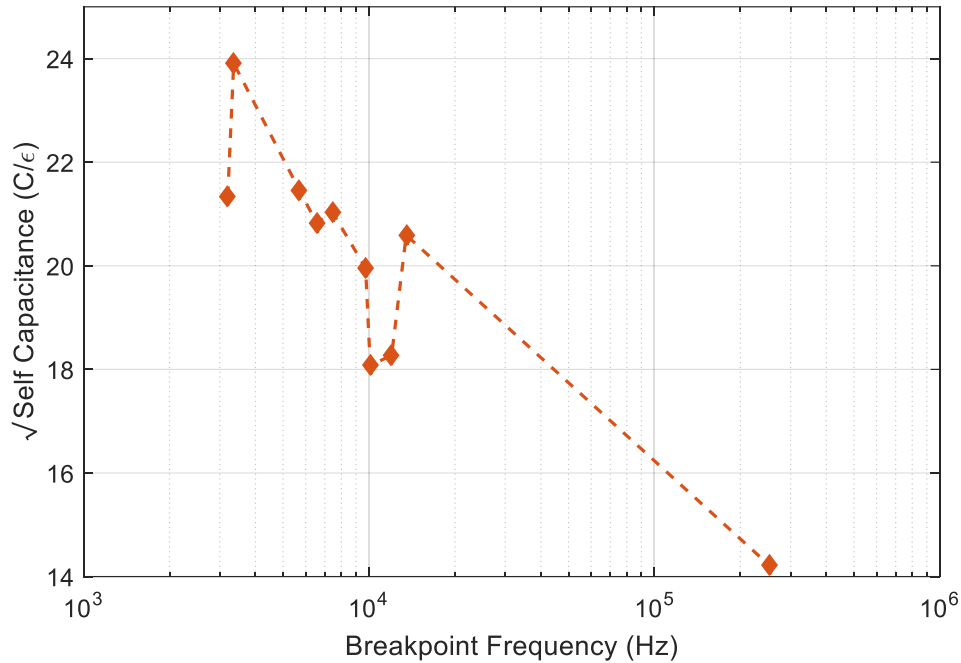
Figure 3.11 (a) Depiction of Frequency dependent study for all ten shapes (b) The breakpoint frequency vs. self-capacitance plot

3.5   Conclusion

In this study, we studied single cell electroporation (SCEP) since SCEP effectively encapsulates the effect of cell shape, size and orientation of the electric field and best suitable for optimization study to obtain desired electroporation result [75]. The Induced Transmembrane Voltage profile vary significantly from that of a spherical cell of same size depending on the distribution of the cell shapes. From the result section, we see the cell with uniform distribution (Matrigel) closely resembles the behavior of a spherical cell of same size. However, it is not true for other cell shapes like Nanofiber (rod like shape) or Spuncoat (disk like shape). Cell shape Matrigel had the lowest electroporation rate and cell shape Spuncoat had the largest. Average electroporated area for all the cell shapes remains almost identical irrespective of the alignment with respect to the excitation field.

The frequency dependent study closely resembles the behavior of a capacitive branch.

At low frequency, the cell membrane behaves more resistive and acts as an insulating barrier between the intracellular and extracellular medium, while at high frequency, the membrane becomes totally permeable to ionic current. The breakdown frequency at which the membrane becomes conductive is however related to the distribution of the cell shape.

The finding of this study questions the viability of the general assumption of considering cell shapes as sphere or ellipse or any other symmetrical shape. In case of really fractal cell shapes, the actual morphology must be taken into consideration. We have only concentrated on homogenous electrical excitation in this study. Our future goal is to expand this study to include the effect of inhomogeneous electrical excitation. Moreover, the linear membrane model considered in this study might present a hinderance towards the accurate estimation of the ITV for the hBMSC cell family. Consequently, future expansion of this study will incorporate inclusion of nonlinear membrane models, taking into account of the pore dynamics and variable membrane parameters. Also, the acquisition of the electroporation threshold for this cell family (hBMSCs) using bulk electroporation study would provide further validation of our work.

CHAPTER 4

4 A COMPUTATIONAL STUDY TO INVESTIGATE THE EFFECT OF CELL MORPHOLOGY IN SUPRA-ELECTROPORATION USING 2D CROSS-SECTIONS OF REALISTIC CELL GEOMETRIES

4.1 Abstract

The technique of using a high intensity ultra-short electric pulse with duration less than the membrane charging time to alter the internal organelles' permeability is known as Supra-electroporation. The induced electric field inside the cell such cases should be high enough to overcome the pore energy barrier, but again should maintain a short duration to ensure the pore evolution doesn't surpasses the electrical breakdown threshold. Therefore, the problem definition of the fundamental physics should incorporate the rate of change in membrane properties with formation of pores on the cell and internal organelles' membrane. In this study, we present a computational test-bed to investigate the supra-electroporation in phenomenon realistic cell shapes using a commercial Finite-element solver. Upon validating the accuracy of our model, we used it to investigate the effect of cell morphologies in electroporating internal organelles such as nucleus. To introduce a realistic variation in cell morphology, we incorporated the most advanced and accurate cell database present in the literature developed by National Institute of Standards and Technology. Our observation suggests that, supra-electroporation is highly dependent on the cell membrane irregularity, especially location of the internal organelle with respective to any protrusion on the cell surface. The results from

our observation can be utilized to engineer selective targeting of desired cell with specific morphology.

4.2 Introduction

The constituting lipid (mainly phospholipid, glycolipid or cholesterol) bilayer of biological cell membrane undergoes constant rearrangements, leading to reversible pore formation at equilibrium [66], [102]. The lifetime of these pores is very short (< nanosecond) and their hydrophobic (non-conducting) nature only allows permeation of selective molecules into the intracellular medium, thereby giving rise to the insulating behavior of the cell membrane from electrical point of view [66], [103], [104]. Exposing a biological cell to external electrical excitation gives rise to several biophysical and biochemical responses, such as electroporation (uniform electric field), electrorotation (rotating electric field) or dielectrophoresis (non-uniform electric field) [105]. When the excitation electric field strength is high (0.1 kV/cm – 100 kV/cm) and short in duration (1 ns - 1 s), the membrane goes through formation of stable hydrophilic (conducting) pores due to the induced electric potential, hence altering the permeability of the membrane [79], [104]. The lifetime of these pores varies depending on the excitation field strength and duration, and may diminish (reversible) or cause mechanical rupture in the cell membrane (irreversible), if expanded beyond recovery [79], [104]. This physical phenomenon is hence referred as electroporation or electropermeabilization.

Electrically, cell membrane has a lower relative permittivity (~ 5) and very low conductance ($\sim 3 \times 10^{-7}$ S/m) compared to the surrounding extracellular medium (relative permittivity (~ 80) and conductance (~ 1.2 S/m)) *in vitro* or *in vivo*. Hence, when exposed to

an electrical excitation, charges get accumulated at the membrane surface and therefore, a stronger intracellular electric field gets generated [106]. If the excitation pulse duration is shorter than the membrane charging time (nanosecond or subnanosecond), the excitation field can interact with intracellular organelles and induce electroporation at the intracellular membrane surfaces [104]. This technique of using ultrashort (nanosecond), high intensity pulsed electric field (nsPEF) to electroporate internal organelles is known as Supra-Electroporation [79], [104], [107]. Over the last decade, the nsPEF has gained significant interest for its capability to interact with mitochondria, nucleus, endoplasmic reticulum, and several other internal organelles without disrupting the structural integrity of the cell membrane to a great deal [108]–[113]. Some recent studies have explored application of nsPEF in neuromuscular stimulation [114]–[116], formation of ion-selective nanopores in cell membrane [117], [118], and even activating voltage-gated channels [116]. Additional experimental evidence suggests that nsPEF can trigger apoptotic cell death stimuli, which can prevent local inflammation otherwise present in case of cell or tissue ablation by irreversible electroporation (IRE) [119], [120] and can provide selectivity towards cancerous cells [121], [122]. More recent developments utilize the nsPEF for localized electroporation protocol into the cell [123], [124].

Since the discovery of electroporation, a plethora of studies have been conducted to explain and understand the phenomenon and explore the effect of cell size, shape, orientation and excitation parameters on the outcome of this clinical modality. From research standpoint, *in-silico* models are more preferred than *in-vitro* or *in-vivo* experiments because of its simplicity and reduced cost in setup. To date, numerous computational models of electroporation validated by experimental evidence have been reported, which can be broadly

catagorized in two major categories: molecular dynamic (MD) simulation and electrical characterization of the cell membrane pore formation. While the MD simulation focuses on membrane kinetics from molecular point of view and reproduces the temporal profile of pore creation and evolution, the electrical characterization considers the spatial and temporal distribution of induced transmembrane voltage (ITV) and conductivity and permittivity of a uniformly distributed membrane. Combined hypothesis from these study states, when exposed to a high enough electric field excitation, ITV at the membrane surface increases and when it goes beyond a specific threshold, the energy required to form hydrophilic pores gets lowered and numerous pores start forming on the membrane surface hence increasing the permeability of the membrane [125]. Since, these pores are often short lived and minuscule in size, experimental validation of existence of such a physical entity was not proved, until recently a study presented experimental validation of nanopore formation in lipid vesicles that agrees with molecular dynamic solution of pore formation [113].

Both analytical and numerical models along with experimental validation have confirmed that shape and orientation of the target cell has a major impact on the electroporation studies [93]. However, most of these studies incorporated simplified geometries like spheres or spheroids and even in case of realistic 3D shapes, the primary focus was only on conventional electroporation protocol [89], [93]. One more recent study incorporated supra-electroporation in their numerical model, focusing on the pore formation dynamics on cell membrane as well as nucleus membrane [126]. Although, the focus of their study was also concentrated on the effect of cell shape in supra-electroporation phenomenon, however the asymmetry in realistic cell shapes was not entirely analyzed. Our goal in this study is to investigate and analyze the effect of most random variation in cell morphology on supra-

86

electroporation characteristics. To achieve this goal, we have incorporated most advanced 3D

cell map developed to date and the degree of asymmetry in case of the cells considered in our

study is much higher in comparison. We will demonstrate the validation of our incorporated

computational platform and implement it moving forward to bridge the existing gap in supra-

electroporation literatures.

The organization of this manuscript is as shown: in section 4.3, we present a brief introduction

of the pore formation dynamics and its relation with membrane free energy. We also introduce

the procedure adopted in this study to incorporate the NIST cell database and the

methodologies we used to create 2D cross-sections from imported 3D cell geometries. In

section 4.4, we analyze the supra-electroporation behavior of various cell morphology and

discuss on the effect of relative position of the nucleus inside the cell. Finally, we draw

conclusions from our observations in result section in subsection 4.5.

4.3   Background and Methodology

4.3.1   Pore Energy and Radius

The free energy ΔW associated with pore of radius r at a certain transmembrane voltage V_m is

given by (4.1) [125]

$$\Delta W(r, V_m) = \begin{cases} \Delta W_o(r, V_m) = 2\pi r d_m \Gamma_o \frac{I_1\left(\frac{r}{\lambda}\right)}{I_o\left(\frac{r}{\lambda}\right)} - \frac{(\varepsilon_e - \varepsilon_m)\pi r^2}{2d_m} V_m^2; & r < r^* \\ \Delta W_i(r, V_m) = 2\pi r \gamma(r) - \Gamma_i \pi r^2 - \frac{(\varepsilon_e - \varepsilon_m)\pi r^2}{2d_m} V_m^2; & r > r^* \end{cases} \tag{4.1}$$

where, ε_e and ε_m are the permittivity of extracellular medium and cell membrane, ΔW_o

and ΔW_i are pore energy associated with hydrophobic and hydrophilic pores respectively, I_k

is the Bessel function of kth order and γ is the edge tension, which is a function of pore radius

r; $r^*(\sim 0.5$ nm$)$ is the transitioning radius at which energy of the hydrophilic and hydrophobic

pores coincides i.e. $\Delta W_o = \Delta W_i$ (Fig. 4.1(a)). Beyond r^*, all pores are hydrophilic in nature and would expand until $r_{pmin}(\sim 0.8$ nm) to achieve a minimum energy state. Fig 4.1(b) illustrates the pore energy revolution for varying transmembrane voltage V_m and as can be observed at higher V_m, there exists a second maximum r_{max} of the membrane energy vs. pore radius curve. This pore radius corresponds to threshold for irreversible breakdown. This span between r^* and r_{max} addresses the metastability of the pores and would reduce as V_m is increased. Hence, by inducing transmembrane voltage on the cell membrane surface with the help of external electrical excitation, one can engineer different clinical modality to either manipulate the membrane permeability or introduce cell death by nonthermal ablation.

(a)

(b)
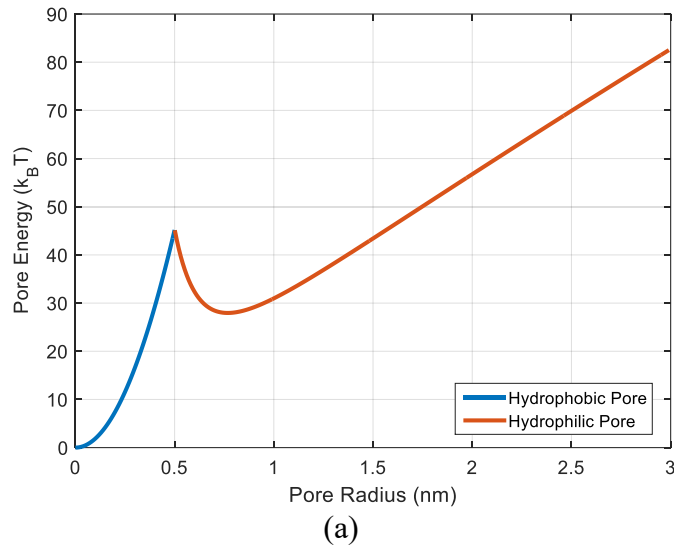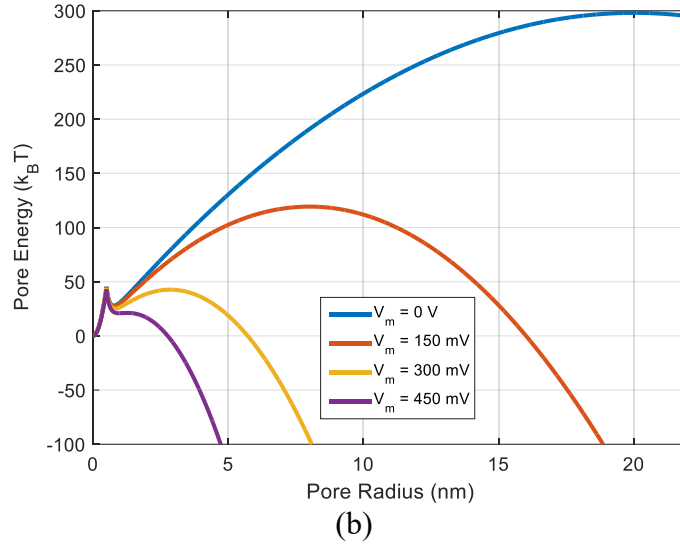
Figure 4.1 (a) Membrane free energy for hydrophobic and hydrophilic pores at $V_m = 0$ V (b) dependence of pore energy on transmembrane voltage (V_m)

The dynamics of pore population and evolution can be explained theoretically by Smoluchowski equation (4.2), which describes the pore density distribution function $n(r, t)$ (pores per unit membrane area per unit pore radius) in a membrane as a function of time t [127]

$$\frac{\partial n}{\partial t} = D_p \frac{\partial}{\partial r} \left[\frac{\partial n}{\partial t} + \frac{n}{kT} \frac{\partial W_i}{\partial t} \right] + S(r) \qquad (4.2)$$

Here, D_p is the diffusion coefficient of pores and $S(r)$ is the pore source term that determines the transition between hydrophobic (W_o) and hydrophilic (W_i) pores. Several studies have already incorporated pore growth to account for pore radius evolution [126], [128]–[133]. However, these approaches are highly complicated from computational perspective, when analytical solution of the induced transmembrane voltage is unavailable and incorporating a complete set of Smoluchowski equation (SE) to account for pore radius evolution with time is beyond the scope of our study. A quasi-static asymptotic version of the SE can be achieved by assuming all pores have the same time-invariant radius [89], [104],

[127], [134], [135]. According to the asymptotic model, the pores are assumed to be hydrophilic and their radius instantaneously increase to achieve $r_{pmin}(\sim 0.8$ nm), which is a valid approximation as long as the excitation pulse is in sub-microsecond range and can interact with the internal organelles [104], [128]. In case of nsPEF, the source term dominates the diffusion and drift term associated with the pore radius in (2). The modified rate of change in pore density N (per unit membrane area) with transmembrane voltage V_m is governed by (4.3) [127]

$$\frac{dN(t)}{dt} = \alpha e^{\left(\frac{V_m}{V_{ep}}\right)^2}\left(1 - \frac{N(t)}{N_0 e^{q(V_m/V_{ep})^2}}\right) \tag{4.3}$$

In (4.3), V_{ep} stands for the characteristics voltage for electroporation, N_0 is the steady-state pore density at $V_m = 0$ V, α is the pore creation rate constant and q is electroporation constant. From computational standpoint, formation of pores on the membrane surface effectively alters the membrane permeability, which can reflected by incorporating associated change in membrane conductivity.

4.3.2 Linear and Nonlinear Membrane Model

The primary step in modelling electrical characterization of electroporation phenomenon is to solve for transmembrane voltage induced over the course of cell membrane under external electric excitation. This specific problem definition is similar to the fundamental physics of dielectric inclusion in a conductive medium. The cell membrane representing a low conductivity (σ_m) layer between the extracellular and intracellular matrix gives rise to spatially and temporally varying transmembrane voltage (V_m) under external excitation which can be solved from the Laplace equation (4.4) [104].

$$-\nabla.\frac{\partial}{\partial t}(\varepsilon_m \nabla V_m) - \nabla(\sigma_m \nabla V_m) = 0 \tag{4.4}$$

In case of linear membrane model, change in the membrane conductivity is ignored, which may yield close approximation to the actual scenario in case of DC or low-frequency excitation [104]. Close form or analytical solution of (4.4) exists for regular shapes like ellipsoids or spheres and shows excellent agreement with experimental measurements [93], [100]. These studies also conclude that cell shape, size and orientation have significant impacts on the induced transmembrane voltage of a cell membrane besides electrical excitation parameters. In contrast, cells with irregular geometries are not mathematically representable in close form, hence analytical solution in such case are not possible. This drawback is addressed by several studies by incorporating numerical methods to compute the induced transmembrane voltage of irregular cell shapes [93], [94]. The conclusion of these studies reflects on the significance of considering the actual cell morphology in computational modelling of electroporation.

However, the fundamental limitation of the linear membrane model is it does not incorporate dynamic change in membrane conductivity due to formation of pores, and hence cannot validate stimulation pulses with sub-microsecond pulse-width and can interact with the internal organelles [104]. Equation (4.5) incorporates the dynamic change in membrane conductivity due to pore formation

$$\sigma_m(t) = \sigma_{m0} + N(t)\sigma_p * \pi r_p^2 * K \tag{4.5}$$

where, $K = \dfrac{e^{v_m}-1}{\frac{w_0 e^{w_0-nv_m}-nv_m}{w_0-nv_m} e^{v_m} - \frac{w_0 e^{w_0+nv_m}+nv_m}{w_0+nv_m}}$ and $v_m = V_m * \frac{q_e}{kT}$. The associated parameter definitions in (4.5) along with some of the key parameters used in our computational modelling are presented in Table 4.1. Nonlinearity in the model arises from the conjunctive coupling

between (4.3) to (4.5). To observe the effect of cell morphology in supra-electroporation study, we have implemented this nonlinear membrane model on both the cell and nucleus membranes of uniform thickness. We have used COMSOL Multiphysics, a commercial finite element solver to implement the physics definition [43]. We have incorporated the Electric Current (Time Domain) solver to solve (4.4) and a weak form PDE solver to solve (4.3) in the multiphysics domain. The membrane kinetics is incorporated in multiphysics domain by implementing a "contact impedance" on the cell and nucleus boundary of the imported cell geometries.

Table 4.1 Parameter list used to design the computational model and associate description [89], [134]

Parameter	Symbol	Value
Pore creation rate density	α	$1\text{x}10^9\ m^2/s$
Characteristic voltage of electroporation	V_{ep}	$224\ mV$
Equilibrium pore density	N_0	$3.3\text{x}10^6\ m^{-2}$
Pore creation rate	q	2.46
Pore energy barrier	w_0	2.65
Relative entrance length of pores	n	0.15
Temperature	T	$295\ K$
Electron charge	q_e	$1.6\text{x}10^{-19}\ C$
Conductivity inside pore	σ_p	$1.2\ S/m$

Pore radius	r_p	$0.8 \, nm$
Membrane conductivity	σ_{m0}	$9.5 \times 10^{-9} S/m$
Membrane relative permittivity	ϵ_m	5

4.3.3 NIST Stem Cell Database

The stem cell database incorporated in our study was developed by National Institute of Standards and Technology (NIST) by culturing a cell line of human bone marrow stromal cells (hBMSCs) in ten different microenvironments and imaging them using confocal laser imaging microscopy to obtain a 3D surface and volumetric mesh of each cell and its respective nucleus [30]. The physical interaction between the cell and its surrounding medium dictates the morphological distribution of the cell [17]. Hence, by engineering ten different microenvironments, researchers were able to demonstrate successful implementation of cellular morphotyping and obtained a wide range of variation in cellular distribution [25]. Thousands of cells and their corresponding nuclei map are categorized in ten different family according to their culturing microenvironment and readily available in an open source database for research purposes [28]. We have incorporated one cell from each of the ten families in our study, the identifiers of which are listed in Table II. The 3D cell maps along with their respective nuclei are randomly oriented. Since our primary focus is concentrated on the cell morphology only, we employed similar orientation protocol for all cells.

In our previous study, we have introduced an accurate computational algorithm to calculate the polarizability of these cells, an electrical characteristic equivalent to cellular dimensionality, which is directly correlated with the induced transmembrane voltage [95], [100]. To compensate the randomness in orientation, the cells from Table 2.1 were

diagonalized based on their respective polarizability matrix, which rotated the principal axes of each cell and its' nucleus to be aligned with the *x*, *y*, *z*- axis of the 3D Cartesian coordinate system. This operation resulted the cells' largest dimension aligned towards the *x*- axis and the smallest dimension towards the *z*- axis. Then the cell and corresponding nucleus was transferred to the center of mass of the nucleus. After that, a 2D cross-section was taken at $z=0$ μm of all cell (Fig. 4.2). As can be observed from Fig. 4.2, the cells incorporated in our study demonstrates a wide range of morphological variation from needle like shape (NF) to circular shape (MG). For simplicity in identification each cell is referred to their respective family name from Table 2.1. The excitation protocol we used in this study was a 71 ns wide pulse with 6ns rise time 10 ns fall time.
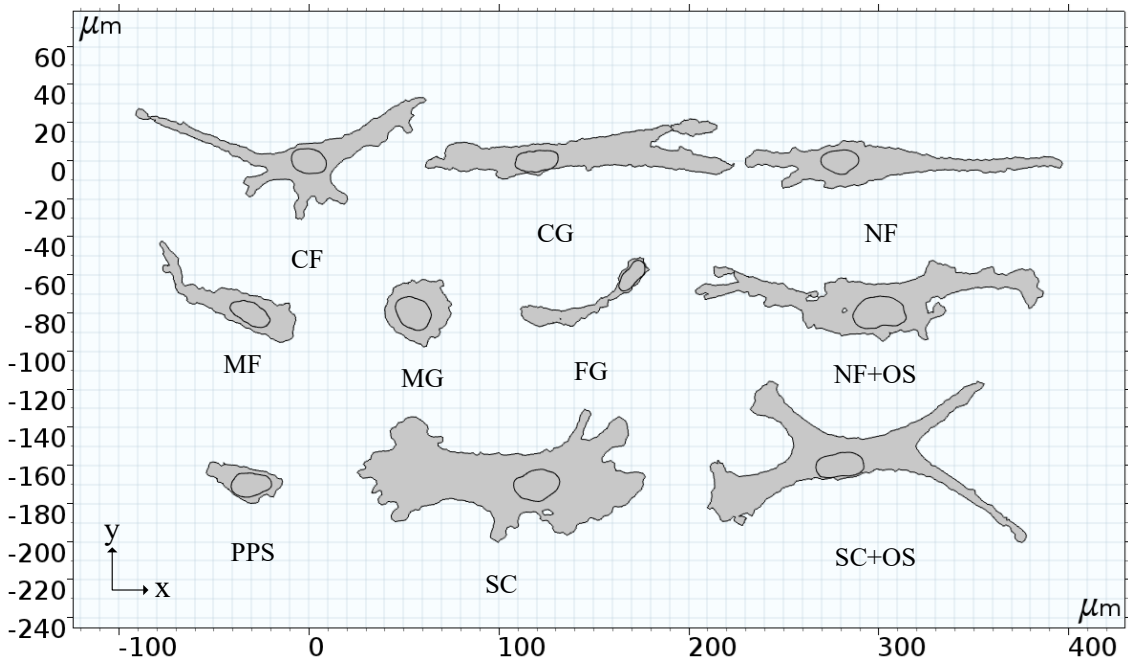
Figure 4.2 A 2D cross-sectional view of the stem cell morphologies along with embedded nucleus considered in this study

4.4 Results and Discussion

4.4.1 Effect of Cell Shape on Supra-EP

The first set results we would be discussing is the pore density distribution on the cell and nucleus membrane for different cross-sections. For brevity, we are focusing on three of the ten cell sections with highest degree of randomness (i.e. MG being near circular, SC being 2D disk and CF being random in distribution). While the excitation electric field plateau (i.e. $\overline{E_0}$) is 16 kV/cm, pore density on cell and nucleus membrane at 10 ns, 15 ns, 20 ns and 30 ns time stamps are depicted in Fig. 4.3. Overall, portion of the cell or nucleus membrane facing the electrodes electroporates at a faster rate than neighboring region. A closer look of pore density at nucleus membrane demonstrates CF cell nucleus is approaching onset of electroporation at 15 ns, whereas SC cell nucleus is still nonporated. At later time stamps, CF cell nucleus reaches pore density equilibrium prior to MG and SC cell sections. This observation clearly highlights the effect of cell morphology on the supra-electroporation characteristics of cells.
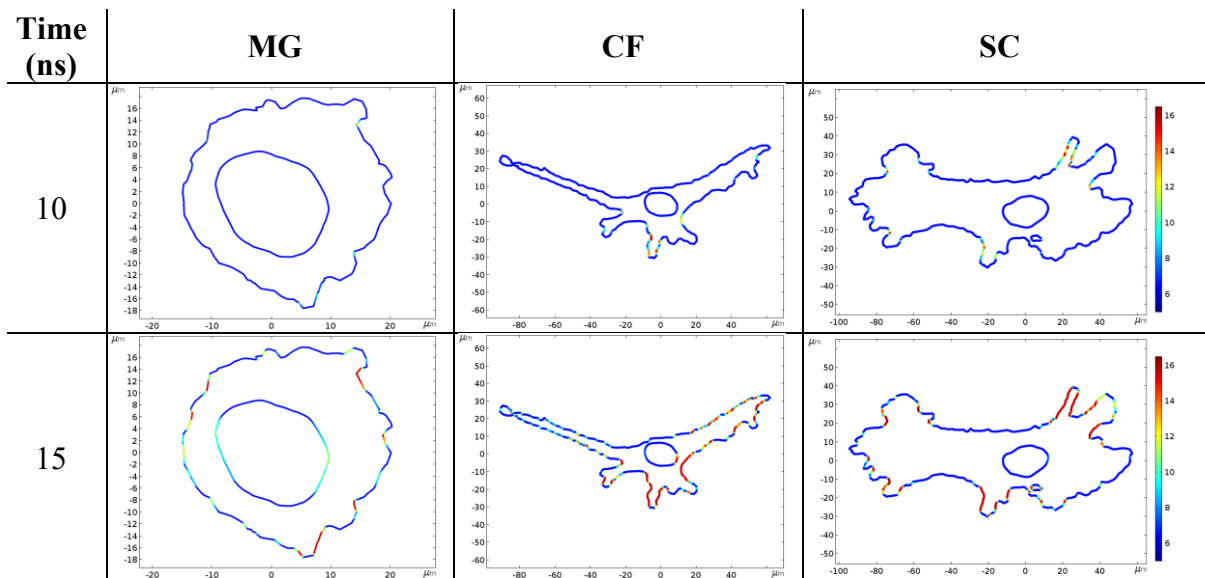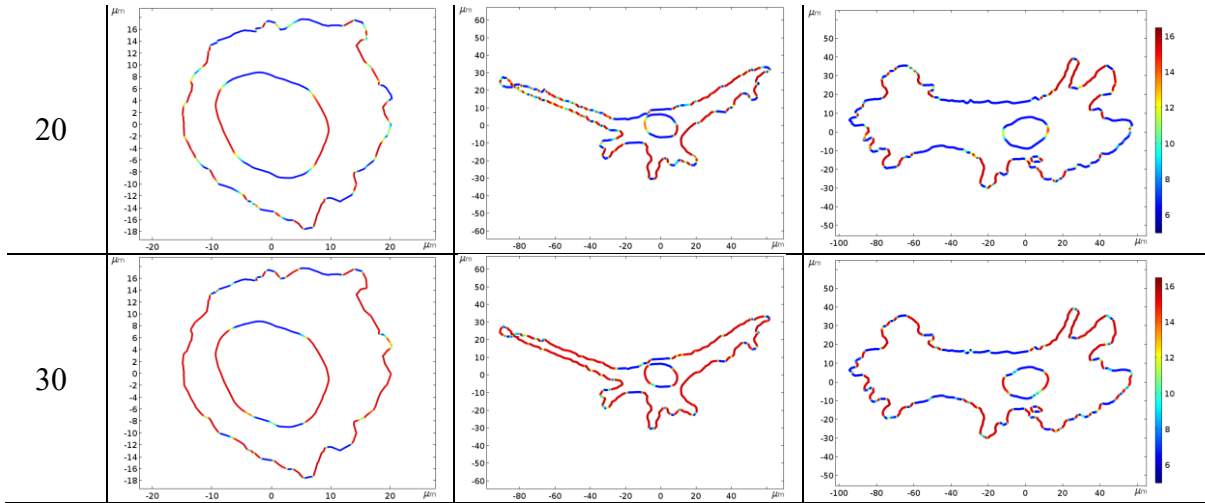
Figure 4.3 Pore density distribution on the cell and nucleus membrane at three separate time stamps

A more convenient alternative to draw conclusive remarks of the Supra-EP phenomenon is to inspect the surface average pore density profile. Average pore density is calculated by taking a line integral of the pore density along the perimeter of the nucleus ($\int N_{ij(t)}.dl / \int dl$). To illustrate the effect of cell shape on nucleus characteristics, we investigate three different cases of regular cell shapes in Fig. 4.4, under identical excitation field along x-axis. Here, a and b are the major and minor semi-axes of the ellipse respectively. The third case is a circular cell with radius mapped in a way to have the same area as the ellipses. In all cases, the embedded nucleus is circular in shape with a radius of 2 μm. The observation suggests that, when the major semi-axis of the ellipse is perpendicular to the excitation field ($a < b$), the pore density reaches equilibrium much faster with respect to the cases where the major semi-axis is parallel to the excitation field direction ($a > b$). This is because, when the major semi-axis of an elliptical cell is aligned perpendicular to the electric field, comparatively more portion of the cell is exposed to the electric field normal component, resulting in an expedited transmembrane voltage threshold progression, hence the excitation field can penetrate inside the cell more rapidly to electroporate the nucleus. The normal electric

96

field distribution stamp at 50 ns depicted in inset, illustrates the ellipse with semi major axis a $< b$ experiences a larger field strength. We have also confirmed this phenomenon using close form expression of the induced electric field inside a cell [100], depicted in Fig. 4.5. The close form solution does not incorporate the pore formation dynamics, still we observe similar behavior (i.e. larger electric field intensity) for 2D elliptical cell with major semi-axis aligned perpendicular to the excitation field direction, which validates our observation that cell orientation with respect to the excitation direction is an important aspect to consider in electroporation studies.
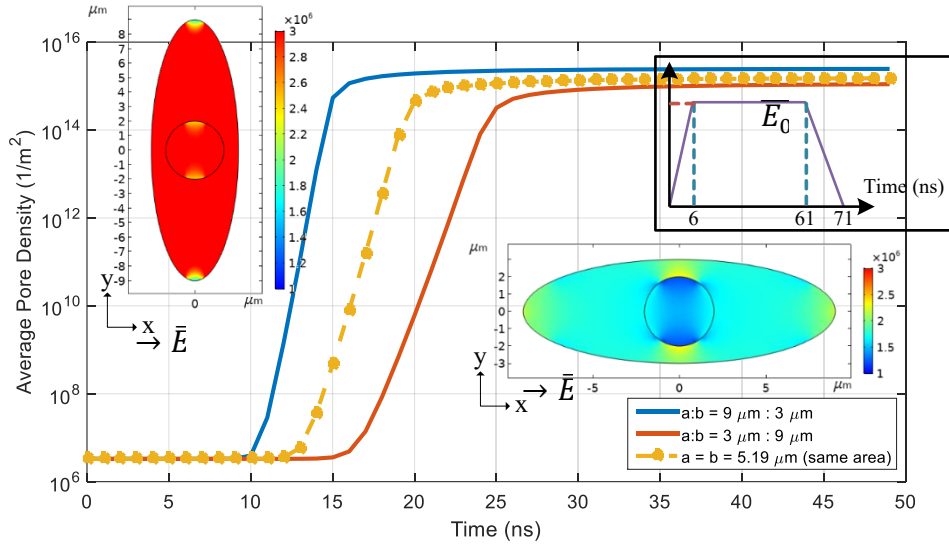
Figure 4.4 A comprehensive comparison between three cases of ellipse depicting the effect of orientation and cell shape in the study of supra-electroporation
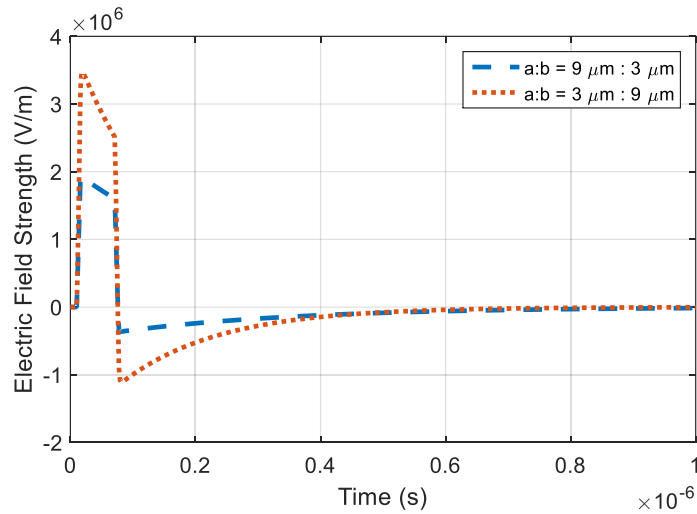
Figure 4.5 Close form implementation of induced electric field inside the cell with two different aspect ratios

Considering the observation from above discussion, we present the pore density distribution on the nuclei of the cells listed in Table 2.1 in Fig. 4.6. For a 16 kV/cm excitation intensity, as can be observed from Fig. 4.6(a), CG nucleus demonstrates the slowest response, since the cell shape distribution is larger along the electric excitation direction (i.e. similar behavior as ellipse with $a > b$). The slanted alignment of the FG cell and embedded nucleus

98

results in faster pore density saturation under identical electrical excitation. There is also a significant difference in the saturated pore density, depicting the variation in cell shape is a major contributor to supra-electroporation characteristics. In Fig. 4.6(b), we demonstrate the effect of excitation field intensity variation. As we increase the excitation intensity from 16 kV/cm to 32 kV/cm, the relative response of all the cell shapes remains the same as 16 kV/cm excitation, but overall response for all cases shows much faster response and increased equilibrium pore density.
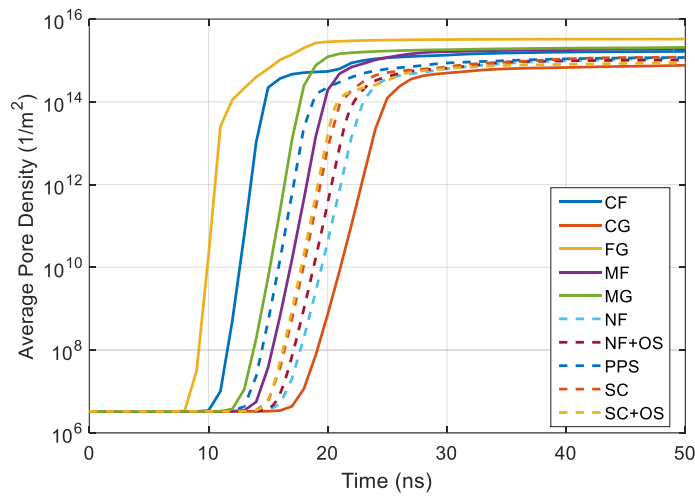
(a)
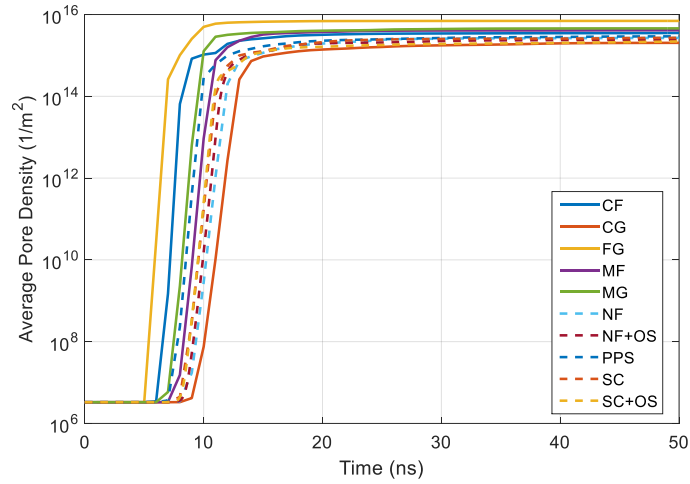
(b)

Figure 4.6 Average pore density profile on nucleus membrane for all cells listed in Table 2.1

under (a) $\overline{E_0} = 16$ kV/cm and (b) $\overline{E_0} = 32$ kV/cm

4.4.2 Effect of Nucleus Shape on Supra-EP

Moving forward, we analyzed the effect of the nucleus morphology in supra-EP study in Fig 7. We replaced the original nucleus in Fig. 2 with an identical circular nucleus with 4.5 μm radius (4.5 μm was the maximum radius of a circle that can fit into all the cell sections). As can be observed by comparing with Fig. 6(a), some cells exhibit delayed response of electroporation onset (such as FG, CF), while supra-EP response in case of some other cell morphologies (such as SC, MG) remain unchanged although their nucleus distribution is not equiaxial (i.e. circular in shape). This observation concludes that, internal organelle morphology also plays a significant role in the temporal distribution of pores in supra-EP phenomenon.
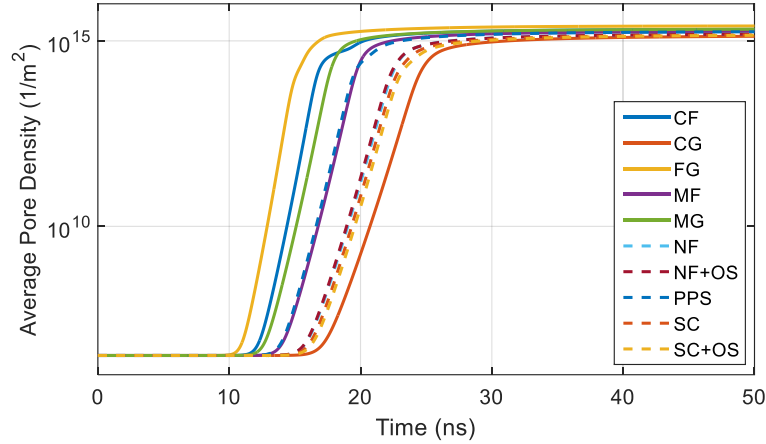
Figure 4.7 Average pore density distribution on the nucleus membrane when a circular analog of 4.5 μm is embedded inside the cells ($\overline{E_0} = 16$ kV/cm)

4.4.3 Effect of Cell Orientation and Excitation Direction

As we have observed from the discussion of Fig. 4.4, orientation of the cell with respect to the excitation field direction is another major contributing factor in supra-EP characteristics. We have solidified this statement by demonstrating two orthogonal excitation direction for the cells considered in this study, depicted in Fig. 4.8. As shown in Fig. 2, 2D cross-section of most of the cells are distributed more along $x -$ axis. Hence, when the excitation direction was flipped to $y -$axis, we observed comparatively faster electroporation onset on the nucleus membrane of the cells considered in this study (similar response as an ellipse with $a < b$). The most prominent difference is observed in case of CG cell-section since this cell section morphologically resembles a 2D ellipse with semi major axis $a < b$. The only exception was observed in case of FG cell-section since this 2D section is not specifically aligned with either of the $x -$ or $y -$ axis.
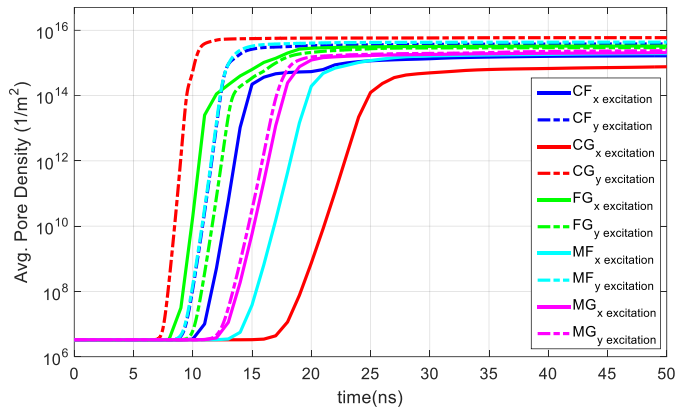
(a)
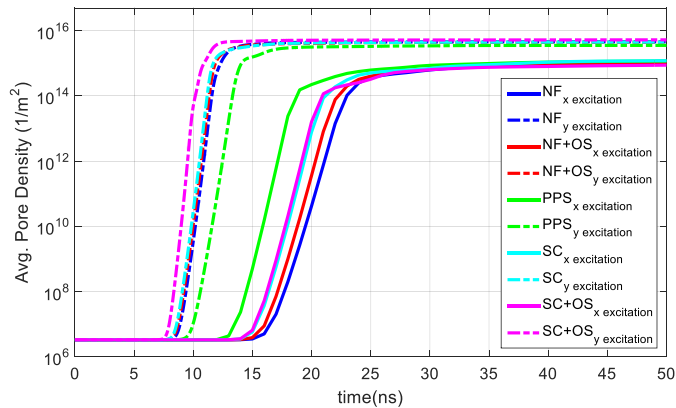
(b)

Figure 4.8 Comparison of pore density distribution on the nucleus membrane of (a) CF, CG, FG, MF, MG cell sections and (b) NF, NF+OS, PPS, SC, SC+OS cell sections under $x-$ and $y-$ axis excitation

4.4.4 Effect of Nucleus Location on Supra-EP

To illustrate the effect of relative position of the nucleus inside the cell, we performed a parametric study by varying the nucleus location inside NF and SC cell section while the exciation field direction is along (+)ve $x-$ axis, as depicted in Fig. 4.9. For NF cell-section (Fig. 4.9(a)), the observation suggests that positioning the nucleus closer to the anode will result in expedited nanopore formation. In contrast, we observe a random behavior in case of

SC cell section. Therefore, it is evident that the relative distance of the nucleus with respect to the excitation electrodes are not of significant consideration in supra-EP study.
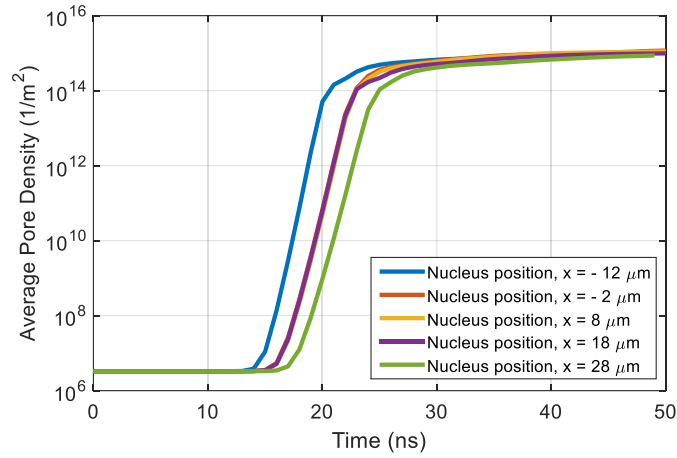
(a)
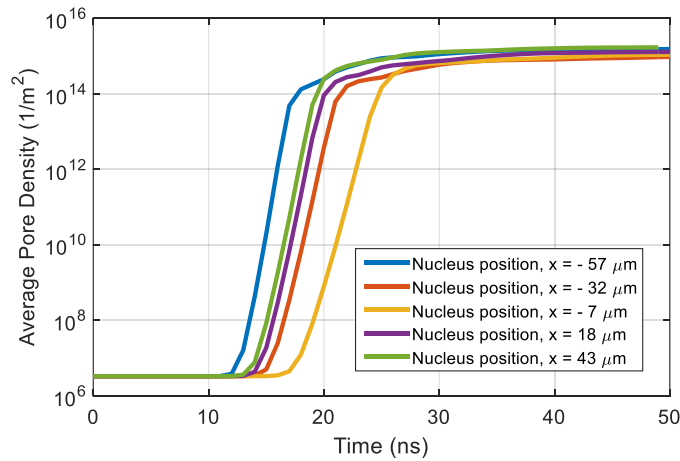
(b)

Figure 4.9 Effect of nucleus location inside the (a) NF and (b) SC cell section when the excitation field in along $x-$ axis with $\overline{E_0} = 16$ kV/cm.

To investigate this observation further, we have performed a similar study with variable nucleus location inside a regular ellipse and a deformed ellipse with protrusion (Fig. 4.10(b)). In case of the regular ellipse cell, varying the nucleus location inside the cell apparently had no effect of the supra-EP characteristics of the nucleus. In contrast, when the nucleus was located near the protrusion, comparatively faster rate of nanopore formation was observed on the nucleus membrane (Fig. 4.10(a)). The major contributing factor in such observation can be identified from the normal field distribution inside the cell. The induced electric field intensity inside the cell reaches steady state just after the onset of external excitation (around 10 ns). We present the normal electric field intensity induced inside the cell at $t = 10$ ns time in Fig. 4.10(b). The top illustration depicts the penetration of a high intensity electric field inside the nucleus when it is placed relatively close to the protrusion ($x = $ -11 μm), whereas when the nucleus is located far from the protrusion ($x = $ -33 μm), induced electric field strength is comparatively lower. Hence, nanopore formation is delayed in case of nuclei that are located far from the irregularity of the cell. This observation is in accord with the findings of the study of Puichar [89], where they reported pronounced electroporation of the cell around the protrusions facing electrodes. However, their finding was only limited to the effect of pore formation on the cell membrane and the impact of the induced electric field was not analyzed in their study. Therefore, by controlling the electroporation time, the results in Fig. 4.7-Fig. 4.9 can be used for the selective supra-electroporation of cells with specific morphologies and nucleus positions.
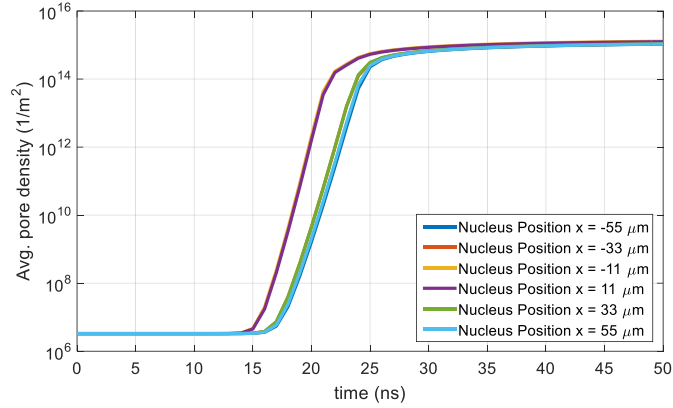
(a)
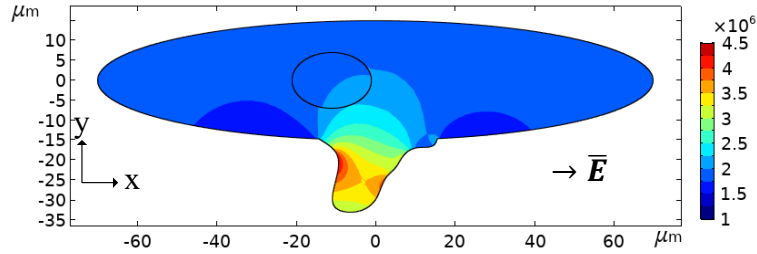
(b)

Figure 4.10 (a) Average pore density on the nucleus membrane of a deformed elliptical cell under $\overline{E_0} = 16\ \text{kV/cm}$ along $x-$ axis (b) Induced normal electric field intensity at $t = 10$ ns

4.5   Conclusion

The primary focus of this study was to investigate the effect of actual cell morphology in supra-electroporation study. We have incorporated a nonlinear numerical model that employs the pore dynamics during electroporation phenomenon and implemented it on a wide variety of actual cell morphology to achieve this goal. Our observation suggests that, electroporation of any internal organelle is highly dependent on its shape and relative location inside the cell besides external excitation parameters. Moreover, the enclosing cell morphology and orientation plays a significant role in supra-EP behavior of any cell. In our study, we have validated that irregularity or protrusion on a cell surface not only impact pore formation on the

cell membrane but also manipulate the internally induced electric field to electroporate internal organelles as well.

The findings of our study however contradicts the conclusion drawn in [126]. Their experimental results along with model findings proposes that irregular cell morphology does not affect the supra-EP characteristics. The discrepancy arises as they incorporated an ns-PEF pulse train to induce cell death by destroying the nucleus membrane. In their study, they have incorporated the pore radius evolution along with pore density and hence their major focus was if a combination of ns-PEF and μs-PEF can introduce pore radius evolution beyond repair (i.e. irreversible electroporation on the nucleus membrane). Moreover, while they concentrated on the pore density distribution and maximum after the end of the excitation pulse, we focus our observation on the progression of pore density at the beginning of the excitation. On other hand, although we observe difference in temporal distribution on the nucleus membrane of the cells, the difference is in nanoseconds range. Also, the numbers of average pore density although different, but again has the same exponential term ($\sim 10^{16} \, 1/m^2$). In other words, even though their conclusion contradicts ours, our approach and investigation to the electroporation phenomenon remains accurate and in agreement with each other.

CHAPTER 5

5   3D COMPUTATIONAL STUDY OF LOCALIZED

ELECTROPORATION WITH REALISTIC CELL MORPHOLOGY

5.1   Introduction

In previous section, we have demonstrated the successful implementation of non-linear membrane model to imitate the pore formation dynamics in supra-EP studies for 2D cross-sectional cell surface. The emphasis of this study is to computationally analyze the effect of the actual three-dimensional (3D) cell shape on its supra-electroporation behavior. The computational experiments are conducted using a similar multi-physics solver that combines a quasi-static electromagnetic solver with a well-established non-linear membrane model to account for the changes in membrane conductivity due to the formation of nanopores, except the solution domain is in 3D space. The spatial and temporal variations of the nanopores introduced to the nucleus membrane are quantified for realistic cell shape, indicating the importance of the consideration of the actual 3D cell morphology in supra-electroporation studies.

Besides morphological features, variation in excitation protocols such as uniform or non-uniform electric field excitation also effects the supra-electroporation characteristics. Uniform electric field excitation results in bulk electroporation (BEP) leading to small control over selective electroporation of specific regions of the cell. Although, bulk electroporation (BEP) provides high throughput in gene therapy, drug screening, cell reprogramming, and wound healing applications and requires simplest of setup, it cannot ensure negligible cell damage due to the cells being exposed to high intensity electric fields. Microfluidic

electroporation (MEP) can overcome this limitation by exciting a single cell with low voltage in a confined region to ensure cell viability but fails to incorporate dosage control [136]. Localized electroporation using nanochannel, nonostraw or nanopipette (NEP) overcome these limitations by exposing a small area of the cell to the electroporating field, thereby gain high cell viability, uniform delivery, and dosage control [123]. In the second phase of this section, we will investigate numerically such a setup with realistic three-dimensional cell shapes to design an optimization problem for the electrical excitation to ensure maximum transfection efficiency.

5.2   Methodology

The proposed computational study is going to be performed in COMSOL multiphysics domain with electric current physics to solve the Laplace equation to get the electric field distribution and a weak form PDE solver to account for the non-linear membrane model based on asymptotic Smoluchowski equation (5.1) [134]. To investigate the realistic cell shape, we are incorporating most advanced cell morphology database developed by National Institute of Standards and Technology (NIST) [28]. Application of an external electrical excitation ($\vec{E}$) forces the transmembrane voltage of plasma membrane (PM) to lift above electroporation threshold (Φ_{ep}) by forming numerous conducting pores (N_{ijk}) over the surface of the membrane. The rate of change in pore density over the surface of the PM follows Smoluchowski equation (5.1), which also contributes to the change in membrane conductivity (5.2). As a result, the physics of solving the electric field distribution inside and around the cell using Laplace equation (5.3) must incorporate the change in membrane material property, which is source of nonlinearity in the model.

$$\frac{dN_{ijk}(t)}{dt} = \alpha e^{\left(\frac{\Delta\Phi_m^{ijk}}{\Phi_{ep}}\right)^2} \left(1 - \frac{N_{ijk}(t)}{N_0 e^{q\left(\frac{\Delta\Phi_m^{ijk}}{\Phi_{ep}}\right)^2}}\right), \tag{5.1}$$

$$\chi_m^{ijk}(t) = \chi_{m0} + N_{ijk}(t)\chi_p * \pi\Gamma_p^2 * K, \tag{5.2}$$

$$-\nabla(\chi\nabla\Phi) - \epsilon_0\epsilon_r\nabla\left(\frac{\delta}{\delta t}(\nabla\Phi)\right) = 0. \tag{5.3}$$

Here, N_{ijk} is the number of pores formed on the membrane with voltage $\Delta\Phi_m$, which alters the membrane conductivity, hence the non-linearity in the model. N_0 is the equilibrium pore density of cell and nucleus PM, and Γ_p and χ_p are the pore radius and pore conductivity, respectively. Related parameters for this model are adopted from section 4. The solution of (5.1) was obtained by using the Electric Current (Time Domain) solver and a weak form PDE solver was used to solve (5.2). We then coupled both the solutions in Multiphysics domain to obtain the spatiotemporal distribution of the pore density on the cell and the nucleus PM.

For the uniform electric field excitation, we have used a 16 kV/cm pulse ($\vec{E}$) with 71 ns pulse width, that includes a 6 ns rise time and 10 ns fall time as our excitation, to ensure the electric field intensity is high enough to introduce permeability into the nucleus, but still preserves cell viability [79]. For simulating the non-uniform excitation field, we employed a NEP setup that consists of a cylindrical chamber over which the cell is seated. 3D mesh of the desired cell shape (SC) was imported in a circularly distributed nanochannel array, built in COMSOL Multiphysics model builder (Fig. 5.1). The cell was cultured on a 2D substrate (SpunCoat), hence provides a flat distribution [5] and closely resembles the morphology of adherent cells attached on the chip surface of typical NEP systems.
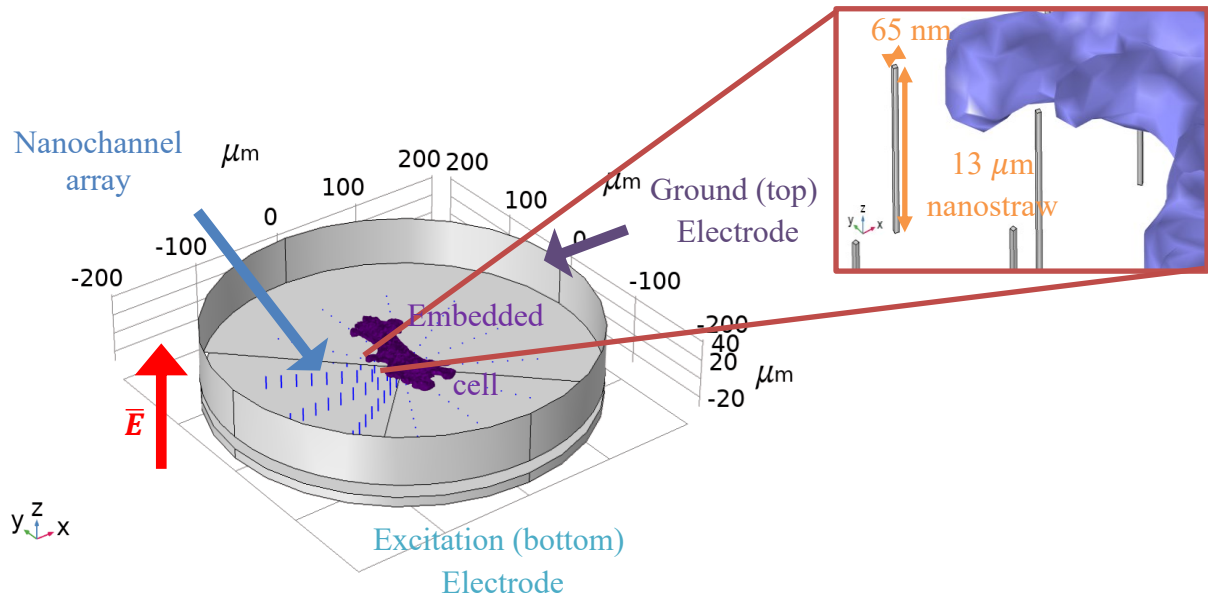
Figure 5.1 Nanochannel setup with realistic 3D cell (blue lines are the uniformly distributed channels distributed on top of the bottom electrode)

5.3   Results and Discussion

5.3.1   Uniform Electrical Excitation

Under the influence of the external electrical excitation, the pore density distribution of cell and nucleus PM at different time stamps is shown in Fig. 5.2. Even though the rise time of the pulse is 6 ns, we see the onset of electroporation at cell PM happens at around 15 ns, depicting its capacitive behavior. Although the cell shape considered herein is almost spherical in shape (MG), but we can still observe asymmetric behavior in the pore density distribution. This observation drives our motivation to include additional variations in cell morphology (from 1D rod-like cells to 2D disk-like cell) as well as explore different modalities of electrical excitations to target specific cell morphologies selectively.
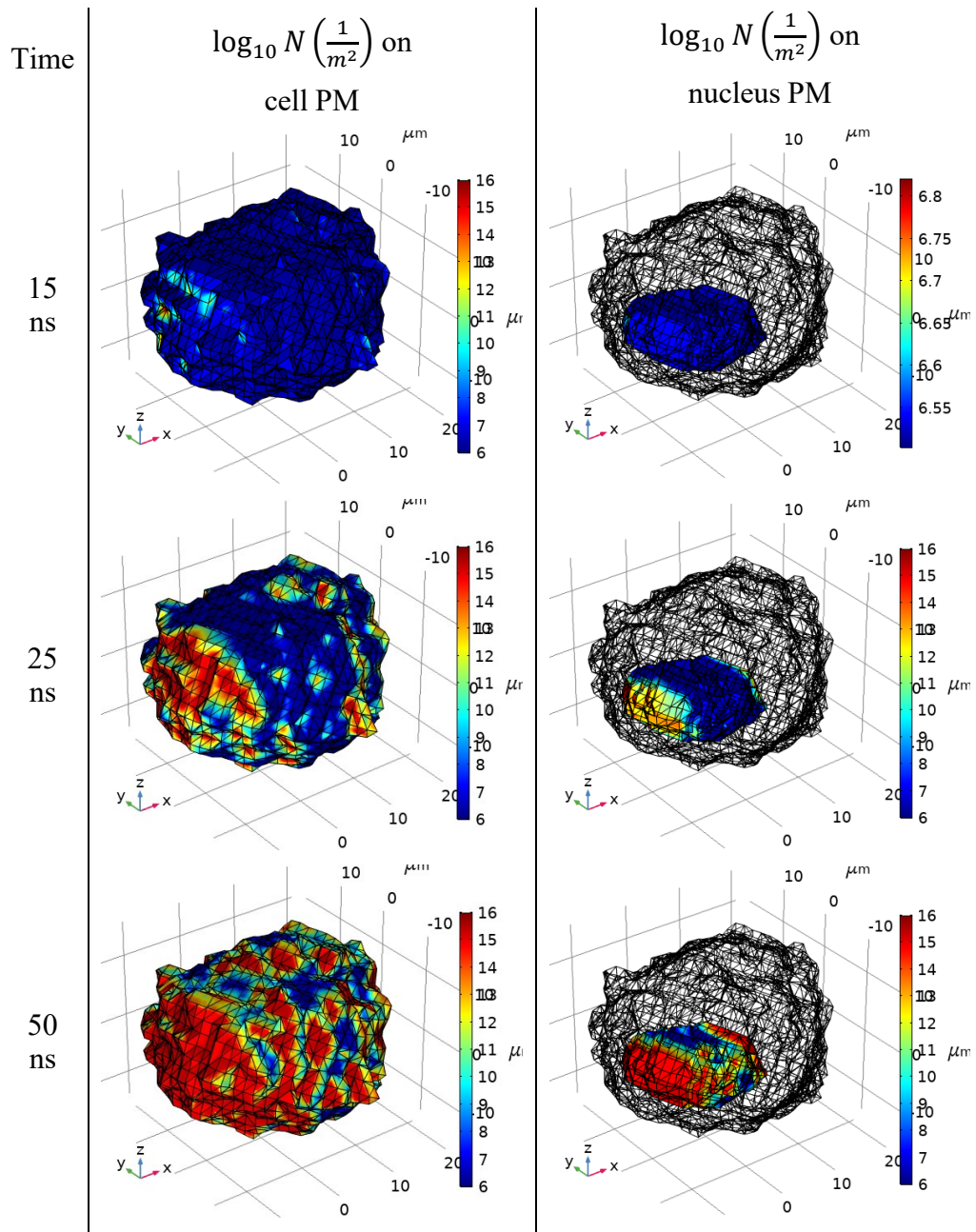
Figure 5.2 3D map of the pore density distribution of Matrigel (MG) at different time instants.
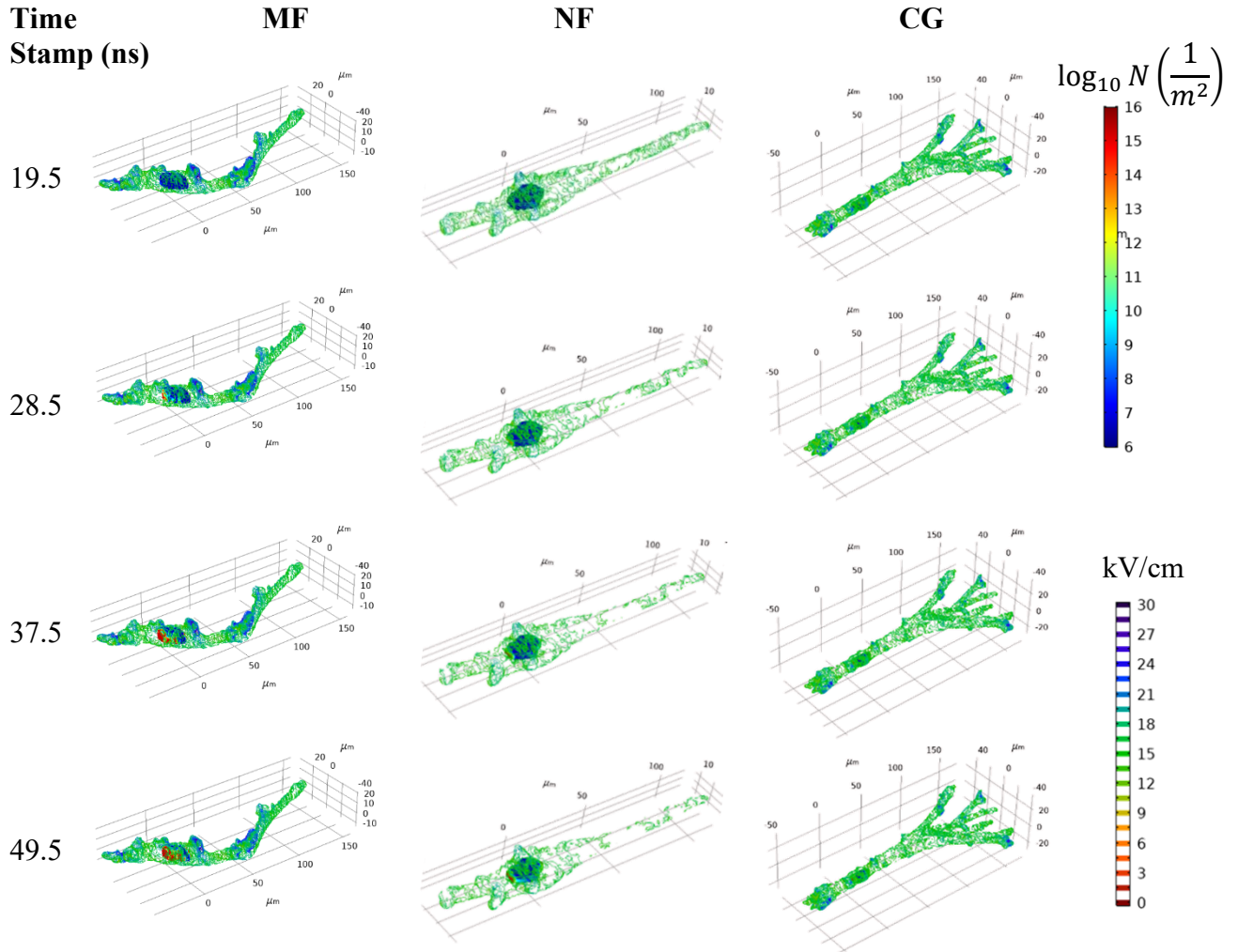
Figure 5.3 Comparison of normal component of the induced electric field (contour plot) and pore density distribution (surface plot) for three different cell shapes at several time stamps

We present the normal component of the induced electric field due to a uniform external excitation along with the pore density distribution at nucleus of three cell morphologies (MF, NF, CG) in Fig. 5.2. The contour plots depicts insignificant difference in induced electric field for different cell shapes and reaching equilibrium at a certain time stamp for all cell shapes. On the same plot, surface distribution of pore density at nucleus of each cell shows the nucleus getting electroporated after a while. Pore formation at nucleus PM of MG cell (Figure 5.2) is much faster compared to other cell shapes. At around 50 ns, almost half of the MG cell nucleus

reaches equilibrium pore density stage. Not as fast as MG cell nucleus, but MF cell also demonstrates an expedited supra-EP behavior in comparison to NF and CG cell shapes.

5.3.2 Non-uniform Electrical Excitation

To investigate the effect of non-uniform excitation, we incorporated the geometry depicted in Fig. 5.1 and a 250 V unit step excitation was used as the source. We then compared the pore density distribution of it with a spheroidal analog under identical excitation. The spheroidal cell was chosen carefully to have same volume as the irregular cell shape. We present the comparison at several time stamps in Fig. 5.4. There exist gaps between the substrate and cell membrane due to the presence of binding proteins that attach the cell cytoskeleton to the culturing medium. The irregular cell morphology introduced in our study had a minimum gap distance of $\approx$ 162 nm from the tip of the nanochannel setup along z-axis.

We recorded the induced electric field strength at the tip of each nanochannel reached 130 kV/cm for a 250 V excitation and maintained 3 kV/cm (considered as a threshold to initiate pore formation [123]) in the ECM until z $\approx$ 1.5 μm far from the tip. Black dots around the cell corresponds to nanochannel location in the xy-plane. While Irregular cell reaches onset of electroporation at 15 ns, the spheroidal cell already encounters relatively higher throughput at a faster rate.

To illustrate a more comprehensive conclusion on the pore density distribution of irregular cell shapes, we present the depth profile (μm) of each cell shape from the tip of the nanochannel at 150 ns after the onset of excitation in Fig. 5.5. Contour plot of the membrane distance from the tip of the nanochannel illustrates the nonuniformity of depth profile along z

113

and its effect on pore formation. As a result, spheroidal cell has a symmetrical pore density distribution unlike irregular cell shape.
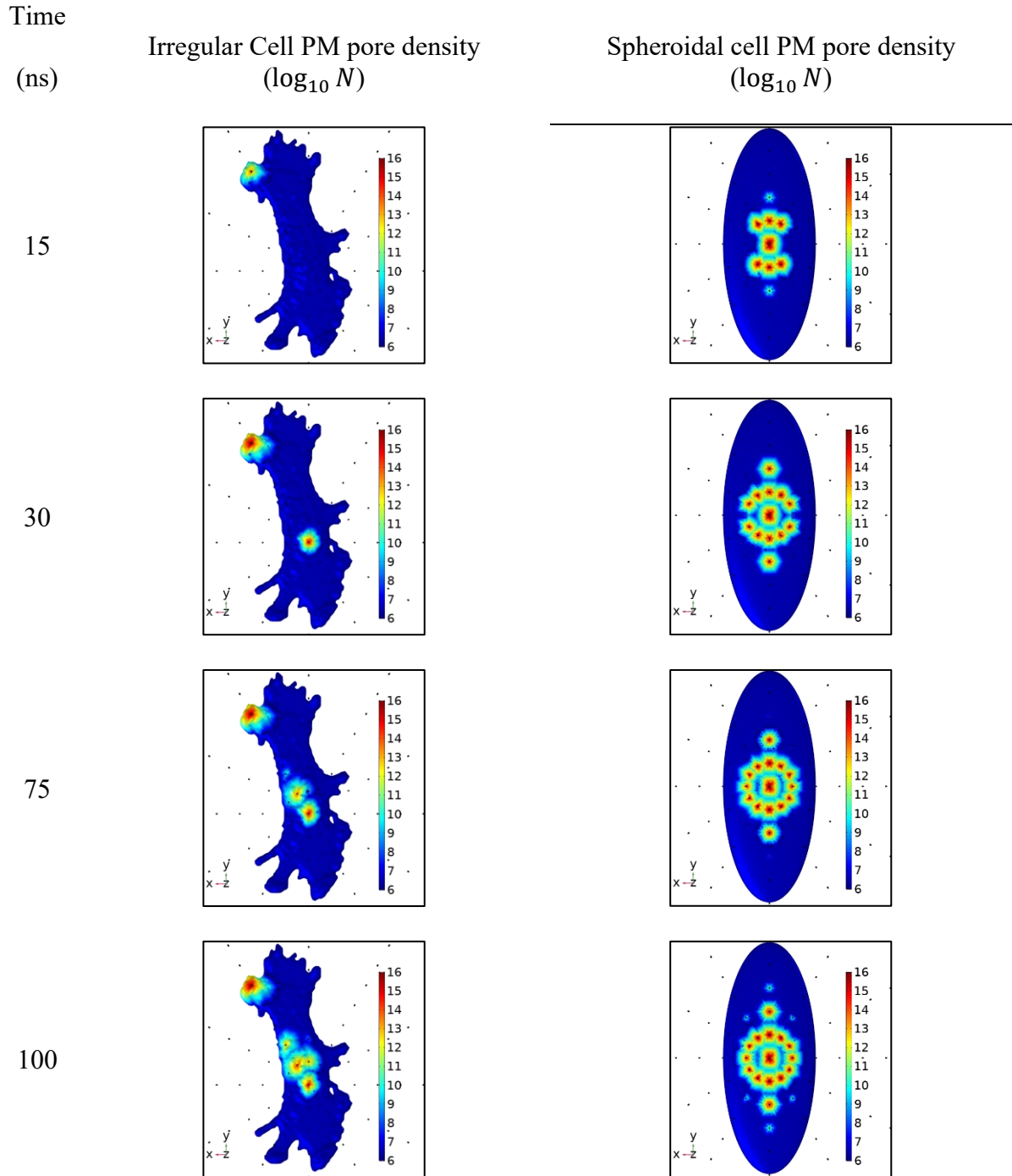
Figure 5.4 Comparison of pore density profile on an irregular cell shape under non-uniform external excitation
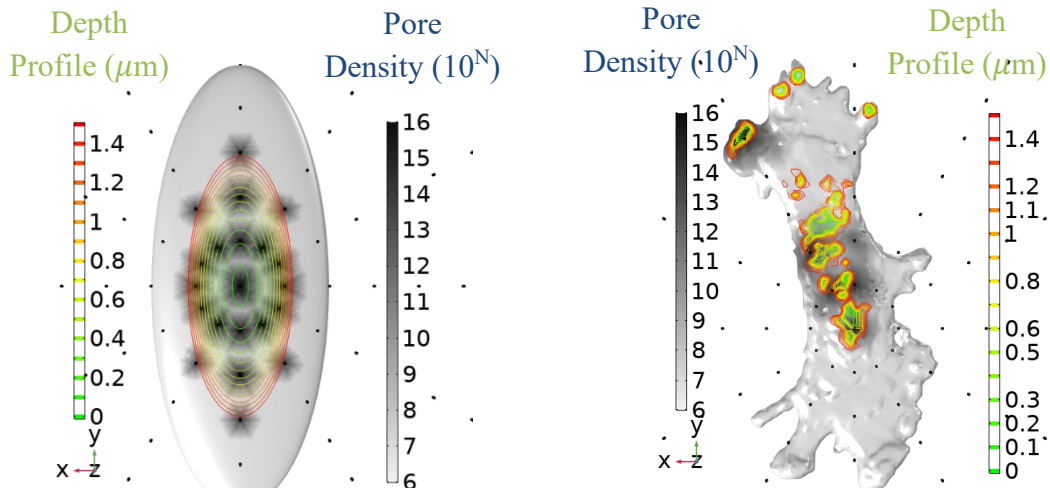
Figure 5.5 Pore density distribution with depth profile from the tip of the nanochannel electrode

This is another cell morphology effect because irregular cell shapes will have variations in height which will effect electroporation rate and hence morphology is a key aspect to quantify electroporation throughput of original cells.

5.4   Conclusion

The above observation signifies the importance of incorporating the actual cell geometry in localized electroporation study. Selective supra-electroporation of cells with specific morphology can be achieved by controlling the time exposure. For practical electroporation studies the nonuniformity in excitation can couple with the variations in the cell morphology e.g. the depth of the cell affect the rate of electroporation. Our study concludes that, besides excitation field and channel gap distance, cell morphology also has a major effect on transfection efficiency in NEP applications.

CHAPTER 6

6   CONCLUSION AND FUTURE RESEARCH

In chapter 2, we analyzed the electrical properties of realistic cell geometries by focusing on the electrostatic electric and magnetic polarizabilities. To incorporate a wide variation in cell morphology, we incorporated a realistic 3D cell database of thousands of stem cells. Realizing the sophisticated nature of the application, we ensured the accuracy of our calculation through extensive validation from three completely different solvers. We found that cellular dimensionality plays a significant role on the behavior of a cell when subject to external electrical stimulus. We also conducted a statistical analysis of the cellular dimensionality to predict the possible response of a cell when cultured in a specific condition. Moreover, our observation solidifies the importance of considering the exact morphology of a cell while designing experiments to characterize cells' electrical behavior and to interpret the experimental outcome. The polarizability values in this work will aid in designing more accurate experiments and a more accurate interpretation of the measurement results, which has the potential to advance the electrical characterization of biological cells.

In chapter 3, we took the findings from our polarizability studies and attempted to link it with the induced transmembrane voltage (ITV) study. While polarizability calculations were done in extreme contrast to predict the dielectric properties of a cell in any medium using Pade approximation, in the ITV study, we modeled the cells as a uniform medium enclosed by another uniform layer of cell membrane of negligible conductivity. We found that the ITV profile is highly dependent on the nonlinear distribution of cell membrane and the degree of nonuniformity in the cell membrane structure influence the amount of charge buildup at certain

116

location of the cell. However, while being randomly oriented, all cell experienced a similar electroporated area considering a hypothetical electroporation threshold value. More interesting observation of the cell morphological effect was observed when we switch the excitation protocol to alternating current. We found the membrane goes through breakdown at a certain frequency, namely the cutoff frequency and this frequency maintains direct correlation with the cell morphology. The shortcoming of this study is, we considered the membrane properties remain unchanged during this breakdown phenomena.

However, in practical case scenario, the membrane goes through simultaneous pore formation, which in turn will change the dielectric properties of it. Hence, in chapter 4, our focus was incorporating a nonlinear membrane model that can simulate the physics of pore formation dynamics. The preliminary study was conducted on 2D cell cross-sections with internal organelles. We computationally demonstrated that by controlling the pulse frequency and strength, the internal organelles' membrane can also be manipulated. A significant finding in this regard was that the pore formation across the internal organelles' membrane is highly dependent on the cell membrane morphology enclosing the internal organelle. Also the relative position of the internal organelle has a prominent effect on how quickly/slowly its' membrane will electroporate. The future scope of this study is to incorporate the variable pore radius and also considering the nonuniform electrical excitation.

Being a computational study, the overall findings of this studies are quantitative and ensured a satisfactory level of accuracy upon validation at different stages. However, the application of the findings is in biological science which is the most critical science in perspective of practical applications. Hence, the ultimate future remains in finding appropriate opportunity to experimentally validate our results. Given the facilities to perform the

experiments in *in-vitro* setup, we can achieve more sophisticated outcome that can employed in several other biomedical applications such as dielectrophoresis, electrotaxis etc. besides electroporation phenomenon.

As the supra-EP studies concentrates on electroporating internal organelles inside the cell, we must also take other internal organelles such as mitochondria, chloroplasts, the endoplasmic reticulum, the Golgi apparatus, and lysosomes besides the nucleus. Even though nucleus is the largest internal organelle of a cell and according to the physics of electroporation, will electroporate faster, other organelles will also go through pore formation under specific condition of the excitation field. In this study, we only considered nucleus out of all the internal organelles of the cells. The future scope of this study remains in incorporating an accurate physical model of other organelles and a thorough investigation of the excitation protocol to selectively electroporate specific internal organelle. We also need to investigate the effect of high intensity electric field on membrane proteins or microorganism that doesn't have any membrane of its own. In these future studies, the findings of our study can guide users can guide potential selective targeting of specific internal organelles based on their location inside the cells and the local internal electric field.

.

REFERENCES

[1] S. Baidya, A. M. Hassan, and M. Zhao, "Computational modeling of transepithelial endogenous electric signals," in *Biological and Medical Aspects of Electromagnetic Fields*, 4th ed., CRC Press, 2018.

[2] J. Hunckler and A. de Mel, "A current affair: electrotherapy in wound healing," *J. Multidiscip. Healthc.*, vol. 10, pp. 179–194, Apr. 2017, doi: 10.2147/JMDH.S127207.

[3] S. Ud-Din and A. Bayat, "Electrical stimulation and cutaneous wound healing: A review of clinical evidence," *Healthcare*, vol. 2, no. 4, Art. no. 4, Dec. 2014, doi: 10.3390/healthcare2040445.

[4] N. Abd Rahman, F. Ibrahim, and B. Yafouz, "Dielectrophoresis for biomedical sciences applications: A review," *Sensors*, vol. 17, no. 3, Art. no. 3, Mar. 2017, doi: 10.3390/s17030449.

[5] L. Rems and D. Miklavčič, "Tutorial: Electroporation of cells in complex materials and tissue," *J. Appl. Phys.*, vol. 119, no. 20, p. 201101, May 2016, doi: 10.1063/1.4949264.

[6] P. Rangamani *et al.*, "Decoding information in cell shape," *Cell*, vol. 154, no. 6, pp. 1356–1369, Sep. 2013, doi: 10.1016/j.cell.2013.08.026.

[7] S. W. K. Chan, K. S. Leung, and W. S. Felix Wong, "An expert system for the detection of cervical cancer cells using knowledge-based image analyzer," *Artif. Intell. Med.*, vol. 8, no. 1, pp. 67–90, Feb. 1996, doi: 10.1016/0933-3657(95)00021-6.

[8] T.-Q. Xie, M. L. Zeidel, and Y.-T. Pan, "Detection of tumorigenesis in urinary bladder with optical coherence tomography: optical characterization of morphological changes," *Opt. Express*, vol. 10, no. 24, pp. 1431–1443, Dec. 2002, doi: 10.1364/OE.10.001431.

[9] G. A. Losa and C. Castelli, "Nuclear patterns of human breast cancer cells during apoptosis: characterisation by fractal dimension and co-occurrence matrix statistics," *Cell Tissue Res.*, vol. 322, no. 2, pp. 257–267, Nov. 2005, doi: 10.1007/s00441-005-0030-2.

[10] M. Colombi, L. Moro, N. Zoppi, and S. Barlati, "Quantitative evaluation of mRNAs by *in-situ* hybridization and image analysis: principles and applications," *DNA Cell Biol.*, vol. 12, no. 7, pp. 629–636, Sep. 1993, doi: 10.1089/dna.1993.12.629.

[11] P. A. Melrose, C. Pickel, H. S. Cheramie, W. G. Henk, M. A. Littlefield-Chabaud, and D. D. French, "Distribution and morphology of immunoreactive gonadotropin-releasing

hormone (GnRH) neurons in the basal forebrain of ponies," *J. Comp. Neurol.*, vol. 339, no. 2, pp. 269–287, 1994, doi: 10.1002/cne.903390207.

[12] M. F. Villa and F. R. Amthor, "Automating the quantitative analysis of 2-D neural dendritic trees," *J. Neurosci. Methods*, vol. 56, no. 1, pp. 77–88, Jan. 1995, doi: 10.1016/0165-0270(94)00109-T.

[13] M. Masseroli, A. Bollea, and G. Forloni, "Quantitative morphology and shape classification of neurons by computerized image analysis," *Comput. Methods Programs Biomed.*, vol. 41, no. 2, pp. 89–99, Dec. 1993, doi: 10.1016/0169-2607(93)90068-V.

[14] K. A. Giuliano, "Dissecting the individuality of cancer cells: the morphological and molecular dynamics of single human glioma cells," *Cell Motil.*, vol. 35, no. 3, pp. 237–253, 1996, doi: 10.1002/(SICI)1097-0169(1996)35:3<237::AID-CM6>3.0.CO;2-5.

[15] C. Broglio, J. Dufer, P. Joly, Y. Carpentier, and A. Desplaces, "Quantitative morphological assessment of erythroblastic differentiation induced, *in vitro*, in human K562 leukemic cells," *Anal. Cell. Pathol.*, vol. 5, no. 3, pp. 135–146, May 1993.

[16] E. C. Jensen, "Overview of live-cell imaging: requirements and methods used," *Anat. Rec.*, vol. 296, no. 1, pp. 1–8, 2013, doi: 10.1002/ar.22554.

[17] E. Cukierman, R. Pankov, D. R. Stevens, and K. M. Yamada, "Taking cell-matrix adhesions to the third dimension," *Science*, vol. 294, no. 5547, pp. 1708–1712, Nov. 2001, doi: 10.1126/science.1064829.

[18] S. Liao *et al.*, "Biomimetic nanocomposites to control osteogenic differentiation of human mesenchymal stem cells," *Adv. Healthc. Mater.*, vol. 3, no. 5, pp. 737–751, 2014, doi: 10.1002/adhm.201300207.

[19] S. J. Florczyk, M. Leung, Z. Li, J. I. Huang, R. A. Hopper, and M. Zhang, "Evaluation of three-dimensional porous chitosan–alginate scaffolds in rat calvarial defects for bone regeneration applications," *J. Biomed. Mater. Res. A*, vol. 101, no. 10, pp. 2974–2983, 2013, doi: 10.1002/jbm.a.34593.

[20] K. Chatterjee *et al.*, "The effect of 3D hydrogel scaffold modulus on osteoblast differentiation and mineralization revealed by combinatorial screening," *Biomaterials*, vol. 31, no. 19, pp. 5051–5062, Jul. 2010, doi: 10.1016/j.biomaterials.2010.03.024.

[21] D. Chen *et al.*, "Machine learning based methodology to identify cell shape phenotypes associated with microenvironmental cues," *Biomaterials*, vol. 104, pp. 104–118, Oct. 2016, doi: 10.1016/j.biomaterials.2016.06.040.

[22] R. McBeath, D. M. Pirone, C. M. Nelson, K. Bhadriraju, and C. S. Chen, "Cell shape, cytoskeletal tension, and RhoA regulate stem cell lineage commitment," *Dev. Cell*, vol. 6, no. 4, pp. 483–495, Apr. 2004, doi: 10.1016/S1534-5807(04)00075-9.

[23] K. A. Kilian, B. Bugarija, B. T. Lahn, and M. Mrksich, "Geometric cues for directing the differentiation of mesenchymal stem cells," *Proc. Natl. Acad. Sci.*, vol. 107, no. 11, pp. 4872–4877, Mar. 2010.

[24] C. S. Chen, M. Mrksich, S. Huang, G. M. Whitesides, and D. E. Ingber, "Geometric control of cell life and death," *Science*, vol. 276, no. 5317, pp. 1425–1428, May 1997, doi: 10.1126/science.276.5317.1425.

[25] S. J. Florczyk *et al.*, "A bioinformatics 3D cellular morphotyping strategy for assessing biomaterial scaffold niches," *ACS Biomater. Sci. Eng.*, vol. 3, no. 10, pp. 2302–2313, Oct. 2017, doi: 10.1021/acsbiomaterials.7b00473.

[26] P. Bajcsy, M. Simon, S. J. Florczyk, C. G. Simon, D. Juba, and M. C. Brady, "A method for the evaluation of thousands of automated 3D stem cell segmentations," *J. Microsc.*, vol. 260, no. 3, pp. 363–376, 2015, doi: 10.1111/jmi.12303.

[27] "Mass Viewer." https://isg.nist.gov/deepzoomweb/stemcells3d/index.html

[28] "NIST computational science in metrology." https://isg.nist.gov/deepzoomweb/fileBrowsing/3D (accessed May 11, 2020).

[29] B. A. P. Betancourt *et al.*, "Effect of the scaffold microenvironment on cell polarizability and capacitance determined by probabilistic computations," *Biomed. Mater.*, vol. 13, no. 2, p. 025012, Jan. 2018, doi: 10.1088/1748-605X/aa9650.

[30] T. M. Farooque, C. H. Camp, C. K. Tison, G. Kumar, S. H. Parekh, and C. G. Simon, "Measuring stem cell dimensionality in tissue scaffolds," *Biomaterials*, vol. 35, no. 9, pp. 2558–2567, Mar. 2014, doi: 10.1016/j.biomaterials.2013.12.092.

[31] D. Juba, D. J. Audus, M. Mascagni, J. F. Douglas, and W. Keyrouz, "ZENO: Software for calculating hydrodynamic, electrical, and shape properties of polymer and particle suspensions," *J. Res. Natl. Inst. Stand. Technol.*, vol. 122, p. 20, Mar. 2017, doi: 10.6028/jres.122.020.

[32] M. L. Mansfield, J. F. Douglas, and E. J. Garboczi, "Intrinsic viscosity and the electrical polarizability of arbitrarily shaped objects," *Phys. Rev. E*, vol. 64, no. 6, p. 061401, Nov. 2001, doi: 10.1103/PhysRevE.64.061401.

[33] K. Asami, "Low-frequency dielectric dispersion of bacterial cell suspensions," *Colloids Surf. B Biointerfaces*, vol. 119, pp. 1–5, Jul. 2014, doi: 10.1016/j.colsurfb.2014.04.014.

[34] A. Di Biasio and C. Cametti, "Polarizability of spherical biological cells in the presence of localized surface charge distributions at the membrane interfaces," *Phys. Rev. E*, vol. 82, no. 2, p. 021917, Aug. 2010, doi: 10.1103/PhysRevE.82.021917.

[35] A. D. Biasio, L. Ambrosone, and C. Cametti, "Electrical polarizability of differently shaped dielectric objects in the presence of localized interfacial charge distribution: a unifying scenario," *J. Phys. Appl. Phys.*, vol. 46, no. 5, p. 055305, Jan. 2013, doi: 10.1088/0022-3727/46/5/055305.

[36] J. L. Sebastián, S. Muñoz, M. Sancho, and G. Álvarez, "Polarizability of shelled particles of arbitrary shape in lossy media with an application to hematic cells," *Phys. Rev. E*, vol. 78, no. 5, p. 051905, Nov. 2008, doi: 10.1103/PhysRevE.78.051905.

[37] E. Prodan, C. Prodan, and J. H. Miller, "The dielectric response of spherical live cells in suspension: an analytic solution," *Biophys. J.*, vol. 95, no. 9, pp. 4174–4182, Nov. 2008, doi: 10.1529/biophysj.108.137042.

[38] J. L. Sebastián, S. Muñoz, M. Sancho, G. Martínez, and K. V. I. S. Kaler, "Polarizability of red blood cells with an anisotropic membrane," *Phys. Rev. E*, vol. 81, no. 2, p. 022901, Feb. 2010, doi: 10.1103/PhysRevE.81.022901.

[39] A. Sihvola, P. Yla-Oijala, S. Jarvenpaa, and J. Avelin, "Polarizabilities of platonic solids," *IEEE Trans. Antennas Propag.*, vol. 52, no. 9, pp. 2226–2233, Sep. 2004, doi: 10.1109/TAP.2004.834081.

[40] J. D. Jackson, *Classical electrodynamics*, 3rd ed. New York, NY, USA: John Wiley & Sons.

[41] A. H. Sihvola, *Electromagnetic mixing formulas and applications*. IET, 1999.

[42] F. Vargas–Lara, A. M. Hassan, E. J. Garboczi, and J. F. Douglas, "Intrinsic conductivity of carbon nanotubes and graphene sheets having a realistic geometry," *J. Chem. Phys.*, vol. 143, no. 20, p. 204902, Nov. 2015, doi: 10.1063/1.4935970.

[43] *COMSOL multiphysics*. Stockholm, Sweden: COMSOL AB. [Online]. Available: www.comsol.com

[44] *COMSOL multiphysics AC/DC module user's guide*. Stockholm, Sweden: COMSOL AB.

[45] P. Cignoni, M. Callieri, M. Corsini, M. Dellepiane, F. Ganovelli, and G. Ranzuglia, "MeshLab: an Open-Source Mesh Processing Tool," p. 8.

[46] M. T. H. Reid and S. G. Johnson, "Efficient computation of power, force, and torque in BEM scattering calculations," *IEEE Trans. Antennas Propag.*, vol. 63, no. 8, pp. 3588–3598, Aug. 2015, doi: 10.1109/TAP.2015.2438393.

[47] C. Geuzaine and J.-F. Remacle, "Gmsh: A 3-D finite element mesh generator with built-in pre- and post-processing facilities," *Int. J. Numer. Methods Eng.*, vol. 79, no. 11, pp. 1309–1331, 2009, doi: 10.1002/nme.2579.

[48] E. J. Garboczi, "Finite element and finite difference programs for computing the linear electric and elastic properties of digital images of random materials," Dec. 1998, Accessed: Jul. 01, 2021. [Online]. Available: https://www.nist.gov/publications/finite-element-and-finite-difference-programs-computing-linear-electric-and-elastic

[49] E. J. Garboczi and J. F. Douglas, "Intrinsic conductivity of objects having arbitrary shape and conductivity," *Phys. Rev. E*, vol. 53, no. 6, pp. 6169–6180, Jun. 1996, doi: 10.1103/PhysRevE.53.6169.

[50] E. J. Garboczi, "The influence of particle shape on the results of the electrical sensing zone method as explained by the particle intrinsic conductivity," *Powder Technol.*, vol. 322, pp. 32–40, Dec. 2017, doi: 10.1016/j.powtec.2017.08.057.

[51] A. N. Chiaramonti, J. D. Goguen, and E. J. Garboczi, "Quantifying the 3-dimensional shape of lunar regolith particles using X-ray computed tomography and scanning electron microscopy at sub-λ resolution," *Microsc. Microanal. Off. J. Microsc. Soc. Am. Microbeam Anal. Soc. Microsc. Soc. Can.*, vol. 23, no. Suppl 1, pp. 2194–2195, Jul. 2017, doi: 10.1017/S1431927617011631.

[52] D. B. Davidson, *Computational electromagnetics for RF and microwave engineering*, 2nd ed. Cambridge, New York: Cambridge University Press, 2010.

[53] J. F. Douglas and E. J. Garboczi, "Intrinsic viscosity and the polarizability of particles having a wide range of shapes," *Adv. Chem. Phys.*, vol. 91, pp. 85–154, 1995.

[54] D. J. Audus, A. M. Hassan, E. J. Garboczi, and J. F. Douglas, "Interplay of particle shape and suspension properties: a study of cube-like particles," *Soft Matter*, vol. 11, no. 17, pp. 3360–3366, Apr. 2015, doi: 10.1039/C4SM02869D.

[55] M. L. Mansfield and J. F. Douglas, "Improved path integration method for estimating the intrinsic viscosity of arbitrarily shaped particles," *Phys. Rev. E*, vol. 78, no. 4, p. 046712, Oct. 2008, doi: 10.1103/PhysRevE.78.046712.

[56] L. G. Khachiyan, "Rounding of polytopes in the real number model of computation," *Math. Oper. Res.*, vol. 21, no. 2, pp. 307–320, May 1996, doi: 10.1287/moor.21.2.307.

[57] N. Moshtagh, *Minimum volume enclosing ellipsoids*.

[58] R. Pethig, "Review Article—Dielectrophoresis: status of the theory, technology, and applications," *Biomicrofluidics*, vol. 4, no. 2, p. 022811, Jun. 2010, doi: 10.1063/1.3456626.

[59] F. F. Becker, X. B. Wang, Y. Huang, R. Pethig, J. Vykoukal, and P. R. Gascoyne, "Separation of human breast cancer cells from blood by differential dielectric affinity," *Proc. Natl. Acad. Sci.*, vol. 92, no. 3, pp. 860–864, Jan. 1995.

[60] J. Regtmeier, R. Eichhorn, L. Bogunovic, A. Ros, and D. Anselmetti, "Dielectrophoretic trapping and polarizability of DNA: the role of spatial conformation," *Anal. Chem.*, vol. 82, no. 17, pp. 7141–7149, Sep. 2010, doi: 10.1021/ac1005475.

[61] A. Ramos, H. Morgan, N. G. Green, and A. Castellanos, "Ac electrokinetics: a review of forces in microelectrode structures," *J. Phys. Appl. Phys.*, vol. 31, no. 18, pp. 2338–2353, Sep. 1998, doi: 10.1088/0022-3727/31/18/021.

[62] P. R. C. Gascoyne and J. Vykoukal, "Particle separation by dielectrophoresis," *Electrophoresis*, vol. 23, no. 13, pp. 1973–1983, Jul. 2002, doi: 10.1002/1522-2683(200207)23:13<1973::AID-ELPS1973>3.0.CO;2-1.

[63] H. Morgan, M. P. Hughes, and N. G. Green, "Separation of submicron bioparticles by dielectrophoresis," *Biophys. J.*, vol. 77, no. 1, pp. 516–525, Jul. 1999, doi: 10.1016/S0006-3495(99)76908-0.

[64] P. R. C. Gascoyne, J. Noshari, T. J. Anderson, and F. F. Becker, "Isolation of rare cells from cell mixtures by dielectrophoresis," *ELECTROPHORESIS*, vol. 30, no. 8, pp. 1388–1398, 2009, doi: 10.1002/elps.200800373.

[65] B. Valič *et al.*, "Effect of electric field induced transmembrane potential on spheroidal cells: theory and experiment," *Eur. Biophys. J.*, vol. 32, no. 6, pp. 519–528, Oct. 2003, doi: 10.1007/s00249-003-0296-9.

[66] T. Kotnik, P. Kramar, G. Pucihar, D. Miklavcic, and M. Tarek, "Cell membrane electroporation- part 1: the phenomenon," *IEEE Electr. Insul. Mag.*, vol. 28, no. 5, pp. 14–23, Sep. 2012, doi: 10.1109/MEI.2012.6268438.

[67] B. Ghanbarian and H. Daigle, "Permeability in two-component porous media: effective-medium approximation compared with Lattice-Boltzmann simulations," *Vadose Zone J.*, vol. 15, no. 2, Feb. 2016, doi: 10.2136/vzj2015.05.0071.

[68] W. Stein, *The movement of molecules across cell membranes*, vol. 6. Elsevier, 2012.

[69] J. Lombard, "Once upon a time the cell membranes: 175 years of cell boundary research," *Biol. Direct*, vol. 9, no. 1, p. 32, Dec. 2014, doi: 10.1186/s13062-014-0032-7.

[70] U. Zimmermann, "Electric field-mediated fusion and related electrical phenomena," *Biochim. Biophys. Acta BBA - Rev. Biomembr.*, vol. 694, no. 3, pp. 227–277, Nov. 1982, doi: 10.1016/0304-4157(82)90007-7.

[71] E. Tekle, R. D. Astumian, and P. B. Chock, "Electro-permeabilization of cell membranes: Effect of the resting membrane potential," *Biochem. Biophys. Res. Commun.*, vol. 172, no. 1, pp. 282–287, Oct. 1990, doi: 10.1016/S0006-291X(05)80206-2.

[72] J. Teissié and M. P. Rols, "An experimental evaluation of the critical potential difference inducing cell membrane electropermeabilization," *Biophys. J.*, vol. 65, no. 1, pp. 409–413, Jul. 1993, doi: 10.1016/S0006-3495(93)81052-X.

[73] J.-M. Escoffre, D. S. Dean, M. Hubert, M.-P. Rols, and C. Favard, "Membrane perturbation by an external electric field: a mechanism to permit molecular uptake," *Eur. Biophys. J.*, vol. 36, no. 8, p. 973, Jun. 2007, doi: 10.1007/s00249-007-0194-7.

[74] L. Delemotte, F. Dehez, W. Treptow, and M. Tarek, "Modeling membranes under a transmembrane potential," *J. Phys. Chem. B*, vol. 112, no. 18, pp. 5547–5550, May 2008, doi: 10.1021/jp710846y.

[75] M. Wang, O. Orwar, J. Olofsson, and S. G. Weber, "Single-cell electroporation," *Anal. Bioanal. Chem.*, vol. 397, no. 8, pp. 3235–3248, Aug. 2010, doi: 10.1007/s00216-010-3744-2.

[76] R. Stampfli, "Reversible electrical breakdown of the excitable membrane of a Ranvier node," *Acad Bras. Ciens*, vol. 30, pp. 57–63, 1958.

[77] G. Sersa, D. Miklavcic, M. Cemazar, Z. Rudolf, G. Pucihar, and M. Snoj, "Electrochemotherapy in treatment of tumours," *Eur. J. Surg. Oncol. EJSO*, vol. 34, no. 2, pp. 232–240, Feb. 2008, doi: 10.1016/j.ejso.2007.05.016.

[78] F. André and L. M. Mir, "DNA electrotransfer: its principles and an updated review of its therapeutic applications," *Gene Ther.*, vol. 11, no. S1, pp. S33–S42, Sep. 2004, doi: 10.1038/sj.gt.3302367.

[79] J. C. Weaver, K. C. Smith, A. T. Esser, R. S. Son, and T. R. Gowrishankar, "A brief overview of electroporation pulse strength-duration space: a region where additional intracellular effects are expected," *Bioelectrochemistry Amst. Neth.*, vol. 87, pp. 236–243, Oct. 2012, doi: 10.1016/j.bioelechem.2012.02.007.

[80] E. W. Lee, S. Thai, and S. T. Kee, "Irreversible Electroporation: A novel image-guided cancer therapy," *Gut Liver*, vol. 4, no. Suppl 1, pp. S99–S104, Sep. 2010, doi: 10.5009/gnl.2010.4.S1.S99.

[81] I. Goswami *et al.*, "Irreversible electroporation inhibits pro-cancer inflammatory signaling in triple negative breast cancer cells," *Bioelectrochemistry*, vol. 113, pp. 42–50, Feb. 2017, doi: 10.1016/j.bioelechem.2016.09.003.

[82] C. B. Arena *et al.*, "High-frequency irreversible electroporation (H-FIRE) for non-thermal ablation without muscle contraction," *Biomed. Eng. OnLine*, vol. 10, no. 1, p. 102, Nov. 2011, doi: 10.1186/1475-925X-10-102.

[83] A. H. Ruarus *et al.*, "Percutaneous irreversible electroporation in locally advanced and recurrent pancreatic cancer (PANFIRE-2): a multicenter, prospective, single-arm, phase II study," *Radiology*, vol. 294, no. 1, pp. 212–220, Nov. 2019, doi: 10.1148/radiol.2019191109.

[84] C. He, J. Wang, S. Sun, Y. Zhang, and S. Li, "Immunomodulatory effect after irreversible electroporation in patients with locally advanced pancreatic cancer," *Journal of Oncology*, May 12, 2019. https://www.hindawi.com/journals/jo/2019/9346017/ (accessed Dec. 24, 2020).

[85] R. V. Davalos, L. M. Mir, and B. Rubinsky, "Tissue ablation with irreversible electroporation," *Ann. Biomed. Eng.*, vol. 33, no. 2, p. 223, Feb. 2005, doi: 10.1007/s10439-005-8981-8.

[86] D. Miklavčič, D. Šemrov, H. Mekid, and L. M. Mir, "A validated model of in vivo electric field distribution in tissues for electrochemotherapy and for DNA electrotransfer for gene therapy," *Biochim. Biophys. Acta BBA - Gen. Subj.*, vol. 1523, no. 1, pp. 73–83, Sep. 2000, doi: 10.1016/S0304-4165(00)00101-X.

[87] I. Zudans, A. Agarwal, O. Orwar, and S. G. Weber, "Numerical calculations of single-cell electroporation with an electrolyte-filled capillary," *Biophys. J.*, vol. 92, no. 10, pp. 3696–3705, May 2007, doi: 10.1529/biophysj.106.097683.

[88] G. Pucihar, T. Kotnik, B. Valič, and D. Miklavčič, "Numerical determination of transmembrane voltage induced on irregularly shaped cells," *Ann. Biomed. Eng.*, vol. 34, no. 4, p. 642, Mar. 2006, doi: 10.1007/s10439-005-9076-2.

[89] G. Pucihar, D. Miklavcic, and T. Kotnik, "A time-dependent numerical model of transmembrane voltage inducement and electroporation of irregularly shaped cells," *IEEE Trans. Biomed. Eng.*, vol. 56, no. 5, pp. 1491–1501, May 2009, doi: 10.1109/TBME.2009.2014244.

[90] D. Rauly, M. Vindret, E. Chamberod, J. M. F. Martins, and P. Xavier, "Distribution of AC electric field-induced transmembrane voltage in Escherichia coli cell wall layers," *Bioelectromagnetics*, vol. 41, no. 4, pp. 279–288, 2020, doi: https://doi.org/10.1002/bem.22261.

[91] S. Sherif, Y. H. Ghallab, and Y. Ismail, "Analysis of the deformation in red blood cells based on the transmembrane voltage potential and the pore density," in *2019 Novel Intelligent and Leading Emerging Sciences Conference (NILES)*, Oct. 2019, vol. 1, pp. 63–66. doi: 10.1109/NILES.2019.8909298.

[92] T. R. Gowrishankar and J. C. Weaver, "An approach to electrical modeling of single and multiple cells," *Proc. Natl. Acad. Sci.*, vol. 100, no. 6, pp. 3203–3208, Mar. 2003, doi: 10.1073/pnas.0636434100.

[93] T. Kotnik, G. Pucihar, and D. Miklavčič, "Induced transmembrane voltage and its correlation with electroporation-mediated molecular transport," *J. Membr. Biol.*, vol. 236, no. 1, pp. 3–13, Jul. 2010, doi: 10.1007/s00232-010-9279-9.

[94] P. Bajcsy and C. Simon, "1000+ z-stack experiment." National Institute of Standards and Technology, 2017. doi: 10.18434/M3ZP4Q.

[95] S. Baidya, A. M. Hassan, W. Al-Shaikhli, B. A. P. Betancourt, J. F. Douglas, and E. J. Garboczi, "Analysis of different computational techniques for calculating the polarizability tensors of stem cells with realistic three-dimensional morphologies," *IEEE Trans. Biomed. Eng.*, pp. 1–1, 2018, doi: 10.1109/TBME.2018.2876145.

[96] H. Fricke, "The electric permittivity of a dilute suspension of membrane-covered ellipsoids," *J. Appl. Phys.*, vol. 24, no. 5, pp. 644–646, May 1953, doi: 10.1063/1.1721343.

[97] H. P. Schwan, "Electrical properties of tissue and cell suspensions," in *Advances in Biological and Medical Physics*, vol. 5, J. H. Lawrence and C. A. Tobias, Eds. Elsevier, 1957, pp. 147–209. doi: 10.1016/B978-1-4832-3111-2.50008-0.

[98] J. Bernhardt and H. Pauly, "On the generation of potential differences across the membranes of ellipsoidal cells in an alternating electrical field," *Biophysik*, vol. 10, no. 1, pp. 89–98, Mar. 1973, doi: 10.1007/BF01189915.

[99] T. Kotnik and D. Miklavčič, "Analytical description of transmembrane voltage induced by electric fields on spheroidal cells," *Biophys. J.*, vol. 79, no. 2, pp. 670–679, Aug. 2000, doi: 10.1016/S0006-3495(00)76325-9.

[100] J. Gimsa and D. Wachner, "Analytical description of the transmembrane voltage induced on arbitrarily oriented ellipsoidal and cylindrical cells," *Biophys. J.*, vol. 81, no. 4, pp. 1888–1896, Oct. 2001, doi: 10.1016/S0006-3495(01)75840-7.

[101] K. Maswiwat, D. Wachner, R. Warnke, and J. Gimsa, "Simplified equations for the transmembrane potential induced in ellipsoidal cells of rotational symmetry," *J. Phys. Appl. Phys.*, vol. 40, no. 3, p. 914, 2007, doi: 10.1088/0022-3727/40/3/033.

[102] S. A. Akimov, P. E. Volynsky, T. R. Galimzyanov, P. I. Kuzmin, K. V. Pavlov, and O. V. Batishchev, "Pore formation in lipid membrane I: continuous reversible trajectory from intact bilayer through hydrophobic defect to transversal pore," *Sci. Rep.*, vol. 7, no. 1, Art. no. 1, Sep. 2017, doi: 10.1038/s41598-017-12127-7.

[103] H. Leontiadou, A. E. Mark, and S. J. Marrink, "Molecular dynamics simulations of hydrophilic pores in lipid bilayers," *Biophys. J.*, vol. 86, no. 4, pp. 2156–2164, Apr. 2004.

[104] E. Salimi, "Nanosecond pulse electroporation of biological cells: The effect of membrane dielectric relaxation," Apr. 2011, Accessed: May 23, 2020. [Online]. Available: https://mspace.lib.umanitoba.ca/xmlui/handle/1993/4460

[105] C. A. Jordan, E. Neumann, and A. E. Sowers, *Electroporation and electrofusion in cell biology*. Springer Science & Business Media, 2013.

[106] S. Talele, "Dynamic electroporation modelling," Thesis, The University of Waikato, 2009. Accessed: May 25, 2020. [Online]. Available: https://researchcommons.waikato.ac.nz/handle/10289/4417

[107] K. C. Smith and J. C. Weaver, "Transmembrane molecular transport during versus after extremely large, nanosecond electric pulses," *Biochem. Biophys. Res. Commun.*, vol. 412, no. 1, pp. 8–12, Aug. 2011, doi: 10.1016/j.bbrc.2011.06.171.

[108] T. B. Napotnik, Y.-H. Wu, M. A. Gundersen, D. Miklavčič, and P. T. Vernier, "Nanosecond electric pulses cause mitochondrial membrane permeabilization in Jurkat cells," *Bioelectromagnetics*, vol. 33, no. 3, pp. 257–264, Apr. 2012, doi: 10.1002/bem.20707.

[109] S. J. Beebe, Y.-J. Chen, N. M. Sain, K. H. Schoenbach, and S. Xiao, "Transient features in nanosecond pulsed electric fields differentially modulate mitochondria and viability," *PLoS ONE*, vol. 7, no. 12, Dec. 2012, doi: 10.1371/journal.pone.0051349.

[110] I. Semenov, S. Xiao, and A. G. Pakhomov, "Primary pathways of intracellular Ca2+ mobilization by nanosecond pulsed electric field," *Biochim. Biophys. Acta BBA - Biomembr.*, vol. 1828, no. 3, pp. 981–989, Mar. 2013, doi: 10.1016/j.bbamem.2012.11.032.

[111] I. Semenov, S. Xiao, O. N. Pakhomova, and A. G. Pakhomov, "Recruitment of the intracellular Ca2+ by ultrashort electric stimuli: The impact of pulse duration," *Cell Calcium*, vol. 54, no. 3, pp. 145–150, Sep. 2013, doi: 10.1016/j.ceca.2013.05.008.

[112] G. L. Thompson, C. C. Roth, M. A. Kuipers, G. P. Tolstykh, H. T. Beier, and B. L. Ibey, "Permeabilization of the nuclear envelope following nanosecond pulsed electric field exposure," *Biochem. Biophys. Res. Commun.*, vol. 470, no. 1, pp. 35–40, Jan. 2016, doi: 10.1016/j.bbrc.2015.12.092.

[113] E. B. Sözer, S. Haldar, P. S. Blank, F. Castellani, P. T. Vernier, and J. Zimmerberg, "Ultra-fast electroporation of giant unilamellar vesicles — experimental validation of a

molecular model," *bioRxiv*, p. 2020.01.01.890137, Jan. 2020, doi: 10.1101/2020.01.01.890137.

[114]   M. Casciola, S. Xiao, and A. G. Pakhomov, "Damage-free peripheral nerve stimulation by 12-ns pulsed electric field," *Sci. Rep.*, vol. 7, no. 1, Art. no. 1, Sep. 2017, doi: 10.1038/s41598-017-10282-5.

[115]   A. G. Pakhomov, I. Semenov, M. Casciola, and S. Xiao, "Neuronal excitation and permeabilization by 200-ns pulsed electric field: An optical membrane potential study with FluoVolt dye," *Biochim. Biophys. Acta BBA - Biomembr.*, vol. 1859, no. 7, pp. 1273–1281, Jul. 2017, doi: 10.1016/j.bbamem.2017.04.016.

[116]   M. Casciola *et al.*, "Cancellation of nerve excitation by the reversal of nanosecond stimulus polarity and its relevance to the gating time of sodium channels," *Cell. Mol. Life Sci.*, vol. 76, no. 22, pp. 4539–4550, Nov. 2019, doi: 10.1007/s00018-019-03126-0.

[117]   A. G. Pakhomov, A. M. Bowman, B. L. Ibey, F. M. Andre, O. N. Pakhomova, and K. H. Schoenbach, "Lipid nanopores can form a stable, ion channel-like conduction pathway in cell membrane," *Biochem. Biophys. Res. Commun.*, vol. 385, no. 2, pp. 181–186, Jul. 2009, doi: 10.1016/j.bbrc.2009.05.035.

[118]   L. Yang, G. L. Craviso, P. T. Vernier, I. Chatterjee, and N. Leblanc, "Nanosecond electric pulses differentially affect inward and outward currents in patch clamped adrenal chromaffin cells," *PLoS ONE*, vol. 12, no. 7, Jul. 2017, doi: 10.1371/journal.pone.0181002.

[119]   A. Rossi *et al.*, "Mechanisms and immunogenicity of nsPEF-induced cell death in B16F10 melanoma tumors," *Sci. Rep.*, vol. 9, no. 1, Art. no. 1, Jan. 2019, doi: 10.1038/s41598-018-36527-5.

[120]   O. N. Pakhomova, B. W. Gregory, I. Semenov, and A. G. Pakhomov, "Two modes of cell death caused by exposure to nanosecond pulsed electric field," *PLoS ONE*, vol. 8, no. 7, Jul. 2013, doi: 10.1371/journal.pone.0070278.

[121]   E. C. Gianulis, C. Labib, G. Saulis, V. Novickij, O. N. Pakhomova, and A. G. Pakhomov, "Selective susceptibility to nanosecond pulsed electric field (nsPEF) across different human cell types," *Cell. Mol. Life Sci.*, vol. 74, no. 9, pp. 1741–1754, May 2017, doi: 10.1007/s00018-016-2434-4.

[122] K. Morotomi-Yano, H. Akiyama, and K. Yano, "Different involvement of extracellular calcium in two modes of cell death induced by nanosecond pulsed electric fields," *Arch. Biochem. Biophys.*, vol. 555–556, pp. 47–54, Aug. 2014, doi: 10.1016/j.abb.2014.05.020.

[123] G. He *et al.*, "Multifunctional branched nanostraw-electroporation platform for intracellular regulation and monitoring of circulating tumor cells," *Nano Lett.*, vol. 19, no. 10, pp. 7201–7209, Oct. 2019, doi: 10.1021/acs.nanolett.9b02790.

[124] Y. Cao *et al.*, "Nontoxic nanopore electroporation for effective intracellular delivery of biological macromolecules," *Proc. Natl. Acad. Sci.*, vol. 116, no. 16, pp. 7899–7904, Apr. 2019, doi: 10.1073/pnas.1818553116.

[125] T. Kotnik, L. Rems, M. Tarek, and D. Miklavčič, "Membrane electroporation and electropermeabilization: mechanisms and models," *Annu. Rev. Biophys.*, vol. 48, no. 1, pp. 63–91, May 2019, doi: 10.1146/annurev-biophys-052118-115451.

[126] C. Yao, J. Ning, H. Liu, Y. Lv, Y. Zhao, and S. Dong, "Nanosecond pulses targeting intracellular ablation increase destruction of tumor cells with irregular morphology," *Bioelectrochemistry*, vol. 132, p. 107432, Apr. 2020, doi: 10.1016/j.bioelechem.2019.107432.

[127] D. A. Stewart, T. R. Gowrishankar, and J. C. Weaver, "Transport lattice approach to describing cell electroporation: use of a local asymptotic model," *IEEE Trans. Plasma Sci.*, vol. 32, no. 4, pp. 1696–1708, Aug. 2004, doi: 10.1109/TPS.2004.832639.

[128] Z. Vasilkoski, A. T. Esser, T. R. Gowrishankar, and J. C. Weaver, "Membrane electroporation: the absolute rate equation and nanosecond time scale pore creation," *Phys. Rev. E*, vol. 74, no. 2, p. 021904, Aug. 2006, doi: 10.1103/PhysRevE.74.021904.

[129] K. C. Smith, J. C. Neu, and W. Krassowska, "Model of creation and evolution of stable electropores for DNA delivery," *Biophys. J.*, vol. 86, no. 5, pp. 2813–2826, May 2004, doi: 10.1016/S0006-3495(04)74334-9.

[130] W. Krassowska and P. D. Filev, "Modeling electroporation in a single cell," *Biophys. J.*, vol. 92, no. 2, pp. 404–417, Jan. 2007, doi: 10.1529/biophysj.106.094235.

[131] J. Li and H. Lin, "Numerical simulation of molecular uptake via electroporation," *Bioelectrochemistry*, vol. 82, no. 1, pp. 10–21, Aug. 2011, doi: 10.1016/j.bioelechem.2011.04.006.

[132] C. Yao *et al.*, "Targeted cell membrane damage by bipolar high repeated frequency pulses," *IEEE Trans. Dielectr. Electr. Insul.*, vol. 24, no. 5, pp. 3270–3282, Oct. 2017, doi: 10.1109/TDEI.2017.006306.

[133] R. P. Joshi, Qin Hu, and K. H. Schoenbach, "Modeling studies of cell response to ultrashort, high-intensity electric fields-implications for intracellular manipulation," *IEEE Trans. Plasma Sci.*, vol. 32, no. 4, pp. 1677–1686, Aug. 2004, doi: 10.1109/TPS.2004.830971.

[134] K. C. Smith and J. C. Weaver, "Active mechanisms are needed to describe cell responses to submicrosecond, megavolt-per-meter pulses: cell models for ultrashort pulses," *Biophys. J.*, vol. 95, no. 4, pp. 1547–1563, Aug. 2008, doi: 10.1529/biophysj.107.121921.

[135] T. R. Gowrishankar, A. T. Esser, Z. Vasilkoski, K. C. Smith, and J. C. Weaver, "Microdosimetry for conventional and supra-electroporation in cells with organelles," *Biochem. Biophys. Res. Commun.*, vol. 341, no. 4, pp. 1266–1276, Mar. 2006, doi: 10.1016/j.bbrc.2006.01.094.

[136] L. Chang *et al.*, "3D nanochannel electroporation for high-throughput cell transfection with high uniformity and dosage control," *Nanoscale*, vol. 8, no. 1, pp. 243–252, 2016, doi: 10.1039/C5NR03187G.

VITA

Somen Baidya received the B.Sc. degree in electrical and electronic engineering from the Bangladesh University of Engineering and Technology, Dhaka, Bangladesh in 2012, the M.Sc. degree in Applied Engineering from the Georgia Southern University, Statesboro, GA, USA, in 2016. From 2012 to 2014, he was with Robi Axiata Limited, as a system engineer.

During his tenure of Ph.D. study at University of Missouri-Kansas City, Mr. Baidya received the School of Graduate Studies Research Grant in 2018-2019 session. He has been an active member of the Biomedical Engineering Society since 2018. Mr. Baidya's research has resulted in 1 book chapter, 3 peer-reviewed journal articles, and 11 peer-reviewed conference articles. His research interest includes (a) application of nanoplasmonics in biomarker application to detect the presence of extracellular vesicles and virions, (b) computational and numerical modeling of bioelectric phenomena in human body, (c) design and implementation of high power antennas to conduct electroporation/supra-electroporation studies, (d) modulate cell signaling by means of external electrical excitation, (e) characterization of optical scattering behavior of extraterrestrial particles (lunar regolith).